UNIVERSITY OF CALIFORNIA

Los Angeles

Development and Testing of a Portable Multi-Channel Depth-Resolved Near Infrared Spectroscopy System for Lower Leg Tissue Oxygenation Monitoring

A dissertation submitted in partial satisfaction of the

requirements for the degree Doctor of Philosophy

in Biomedical Engineering

by

Marko N Kostic

2013

ABSTRACT OF THE DISSERTATION

Development and Testing of a Portable Multi-Channel Depth-Resolved Near Infrared Spectroscopy System for Lower Leg Tissue Oxygenation Monitoring

by

Marko N Kostic

Doctor of Philosophy in Biomedical Engineering

University of California, Los Angeles, 2013

Professor Warren Grundfest, Chair

Near infrared spectroscopy [NIRS] is a non-invasive, non-ionizing imaging technique that uses light in the 650 nm to 2,500 nm region of the electromagnetic spectrum. In medical applications, optical devices utilize what is known as the biologic window (i.e. "therapeutic widow"). This window encompasses the light from 600 nm to approximately 1,400 nm. The reason why many medical optical devices exploit light sources within this spectrum is that tissue proteins are relatively transparent at these wavelengths with the exception of certain chromophores such as oxygenated and deoxygenated hemoglobin, fat, and water. However, light is highly scattered by the tissue and this scattering phenomena must be considered when obtaining information at depth within tissues. Thus, good penetration of light into the tissue and investigation of chromophores of interest at various depths is possible but requires careful modeling and understanding of light scattering at given depths. Since their introduction, medical

NIRS devices have been used in many physiologic monitoring applications, including, pulse oximetry, functional NIR for measuring the neuronal activity in the brain, measurement of oxygen consumption in skeletal muscles, and more recently the measurement of tissue blood perfusion.

This dissertation investigated a hypothesis that multi-channel depth-resolved near infrared spectroscopy can be used to monitor lower leg tissue oxygenation and lower leg oxygenation abnormalities and that depth-resolved data collection will provide useful information for analyzing the oxygenation state of tissue. The work presented here details development of a novel portable multi-channel NIRS system capable of long-term non-invasive monitoring of lower leg tissue blood oxygenation levels. Twenty two healthy subjects took part in the feasibility study of the novel system. The study examined the performance of the novel NIRS system in acquiring depth resolved multi-channel data from control leg and test leg, which was subjected to 60-second venous occlusion. The results showed that: The system is capable of acquiring statistically significant multi-channel NIRS data during venous occlusion with or without baseline data; and depth-resolved data provides significant information for analyzing oxygenation state of tissue. These findings indicate that the novel multi-channel depth resolved near infrared spectroscopy system could be used for lower leg tissue oxygenation monitoring.

The dissertation of Marko N Kostic is approved.

James Warwick Bisley

V Reggie Edgerton

E Carmack Holmes

Rahul Singh

Warren Grundfest, Committee Chair

University of California, Los Angeles

2013

This dissertation is dedicated to my parents, Vida and Nikola, and my brother Dusan for their endless love, support, and encouragement. I would not be who I am today without you…

To my wife Lee and our two bears, Nikola and Aleksandar, for their love, support, patience, and for being there through good and challenging times.

TABLE OF CONTENTS

LIST OF FIGURES

LIST OF TABLES

List of Abbreviations

ACS	acute compartment syndrome
ADC	analog-to-digital converter
APD	avalanche photo detector
BP	blood pressure
CCP	critical closing pressure
CECS	chronic exertional compartment syndrome
CPP	compartmental perfusion pressure
CPU	central processing unit
CV	coefficient of variability
DCO	digitally controlled oscillator
DC	direct current
DP	differential pathlength
DPF	differential pathlength factor
G	geometry-dependent factor (scattering losses)
HbO2	oxygenated hemoglobin
Hct	hemoglobin count
HHb	deoxygenated hemoglobin
HHR	health history questionnaire
HR	heart rate
Hz	Hertz
ICP	intra-compartmental pressure

IR	infrared
IRB	institutional review board
LDA	linear discriminant algorithm
LED	light emitting diode
LSB	least significant bit
MC	Monte Carlo
MCML	multi-layered Monte Carlo
NIR	near infrared
NIRS	near infrared spectroscopy
OD	optical density
OTC	over the counter
PC	personal computer
PD	photo detector
PDF	probability density function
POC	proof-of-concept
PPLL	pulse phase-locked loop
SAR	successive approximation
SPICE	simulation program with integrated circuit emphasis
TIA	trans-impedance amplifier
US	ultrasound
USB	universal serial bus
VO	venous occlusion

INDEX

ACKNOWLEDGMENTS

I would like to thank my advisor, Professor Warren Grundfest, for his support, guidance, and help for the past five years. Without his help, I would not have been able to finish this project or my graduate studies. Thank you!

I would like to thank my Committee members, Professors James Bisley, Reggie Edgerton, E. Carmack Holmes, and Rahul Singh, for their invaluable comments and suggestions on my research.

I would also like to thank my team members, Tara Vartanian, James Garritano, and Noah Goldman for their help with the feasibility study, data processing and analysis, and numerous discussions.

I would like to thank my extended family members for their support and help throughout these years. In addition, I would like to thank numerous friends who have helped me both personally and professionally over the years, including Johnnette Dees and Durwood Stephens, Bob and MJ Derkash, Diana and Howard Vagneur, Dan and Lynne Kerst, Tom and Mary Ann Sullivan, Bane and Ljilja Vlajinic, Dr. Jennifer Cummings, Dr. Steven Girouard, Dr. George Krstic, and Dr. Budimir Drakulic.

Finally, I would like to thank my parents and my brother for their endless support and encouragement. In addition, I would like to thank my wife for her support, understanding, patience, and for our two little bears.

VITA

2000	**B.Sc. Electrical Engineering**, University of Mississippi, Oxford, Mississippi *Honors: Magna Cum Laude*
2000-2002	**Design Engineer**, VSE Inc., Glenwood Springs, Colorado
2002-2003	**Design Engineer**, Glumac International, Irvine, California
2003-2009	**R&D Systems Engineer**, Signal Life, Inc., Los Angeles, California
2009	**M.Sc. Biomedical Engineering**, University of California, Los Angeles
2009-2011	**Scientific Advisor**, Telemedicine and Advanced Technology Research Center (TATRC), U.S. Army Medical Research and Materiel Command (USMRMC)
2011-2013	**Graduate Student Researcher**, Biophotonics and Minimally Invasive Surgical Systems Laboratories, Bioengineering Department, University of California, Los Angeles

PUBLICATIONS AND PRESENTATIONS

M. N. Kostic, "Development of a Novel Portable Multi-channel Near Infrared Spectroscopy System," *Stud Health Technol Inform*, vol. 165, 2013.

M. N. Kostic, S. Fakhar, T. Foxall, B. S. Drakulic, and M. W. Krucoff, "Evaluation of Novel ECG Signal Processing on Quantification of Transient Ischemia and Baseline Wander Suppression," 2007, pp. 2199–2202.

M. Arruda, B. S. Drakulic, **M. N. Kostic**, S. Fakhar, and A. Natale, "A novel portable wireless multi-channel ECG and intracardiac recording system," *Heart Rhythm*, vol. 3, no. 5, pp. S328–S329, May 2006.

B. S. Drakulic, Z. Konstantinovic, **M. Kostic**, B. Vlajinic, and G. Nakatsuka, "Electrocardiograph high-pass frequency response revisited," *Journal of Electrocardiology*, vol. 38, no. 4, Supplement, p. 141, Oct. 2005.

Chapter 1

Introduction

Near infrared spectroscopy [NIRS] is a non-invasive, non-ionizing imaging technique that uses light in the 650 nm to 2,500 nm region of the electromagnetic spectrum. In medical applications, optical devices utilize what is known as the biologic window (i.e. "therapeutic widow"). This window encompasses the light from 600 nm to approximately 1,400 nm [1]. The reason why many medical optical devices exploit light sources within this spectrum is that tissue proteins are relatively transparent at these wavelengths with the exception of certain chromophores such as oxygenated and deoxygenated hemoglobin, fat, and water [2]. However, light is highly scattered by the tissue and this scattering phenomena must be considered when obtaining information at depth within tissues [3]–[5]. Thus, good penetration of light into the tissue and investigation of chromophores of interest at various depths is possible but requires careful modeling and understanding of light scattering at given depths. Since their introduction, medical NIRS devices have been used in many physiologic monitoring applications, including, pulse oximetry, functional NIR for measuring the neuronal activity in the brain, measurement of oxygen consumption in skeletal muscles, and more recently the measurement of tissue blood perfusion [6]–[14]. This dissertation will investigate a hypothesis that multi-channel depth-resolved near infrared spectroscopy can be used to monitor lower leg tissue oxygenation and lower leg oxygenation abnormalities and that depth-resolved data collection will provide useful information for analyzing the oxygenation state of tissue.

This dissertation presents a novel portable multi-channel NIRS system capable of long-term non-invasive monitoring of lower leg tissue blood oxygenation levels. The work presented here details development process of the system and it includes validation results from Monte Carlo simulations and a feasibility study. Advantages and limitations of the novel system are discussed, as well as potential future improvements and clinical studies.

Dissertation work is divided into seven chapters: Chapter 2 provides background on the clinical motivation for current research. The chapter begins with an overview of the lower limb anatomy, description of an acute compartment syndrome, a common lower limb perfusion abnormality, and its underlying pathophysiology. This chapter continues with an overview of current clinical technologies for detection of acute compartment syndrome and finally, the emerging technologies for tissue oxygenation monitoring and detection of compartment syndrome. Chapter 3 describes light-tissue interactions and it presents some of the main optical properties that affect light propagation in biological tissues, including index of refraction, scattering, absorption, and spectra of some common chromophore in human body. The chapter details lower leg tissue layers and their effect on light propagation. This chapter also presents Monte Carlo simulation results for a multi-layer lower leg anatomy model. Chapter 4 describes development and design of the novel NIRS system. It provides details regarding several prototype models, as well as technical justifications for the current version of the system. Chapter 5 outlines methods for clinical testing of the device based on clinical needs outlined in Chapter 2. Specifics regarding study sample size, subject inclusion and exclusion criteria are also presented. Chapter 6 provides data analysis methods and the results of a feasibility study, as well as discussion on future clinical system development. Finally, Chapter 7 offers conclusions and future directions for the clinical system development.

Chapter 2

Background

The novel near infrared spectroscopy [NIRS] system is designed to be portable and capable of long-term non-invasive monitoring of lower leg tissue blood oxygenation. In order to provide clinical motivation for current research, this chapter begins with the overview of the lower limb anatomy, description of an acute compartment syndrome, a common lower limb perfusion abnormality, and its underlying pathophysiology. The chapter continues with the overview of current clinical technologies for detection of acute compartment syndrome and two emerging non-invasive technologies for tissue oxygenation monitoring and detection of acute compartment syndrome.

2.1. Anatomy

Lower leg refers to part of the leg below the knee joint and above the ankle joint. This portion of the leg contains two major bones, the tibia and fibula, and has four distinct muscle compartments, each made up of their corresponding muscles, nerves, vascular structures, and fascia. The four lower leg compartments are: Anterior, lateral (peroneal), superficial posterior, and deep posterior (Figure 2-1, modified from [15]). Each of these compartments contain at least one neurovascular bundle. The anterior compartment includes the tibialis anterior, extensor hallucis longus, extensor digitorum longus, and fibularis tertius muscles. The compartment is innervated by the deep peroneal nerve and supplied by the anterior tibial artery and vein. The

lateral compartment encompasses fibularis longus and fibularis brevis muscles, both of which are innervated by the superficial peroneal nerve. The superficial posterior compartment includes the gastrocnemius, plantaris, and soleus muscles. These three muscles are innervated by the tibial nerve. The deep posterior compartment contains the popliteus, flexor hallucis longus, flexor digitorum, and tibialis posterior muscles. The tibial nerve and posterior tibial artery and vein support the function of deep posterior compartment [15], [16]. Muscle compartments are separated by layers of thick tissue called deep (or muscle) fascia. This densely packed, fibrous structure acts as a support and protection to the compartmental muscles and associated vessels and nerves. The muscle fascia contains very little, if any, vasculature. The fascia, however, contains many different types of sensory receptors, including the nociceptors. Highly dense collagen fibers make up the fascia and provide its strength and rigidity.

As mentioned earlier, the individual compartments of the lower leg contain their own vascular supplies, Figure 2-2 (adapted from [17]). This vasculature is a part of body's systemic circulation that includes arteries, arterioles, capillaries, venules, and veins. Arteries transport oxygenated blood from the heart to peripheral tissue under high pressure. Arterioles comprise control channels between the arteries and the capillaries and are also part of the high pressure systemic circulation. Located within tissues, capillaries exist as means for blood to travel from arterioles to venules. The capillaries have very thin permeable walls and function as networks for exchange of nutrients, electrolytes, hormones, fluids, etc. between blood and the interstitial fluid. Venules gather blood, which now contains cellular metabolic waste products and deoxygenated blood, from capillaries and transport it to veins. The veins, like the venules, are part of the low pressure systemic circulation and transport blood from periphery (i.e. tissue and venules) back to the heart.

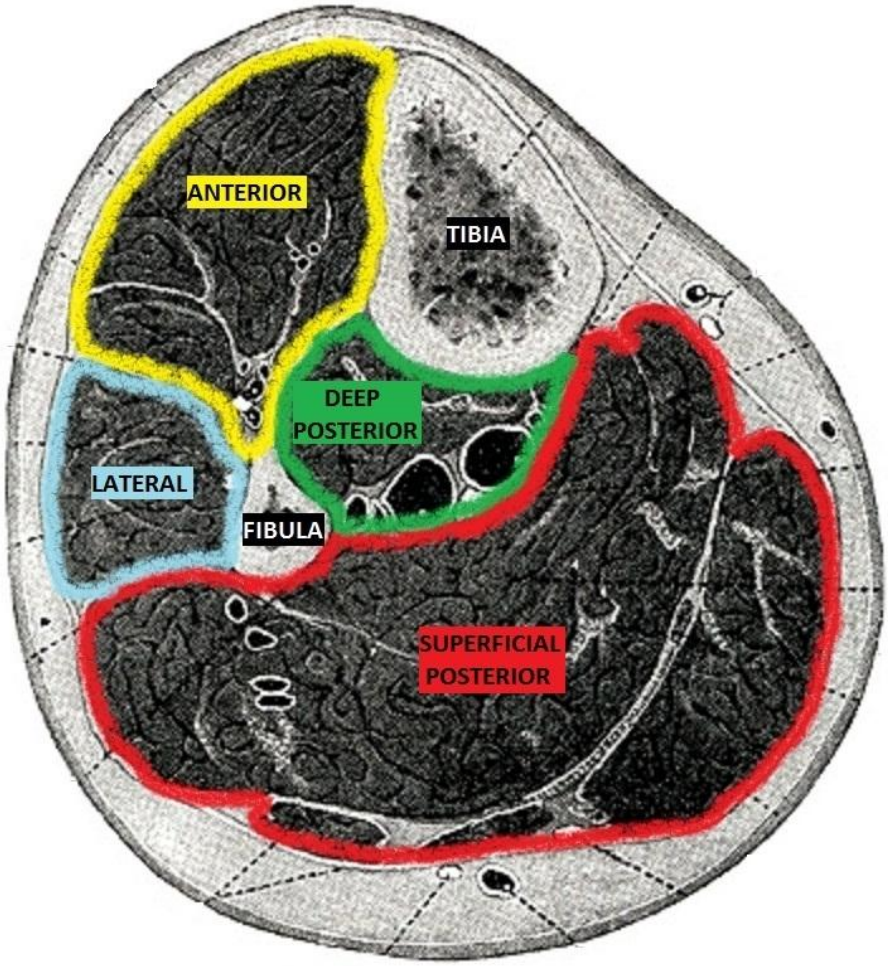

Figure 2-1 Lower leg compartments

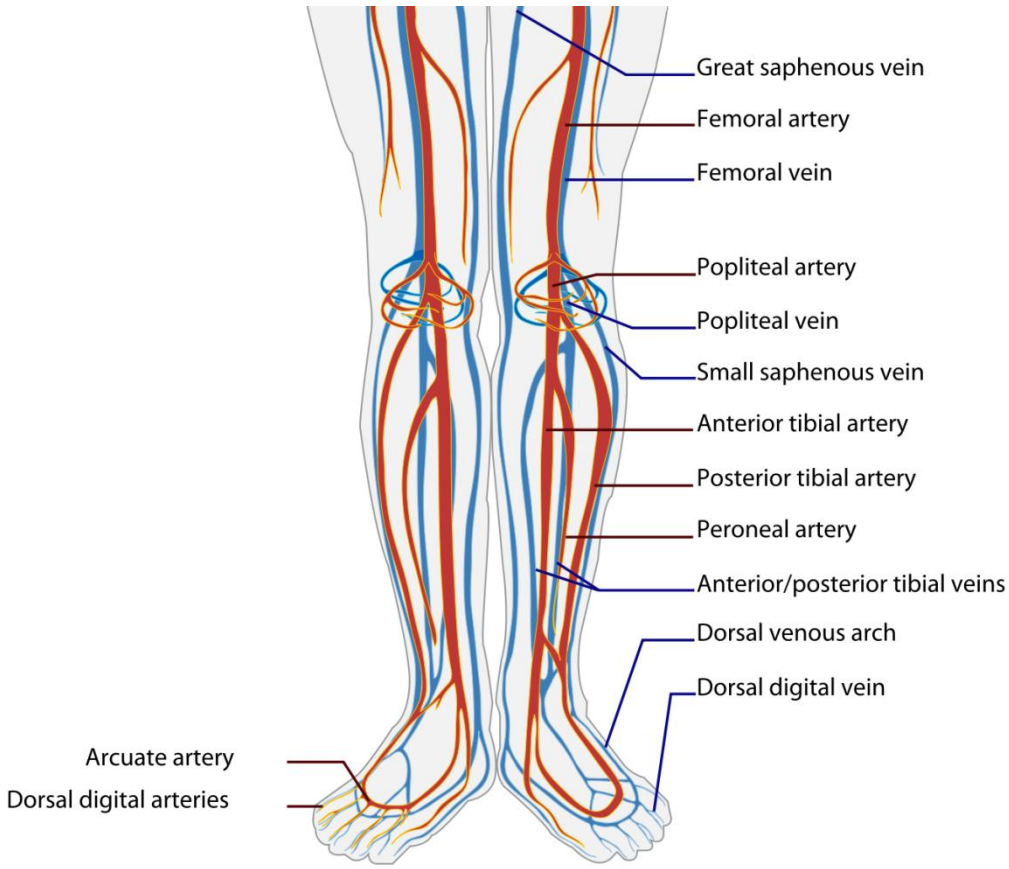

Figure 2-2 Lower leg vasculature

Blood flow through any vessel is governed by two factors: First factor is the pressure difference between two points in a vessel, known as the pressure gradient; the second factor is vascular resistance. Based on general form of Ohm's Law, equation (2-1), blood flow in systemic circulation, and in any vessel in general, is directly proportional to the pressure difference between two points in the vessel (e.g., between the arterial and venous side of capillaries) and inversely proportional to the vessel resistance (i.e. vascular resistance). Furthermore, Poiseuille Law of equation (2-2) shows that the flow within the blood vessel is

directly proportional to the fourth power of the vessel radius. Hence, small changes in the vessel radius will yield considerable change in the blood flow [18].

$$F = \frac{\Delta P}{R} \tag{2-1}$$

where: F is blood flow, ΔP is pressure difference between two points in a vessel, and R is vessel resistance.

$$F = \frac{\Delta P r^4 \pi}{8 \eta L} \tag{2-2}$$

where: F is blood flow, ΔP is pressure difference between two points in a vessel, r is vessel radius, η is dynamic fluid viscosity, and L is vessel length.

2.2. Compartment Syndrome

Compartment syndrome is a term referring to a condition of increased pressure within a tissue compartment. Increased intra-compartmental pressure causes loss of adequate blood circulation and tissue function becomes compromised, which may eventually lead to irreversible neuromuscular damage [19]. Compartment syndrome may develop in any compartment in the body, including the legs, arms, hands, and abdomen [20].

Based on severity and timeline of symptoms, the lower leg compartment syndromes may be placed in two distinct categories: Acute compartment syndrome [ACS], which presents with more severe and very aggressive symptoms; and chronic exertional compartment syndrome [CECS], which, as its name implies, results from a prolonged exercise and often has less severe

morbidity than the ACS [21]. Based on its origins, the ACS may be divided into two sub-categories: (1) Compartment syndrome caused by decreased compartment size (e.g., constriction by casts, compression, thermal injuries) and (2) compartment syndrome caused by increased compartment contents (e.g., hemorrhage, edema, reperfusion after trauma) [22]. The most common cause of ACS is trauma [20]. For the cases where trauma is not the primary cause, 20 percent of ACS cases are caused by ischemia in revascularized limbs. Table 2-1 shows some of the possible causes of ACS, as well as their incidence rates [23], [24]. Current research shows that acute compartment syndrome affects primarily the anterior compartments of lower legs. Hence, it is recommended that intra-compartmental pressure [ICP] measurement, the current clinical standard-of-care, be made in this compartment and elsewhere on indication only [25].

Table 2-1 Most Common Acute Compartment Syndrome Causes and Incidence Rates

Type	Example	Incidence [%]
Orthopedic		69 (36)
	Fractures and fracture surgery (tibial)	
Vascular		not available
	Arterial and venous injuries	
	Reperfusion injury	
	Hemorrhage	
Soft Tissue		23.2
	Crush injury	
	Burns	
	Prolonged limb compression	
Iatrogenic		2.32
	Arterial/venous puncture in anticoagulation patients	
	Casts and circular dressings	
	Pulsatile irrigation	
	Surgical Positioning (e.g., prolonged lithotomy position)	
	Pneumatic antishock garment	

2.3. Pathophysiology of ACS

The blood flow to each tissue of the body is controlled by individual metabolic needs of those tissues [18]. The living cells require both oxygen and various foodstuffs for their normal functioning. Blood carries both oxygen and foodstuffs (e.g., glucose, fatty acids) to the interstitial space via capillaries where they are absorbed by local cells. Once oxygen and foodstuffs enter cells, they react chemically with enzymes to create energy (adenosine triphosphate, ATP), which is then used for numerous intracellular metabolic processes [18].

As mentioned earlier, the compartment syndrome is characterized by increased compartmental pressure which decreases vessel radius, increases vascular resistance and thus reduces blood flow to the local muscle tissue. It was suggested recently [22] that two complementary theories can explain the compartment syndrome pathophysiology: (1) The arteriovenous gradient theory [26] and (2) the ischemia-reperfusion theory [27].

The arteriovenous gradient theory (Figure 2-3) is directly linked with the pressure difference in the vessel as described earlier. When the pressure difference between two points in the vessel reaches zero, blood flow ceases and no delivery of nutrients and removal of waste products from the local tissues occur. For instance, sudden trauma or injury to blood vessels of the lower leg causes bleeding and intramuscular swelling in that given area [28]. The ICP gradually increases in response to the inflammation, producing a force pushing against the rigid fascia enveloping the muscle compartment. As a result, intra-luminal venous pressures increase causing a decrease in the arteriovenous pressure gradient [29]. The pressure gradient value where termination of blood flow occurs is referred to as the critical closing pressure [CCP] [30].

Figure 2-3 Arteriovenous Gradient Theory Diagram

In contrast to arteriovenous gradient theory, the ischemia-reperfusion theory (Figure 2-4) describes the mechanism where damage to the skeletal muscles occurs during both the ischemic event as well as during reperfusion of the muscle tissue after the reestablishment of the blood flow [31]. Once the blood flow is reduced below a certain point, the muscle tissue becomes ischemic. Muscle (and nerve) tissue of the lower limbs have very limited tolerance to ischemia after which the tissue may develop complex regional pain syndrome, muscle necrosis, and even eventually lead to major amputation [32]. Muscles, for example, can tolerate only four hours of ischemia before irreversible changes occur [28]. The damage during reperfusion is caused by the release of oxygen-free radicals, large amounts of calcium in the damaged muscle tissue, and the permeation of neutrophils into the vessel [33]. Furthermore, the reintroduction of molecular oxygen during reperfusion increases microvascular permeability [31]. The increased microvascular permeability causes more leakage into interstitial space and further increase in compartment pressure which again leads to reduction or complete disappearance of arteriovenous gradient and consequently stops all blood flow.

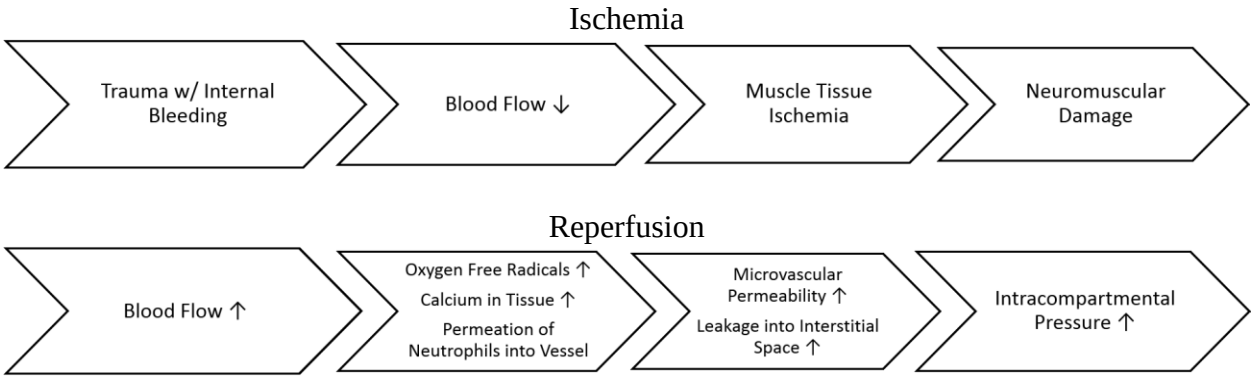

Figure 2-4 Ischemia-Reperfusion Theory Diagram

In addition to two theories just described, a significant contributing factor to morbidity associated with the acute compartment syndrome of the lower leg is time. Time has been proven to act as an additional cause of irreversible compartmental tissue damage [34]. Hargens *et al.* showed that the duration of increased ICP is responsible for tissue damage in the same manner as the level to which the pressure is raised [35]. This means that higher level of intra-compartmental pressure for a shorter period of time will have the same detrimental effect on compartment tissue as would lower level intra-compartmental pressure sustained for longer period of time [34]. Muscle cell damage is considered to become irreversible after about four hours of continuous ischemia [28]. Past this point, vascular closure becomes permanent and a "no reflow" phenomenon develops, which eliminates the possibility of reperfusion taking place again in the affected tissue [36].

2.4. Current Techniques for ACS Detection

Current techniques for the detection of acute compartment syndrome may be divided in two general categories: (1) Clinical observation and (2) direct measurement of intra-compartmental

pressure. The former utilizes knowledge and experience of the healthcare professional to diagnose possible presence of ACS while the latter utilizes invasive device to directly measure intra-compartmental pressure in the affected limb.

2.4.1. Clinical Observation

Clinical observation of patient symptoms is an initial method for diagnosing possible presence of an acute compartment syndrome [29]. Commonly accepted signs that are indicative of presence of ACS are altered sensation, muscle weakness, paresthesia, pink coloration of the skin, and most of all, excessive pain and sensitivity upon muscle movement [28]. Diagnosis of ACS based on these symptoms, however, fails to yield adequate accuracy for all patients. For example, unconscious patients or patients at an age too young to verbalize the presence of these symptoms are unable to be examined for suspected ACS [29]. Even though the excessive pain is one of the most commonly used symptoms for the ACS diagnosis, it is especially unreliable indicator of the presence of ACS. There are at least three major reasons for this unreliability. First, pain from the traumatic injury can be greater than the pain caused by the ACS and could, therefore, be overlooked. Second, "excessive" pain levels cannot be used uniformly for all patients because pain tolerance levels vary greatly from person to person. Third, ACS cannot be recognized during onset because excessive pain levels are only associated with ACS after the tissue damage has already taken place. In addition to these three reasons, the pain sensitivity upon application of external force or touch is not useful in confirming the presence of ACS in deep posterior compartment, which is located away from the surface of the leg and is therefore unresponsive to the touch [34]. For these reasons, it is crucial that clinician does not rely solely on physical

symptoms of the patient but to, instead, measure intra-compartmental pressure, which is the current gold standard for ACS diagnosis [29].

2.4.2. Direct Measurement of ICP - Manometer Method

The first device to measure intra-compartmental pressure was developed by Whiteside *et al.* and named the needle manometer [37]. In this technique, an 18-gauge needle is attached to a 20-ml syringe filled with air via a tube containing saline solution plus air, which is all hooked to a standard mercury manometer that reads the ICP [30]. Saline is initially injected into the compartment to establish and maintain an opening as the syringe is squeezed and its air pressure rises. Once the needle is fully inserted and the saline meniscus has adjusted to indicate rising pressures within the syringe, the manometer will display the ICP level [30]. For this method, patients are considered to be in danger of having ACS when the measured ICP rises to levels within 10-30 mmHg of the previously measured diastolic blood pressure [38]. Even though it is able to determine pressure values within the compartment, this is considered an inaccurate method due to a number of limitations. The overall trend in pressure within a compartment could not be analyzed because the manometer is only able to take discrete measurements [39]. Also, this procedure depends on the use of saline and works only under a bubble-free saline column. Thus, the formation of air bubbles along with the possibility of muscle or blood clot obstructing the needle tip may yield false ICP measurements [40].

2.4.3. Direct Measurement of ICP - Infusion Technique

Addressing the flaws found in manometer devices, the infusion method refers to the continuous monitoring of ICP levels using the catheter. Catheter allows the injection of saline solution and

is connected to an external pressure transducer, three-way stopcock, and a recorder [37]. The saline-filled catheters are inserted approximately two centimeters, via a 14-gauge needle, into the muscle compartment [38]. After waiting a few minutes to allow the inner area to re-stabilize, the ICP values are displayed [29]. Pressure levels exceeding 45 mmHg are considered indicative of ACS.

There are two types of catheters, the wick and slit, which are commonly used during infusion technique. Both styles have five 3-mm slits and hold a piece of polyethylene tubing at the end whose sole purpose is to ensure the tip is not left inside the tissue upon removal of the catheter [30]. The infusion technique provides continuous pressure recordings. A major limitation to this method, however, is that in order to measure accurate ICP levels, it is essential that the external dome transducer be located at the exact height as the tip of the catheter and that it must be frequently recalibrated to this position. Additionally, the catheter is still susceptible to blockage from blood clots and its ability to function still relies on bubble-free saline solution [40], [41].

Although effective in measuring pressure within a compartment, the catheter-based devices have a common drawback of relying on saline infusion which may increases ICP, thus providing false pressure readings [29], [39], [42]. In addition to displaying potentially false ICP readings, the catheter-based systems may increase chances for coagulation formation at the tip of the tube [40], as well as leave patients susceptible to infection [43]. Finally, care must be taken in proper positioning of the needle, leg, and monitoring device relative to one another in order to obtain accurate readings [44].

2.5. Emerging Noninvasive Technologies

To address shortcomings of the current ACS detection techniques, two emerging non-invasive technologies have been tested for monitoring and diagnosis of lower leg perfusion abnormalities: Near infrared spectroscopy [NIRS] and ultrasound [US]. These two techniques will be described next along with select devices that have already been used in clinical ACS studies.

2.5.1. Near Infrared Spectroscopy

Near infrared spectroscopy has been used in medical applications for several decades. A limited number of attempts, however, have been made to use NIRS technology in monitoring and diagnosing lower leg perfusion abnormalities, such as acute compartment syndrome. Principles and theory of operation of NIRS devices will be discussed in greater detail in Chapter 3. The current NIRS systems, which have been used in lower limb trauma studies, were actually developed for other applications, such as cerebral blood flow or exercise muscle oxygenation monitoring. The following are two select commercially-available NIRS systems that are presently being used in lower leg trauma and compartment syndrome detection studies: InSpectra™ Tissue Spectrometer by Hutchinson Technology, Inc. and INVOS® by Somanetics.

The first system, InSpectra™ Tissue Spectrometer, is a device by Hutchinson Technology, Inc. (Hutchinson, MN, USA). It uses NIRS technology to monitor and measure tissue oxygenation saturation (StO_2). This system has been found to be useful in the recognition and monitoring of reduced blood circulation [45]. In a 2000 study by Gianotti *et al.* [46], the Biospectrometer-NB Oximeter (a predecessor to the current InSpectra™ system) was used to determine whether near-infrared spectroscopy is capable of detecting lower extremity compartment syndrome. The system used one optical fiber within a probe to transmit light into

the tissue while a second optical fiber was responsible for receiving the reflected light and returning it to a photosensitive detector. Thus, the optical probe only sampled single tissue depth. The optical probe was placed on the surface of the skin of nine patients having elevated compartment pressures (indication of the possible existence of ACS). Separate control readings on 33 patients with no evidence of ACS were also made. In the ACS group, NIR-derived StO_2 values were taken pre- and post-fasciotomy. The pre-surgical StO_2 readings indicated 56 ± 27% tissue oxygen saturation values, while the postsurgical mean StO_2 values were 82 ± 16%. The control group appeared to have significantly higher mean StO_2 values of 87± 7%. The authors concluded that in subjects with clinically diagnosed ACS, NIR-derived StO_2 values of lower limb compartments were significantly lower than values of the control group. Furthermore, ACS subjects showed increase in StO_2 measures post-fasciotomy, indicating normalization in oxygen delivery to the affected areas. In a 2001 study by Gentilello *et al.* [47], the Biospectrometer-NB Oximeter device was used to gather tissue oxygen saturation (StO_2) in 15 volunteers with externally-applied lower leg sphygmomanometric blood pressure cuff. The pneumatic cuff was placed over a 25-mm optical probe, encircling the anterior compartment of the lower leg, and was inflated to simulate the ACS by applying the external pressure to the compartment. Previous studies have found that the pressure applied to the exterior of the compartment is approximately equal to the intracompartmental pressure [48]. The NIRS system recorded relative StO_2 values of the underlying tissue. The authors concluded that these values significantly correlated with ischemic condition, just as compartmental perfusion pressure [CPP] readings related to the ischemic condition.

Even though authors of two clinical studies mentioned above concluded utility of Biospectrometer-NB Oximeter device in ACS detection, the current version of that system,

InSpectra™ 650, has several limitations. Based on the information provided by the manufacturer, these limitations include: Use of single pair of light source and detector to sample a single depth of tissue; the system weighs 4 kilograms and the main unit is bulky (19,000 cm^3), thus limiting system's use to hospital bedside only; optical probe connects to the main unit using a 3 meter cable.

The INVOS® System is an oxygen saturation monitor by Somanetics Corporation (Troy, MI, USA) built for measuring regional oxygen saturation (rSO2) of blood in both brain and body tissue. It has 730 nm and 810 nm light emitting diodes [LEDs] as its light sources and two photodiode detectors, located 30 and 40 mm away from the LEDs, for receiving near-infrared light [49]. Thus, system is capable of sampling a maximum of four different tissue depths. In 2009, Shuler *et al.* [50] conducted a study using INVOS® device in lower extremity trauma. The StO_2 values were measured in 26 patients with tibial fractures and 25 uninjured control subjects. For each subject, NIRS measurements at the mid-tibial level of all four compartments in both legs were obtained. Data was acquired by placing the device's sensor pad over the tibial region of all four compartments. Results for tissue oxygenation levels were displayed in the form of a percentage for the proportion of hemoglobin saturated with oxygen. Analysis of mean tissue oxygenation values for all four compartments in both experimental and control groups showed an average of 15.4% higher values for injured legs than uninjured legs. The authors of this study concluded that tibial fractures lead to increase in tissue oxygenation levels. They believed that these findings indicated that, prior to ischemia that was caused by intracompartmental pressure [ICP] increase, the hyper perfusion occurred due to decreased vascular resistance after trauma.

Based on the information provided by the manufacturer, some of the limitations of the INVOS® 5100C system include: Sampling of four different tissue depths; the system weighs 4.95 kilograms and the main unit is bulky (13,224 cm^3); system's primary power supply is mains voltage (100-240V); optical sensors connect to the main unit using a 1.5 meter cable. The latter three characteristics of the system limit its use to hospital bedside only.

2.5.2. Ultrasound

The ultrasound technology has been used in limited number of cases for ACS detection [43], [51]. For example, in a clinical study by Weimann *et al.*, Pulse Phase-Locked Loop (PPLL) ultrasound was used to measure intramuscular pressure as means of detecting compartment syndrome [43]. The PPLL system was connected to an ultrasound transducer that was attached to the anterior portion of the lower leg. A frequency of 2 MHz was delivered through skin and muscle, reflected off the bone, and sent back to the transducer. The arterial pressure waveforms were measured by way of facial displacements, which indicated whether the patient had normal or unusually elevated ICP levels [43]. The ultrasound technology, however, is limited by muscle fasciculation, which obscures US signal when the ICP catheter is present.

2.6. Summary

This chapter provided clinical motivation for current research. The lower leg anatomy was described along with important concepts related to its vasculature. Two types of compartment syndromes were defined and their possible causes. The chapter then focused on the description of an acute compartment syndrome, a common lower leg perfusion abnormality, its causes, and underlying pathophysiology. This chapter provided an overview of current techniques for the

diagnosis of acute compartment syndrome, clinical observation and invasive intra-compartmental pressure measurement. Due to shortcomings of current ACS detections techniques, two non-invasive emerging technologies, near infrared spectroscopy and ultrasound, were introduced and described in reference to their potential application for lower limb perfusion abnormality diagnosis and monitoring. The limitations of current NIRS and US systems were also highlighted. As the focus of this dissertation is development of a novel NIRS system for lower leg tissue oxygenation monitoring, next chapter will provide details about the theory of operation of near infrared spectroscopy devices and how lower leg anatomy and physiology may affects light propagation.

Chapter 3

Theory of Operation of NIRS Devices

This chapter provides an overview of the theory of operation of near infrared spectroscopy devices. In particular, this chapter will describe what happens to light when it enters human tissue. It will present some of the main optical properties that affect light propagation in biological tissues [52], including index of refraction, scattering, absorption, as well as spectra of some common chromophore in human body. This chapter will then provide details on the lower leg tissues and their specific effect on light propagation. Finally, Monte Carlo simulation results will be presented for a multi-layer lower leg anatomy model.

Several physical phenomena occur when the incident light impacts human tissue (Figure 3-1). First, the light is partially reflected and partially transmitted. This is caused by the refractive index mismatch between the medium above the tissue (e.g., air) and the tissue itself. Second, once the light is refractively transmitted into tissue, scattering and potentially absorption will occur. The latter will depend on the concentration and type of chromophores present in tissue. Finally, mostly due to scattering, the light is either reflected back to the same surface as the incident light or it is transmitted to the opposite side from the incident light. To better understand these three physical phenomena, index of refraction, scattering, and absorption will be discussed next in detail.

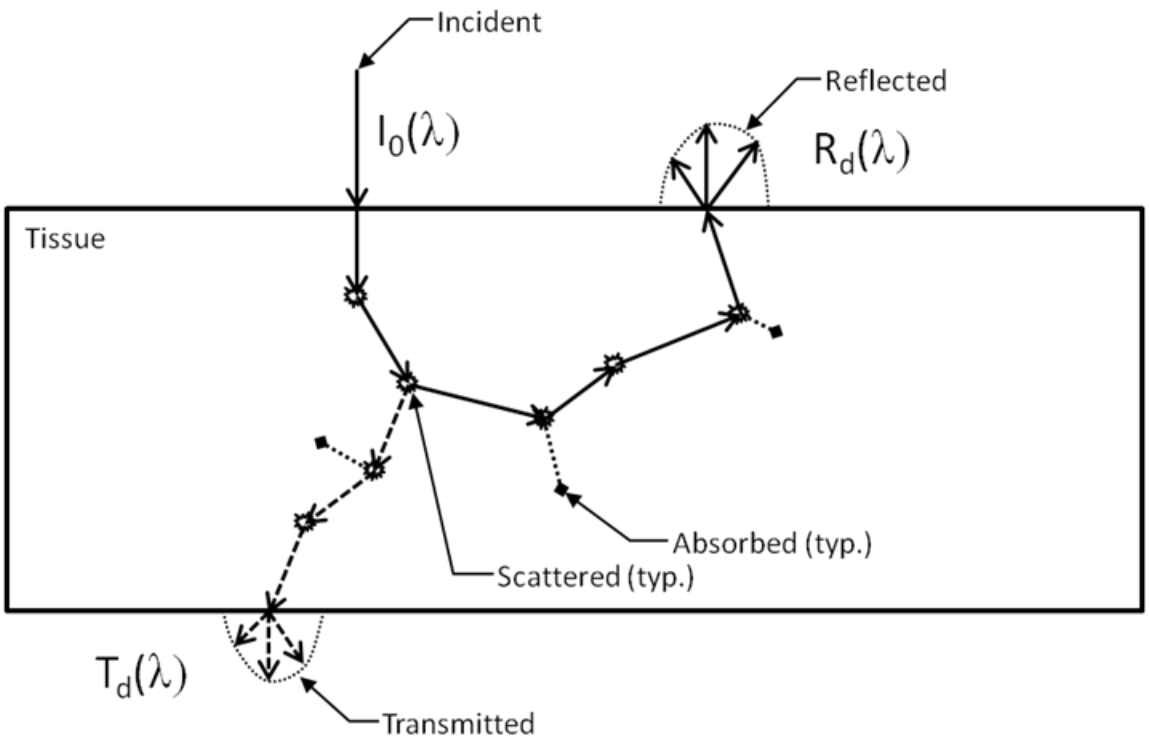

Figure 3-1 Light Interactions with Tissue

3.1. Index of Refraction

The index of refraction is defined as the ratio of the speed of light in vacuum to the speed of light in the medium [53]. It is usually denoted as *n* and it is always greater than one. Therefore, when a light from one medium (e.g., air) enters a medium of different index of refraction, the direction of light is changed. The relation that governs how light will behave due to the optical mismatch between two boundaries (Figure 3-2) is described by Snell's law as follows:

$$n_1 \sin\Theta_1 = n_2 \sin\Theta_2 \tag{3-1}$$

$$\sin\Theta_2 = \frac{n_1}{n_2}\sin\Theta_1 \tag{3-2}$$

where Θ_1 is the angle of incidence, Θ_2 is the angle of refraction, and n_1 and n_2 are refractive indices of two media.

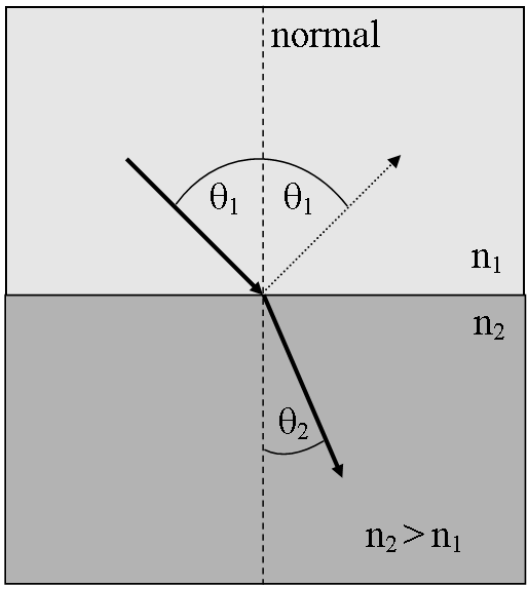

Figure 3-2 Illustration of Snell's Law

Biological tissues usually have higher average refractive index (e.g., n_2) than the surrounding air (e.g., n_1). This mismatch, from lower to higher refractive index, causes partial reflection of the incident light at the surface, called Fresnel reflection [54], and results in partial refractive transmission. The refracted transmitted light enters tissue and becomes scattered and potentially absorbed.

3.2. Scattering

Light scattering is a process where light trajectory is changed due to local (i.e. medium) non-uniformities (Figure 3-3, modified from [55]). The scattering can be characterized as elastic and inelastic. The former is a case where there is negligible energy transfer between the incident light and the scatters while the latter is the opposite. Based on the number of scattering events, the scattering can be single or multiple. The single scattering occurs when the light is scattered

by a single non-uniformity. On the other hand, multiple scattering occurs when there is a large concentration of non-uniformities in a medium; such is the case in biological tissues.

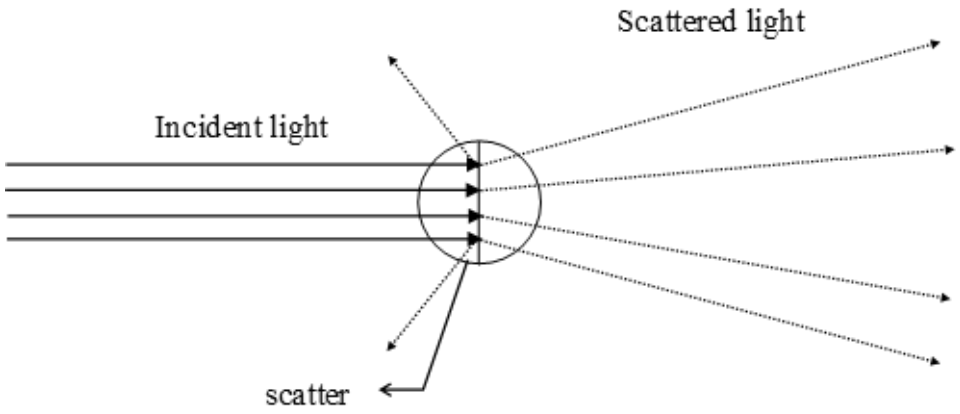

Figure 3-3 Light Scattering from a Single Scattering Particle (i.e. scatter)

In order to better understand scattering, a concept of scattering cross section is introduced. The scattering cross section, σ_s, is defined [52] as the ratio of scattered light power, P_S, to the intensity (power per unit area) of the incident wave, I_0:

$$\sigma_s(\hat{s}) = \frac{P_s}{I_0} \tag{3-3}$$

In a medium containing large number of non-uniformities (i.e. scatters), the scattering cross section (in units of area) and density of scatterers (in number per volume), ρ_s, characterize scattering coefficient (in units per length), μ_s, as follows:

$$\mu_s = \rho_s \cdot \sigma_s \tag{3-4}$$

Furthermore, the average distance that light travels before the next scattering event can be defined as the inverse of the coefficient of scattering, or $1/\mu_s$, and it is called the scattering mean free path, l_s.

In addition to scattering coefficient μ_s, which is applicable for all cases, the reduced scattering coefficient, μ_s', is often used in situations involving propagation of visible and near infrared light through medium where light transport is primarily governed by scattering and not absorption (i.e. $\mu_s' >> \mu_a$). The reduced scattering coefficient combines the scattering coefficient and the anisotropy, *g*, via equation (3-5). The anisotropy is a dimensionless measure of the amount of photon energy preserved in the forward direction (i.e. direction of incident photon) after a single scattering event. Therefore, the reduced scattering coefficient corresponds to the effective number of isotropic scatters per unit length.

$$\mu_s' = \mu_s \cdot (1 - g) \tag{3-5}$$

Finally, based on the size of non-uniformities and wavelength of light, the scattering can be explained by two different theories: Rayleigh scattering and Mie scattering. The Rayleigh scattering occurs due to spherical scatterers that are much smaller than the wavelength of the light ($r << \lambda$). Mie scattering theory, on the other hand, describes light scattering without limitations with regard to scatter size or wavelength of light.

3.2.1. Rayleigh scattering

The Rayleigh scattering is applicable to cases where scatters are small non-absorbing dielectric spherical particles. Each scatter encounters a uniform electric field in its surroundings which causes it to have a dipole moment. This scatter dipole moment oscillates with the same frequency as the incident light and gives off dipole radiation. This dipole radiation (i.e. scattered light) has the same frequency as the incident light and is radiated in all directions. From the

Mueller matrix for Rayleigh scattering [56], [57] one is able to obtain the intensity of scattered light from a single particle for the unpolarized incident beam having intensity I_0:

$$I_S = \frac{8\pi^4 r^6}{R^2 \lambda^4} \left| \frac{n^2 - 1}{n^2 + 2} \right|^2 (1 + \cos^2 \theta) I_0 \tag{3-6}$$

where I_S - intensity from a single scatter; I_0 - intensity of the incident light; r - radius of a spherical particle, scatter; R - distance to the observer; λ - wavelength of the light; n - relative refractive index of particles.

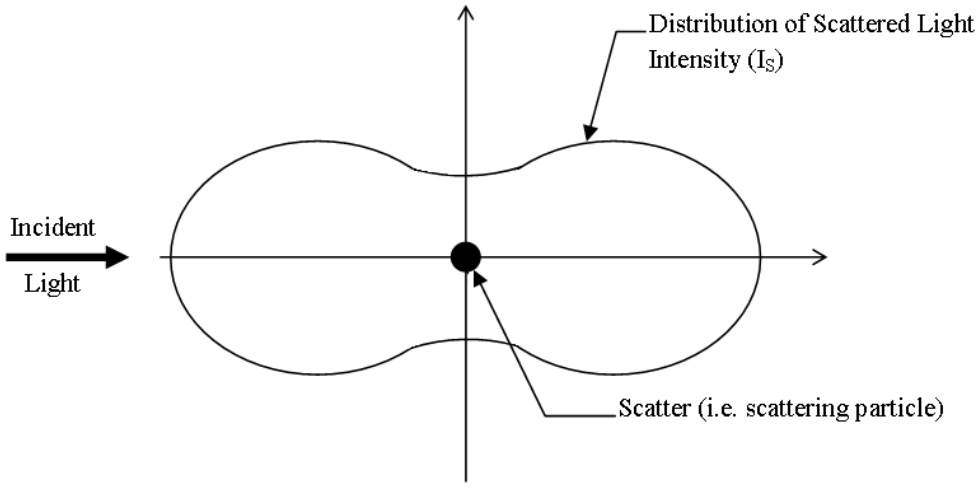

Figure 3-4 Rayleigh Scattering

3.2.2. Mie scattering

As stated above, Mie scattering theory describes light scattering without limitations with regard to scatter size or wavelength of light. The Mie theory plays an important role in cases where size of the scattering particle is similar to the wavelength of incident light ($r \approx \lambda$), which is the situation where Rayleigh ($r << \lambda$) and geometric ($r > \lambda$) approximations are not valid. The result

of Mie scattering, for the case where $r \approx \lambda$, shows that the scattered light is mainly directed in the forward direction (Figure 3-5) [58].

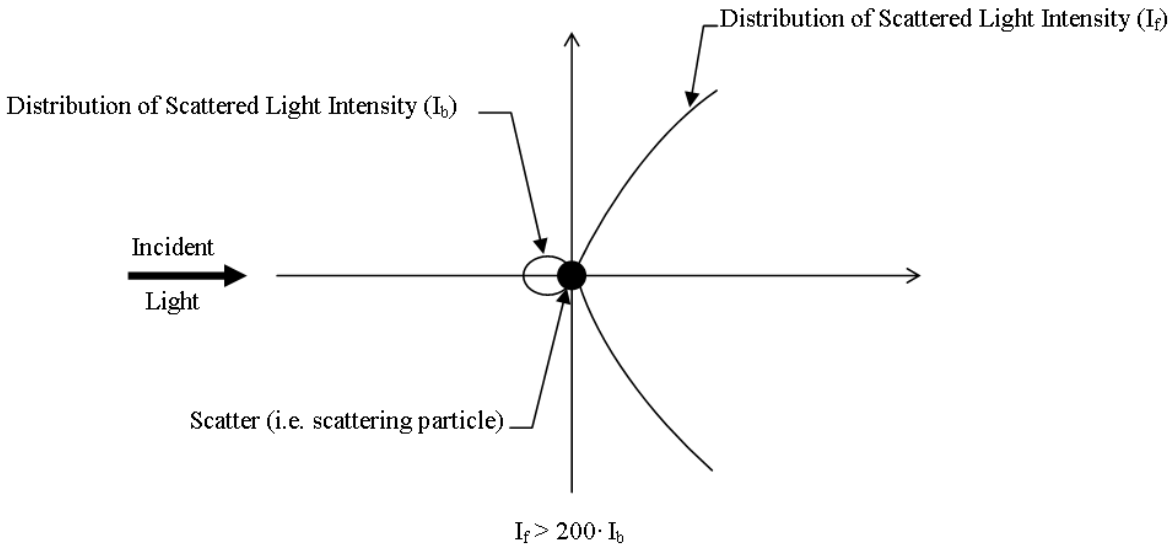

Figure 3-5 Mie Scattering

3.3. Absorption

Absorption is a way in which incident light or photon energy is extracted by the surrounding matter or absorber (Figure 3-6, modified from [55]) and it is considered one of the most important factors in biomedical optics. Based on the type of chromophores, there are two main ways the absorption may take place: (1) Absorption via electronic transitions and (2) absorption via vibrational and rotational transitions. The former is mostly associated with the absorption of light in the ultraviolet, visible, and near infrared regions of the electromagnetic spectrum. The latter is mostly associated with the absorption of light by water in infrared region of the electromagnetic spectrum.

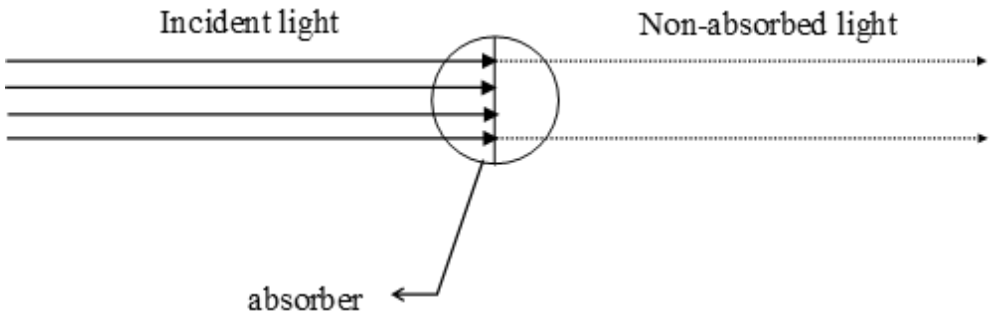

Figure 3-6 Light Absorption by an Absorber (i.e. chromophore)

As in the case of scattering, the concept of absorption cross section is introduced. The absorption cross section, σ_a, is defined [52] as the ratio of the absorbed power, P_a, to the initial intensity (power per unit area) of the incident wave, I_0:

$$\sigma_a = \frac{P_a}{I_0} \tag{3-7}$$

The σ_a can be viewed as the product of actual (i.e. geometric) cross sectional area of the absorber and the absorption efficiency of the absorber.

Similarly to scattering, the absorption cross section (in units of area) and density of absorbers (in number per volume), ρ_a, define the absorption coefficient (in units per length), μ_a:

$$\mu_a = \rho_a \cdot \sigma_a \tag{3-8}$$

The average distance that light travels before being absorbed is defined as the inverse of the coefficient of absorption, or $1/\mu_a$, and it is called the absorption mean free path, l_a. Furthermore, for a medium with a uniform distribution of absorbers, the absorption coefficient can be defined by differential change of intensity of collimated light beam, dI, crossing an infinitely small path length, dz, that yields transmitted light intensity, I:

$$\mu_a = -\frac{dI}{Idz} \tag{3-9}$$

Integrating equation (3-9) over a thickness *z* yields the expression for Beer-Lambert law:

$$I = I_0 e^{-\mu_a z} \tag{3-10}$$

$$A = \log_{10}\frac{I_0}{I} = \mu_a z \tag{3-11}$$

where A is the light attenuation or optical density, OD.

Absorption coefficient can also be written in terms of the molar extinction coefficient (at a specific wavelength λ), ε_λ, and the molar concentration of the absorber, *c*. The molar extinction coefficient can be looked as the absorbing power of the absorber where its variation represents an absorption spectrum of a particular absorber. Using ε_λ and *c* in place of μ_a, the Beer-Lambert law can be rewritten as:

$$I = I_0 e^{-\varepsilon_\lambda c z} \tag{3-12}$$

$$A = \log_{10}\frac{I_0}{I} = \varepsilon_\lambda c z \tag{3-13}$$

Therefore, the Beer-Lambert law provides a relationship between the amount of the absorbed light and the material through which the light is traveling. This law, however, has several limitations, one of them being that it only describes absorption of light in non-scattering medium. In order to be able to apply Beer-Lambert law to scattering medium, several modifications must be incorporated in the original formula.

First, a term that describes scattering losses must be added to the equation (3-13). This term is usually denoted by G and it is a geometry-depended factor [59]. Second, a multiplication term that describes increased optical path length due to the presence of scatters must be included,

as well. This term is usually referred to as the differential pathlength factor, DPF. Differential pathlength factor is the ratio of the actual optical distance, called differential pathlength, DP, and the medium thickness, z.

$$\mathrm{DPF} = \frac{\mathrm{DP}}{\mathrm{z}} \tag{3-14}$$

Incorporating modifications from above into the Beer-Lambert law, equation (3-13), yields the following relationship for the light absorption in highly scattering medium:

$$\mathrm{A} = \log_{10}\frac{\mathrm{I}_0}{\mathrm{I}} = (\varepsilon_\lambda \mathrm{cz})\mathrm{DPF} + \mathrm{G} \tag{3-15}$$

The equation (3-15) represents the Modified Beer-Lambert law. Due to difficulties in obtaining the scattering losses term, G, this equation cannot be used to obtain the absolute value of chromophore concentration, *c*, by measuring the absolute optical density, OD. If, however, it is assumed that the scattering losses remain constant for a specific medium during signal acquisition, then a change in chromophore concentration can be calculated by measuring a change in optical densities.

$$\mathrm{A}_1 = \log_{10}\frac{\mathrm{I}_0}{\mathrm{I}} = (\varepsilon_\lambda \mathrm{c}_1\mathrm{z})\mathrm{DPF} + \mathrm{G} \tag{3-16}$$

$$\mathrm{A}_2 = \log_{10}\frac{\mathrm{I}_0}{\mathrm{I}} = (\varepsilon_\lambda \mathrm{c}_2\mathrm{z})\mathrm{DPF} + \mathrm{G} \tag{3-17}$$

$$(\mathrm{A}_2 - \mathrm{A}_1) = (\varepsilon_\lambda \mathrm{c}_2\mathrm{z})\mathrm{DPF} + \mathrm{G} - (\varepsilon_\lambda \mathrm{c}_1\mathrm{z})\mathrm{DPF} - \mathrm{G} \tag{3-18}$$

$$(\mathrm{A}_2 - \mathrm{A}_1) = (\mathrm{c}_2 - \mathrm{c}_1)(\varepsilon_\lambda \mathrm{z} \cdot \mathrm{DPF}) \tag{3-19}$$

Thus, the Modified Beer-Lambert law could be used in situations where monitoring of changes in chromophore of interest is desired and changes in optical densities (i.e. light attenuation) are measured with the instrument.

3.4. Light Propagation in Tissue

Based on the scattering and anisotropy characteristics of tissue, tissue sampling depth is defined by the photon-path-distribution function for photons migrating from a source to a detector on the surface of the skin. Using the assumption that tissue is homogenously scattering medium, the spatial photon distribution function has a banana-like shape (Figure 3-7). If one considers weak absorption within the tissue, then the banana-like shape of the photon propagation in tissue is approximated by equation (3-20) [54], [60], [61], which describes a curve of the most probable direction of photon migration. From Figure 3-7 it is evident that the maximum sampled tissue depth, z_{max}, occurs approximately at the mid-point between the light source and the light detector (inter-optode distance). Therefore, setting the surface position x at the middle of inter-optode distance, r_{sd}, yields the value of the approximate maximum sampled tissue depth z_{max}, with respect to r_{sd}, as shown in equation (3-21).

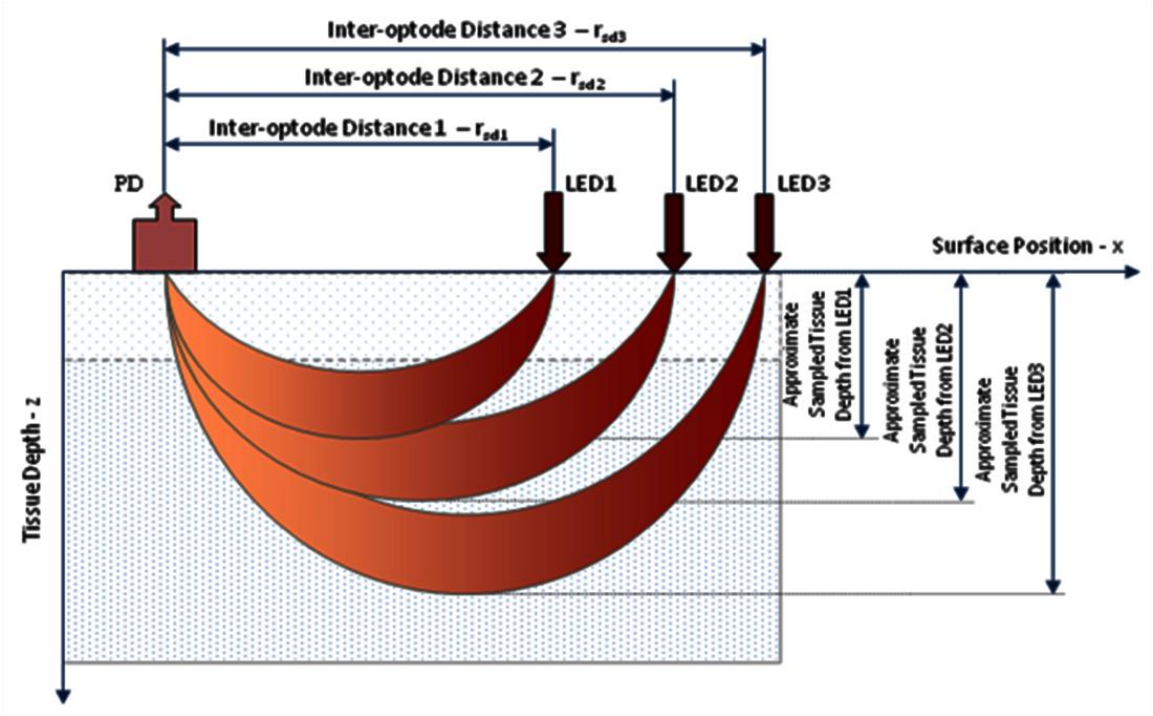

Figure 3-7 Light Propagation In Tissue

$$z \approx \sqrt{\left\{\frac{1}{8}\left[\sqrt{((x^2+(r_{sd}-x)^2)^2+32x^2(r_{sd}-x)^2)}-x^2-(r_{sd}-x)^2\right]\right\}} \qquad (3\text{-}20)$$

$$at\ x=\frac{r_{sd}}{2} \rightarrow z_{max} \approx \frac{r_{sd}}{2\sqrt{2}} = 0.354 \cdot r_{sd} \qquad (3\text{-}21)$$

where z is tissue depth, r_{sd} is inter-optode distance, and x is surface position.

3.5. Anatomy and Physiology Revisited

Human tissues contain a great number of inhomogeneous scatters and absorbers. Penetration of light in tissues, therefore, is greatly depended on the size and number of scatters, concentration of absorbers, as well as on the wavelength of incident light. There are three major tissue types in the lower leg that are of interest with respect to light scattering and absorption. These are skin,

adipose tissue, and muscle (Figure 3-8, modified from [62]). The main scatters and absorbers present in each of these tissues will be discussed next, as well as their effect on light propagation.

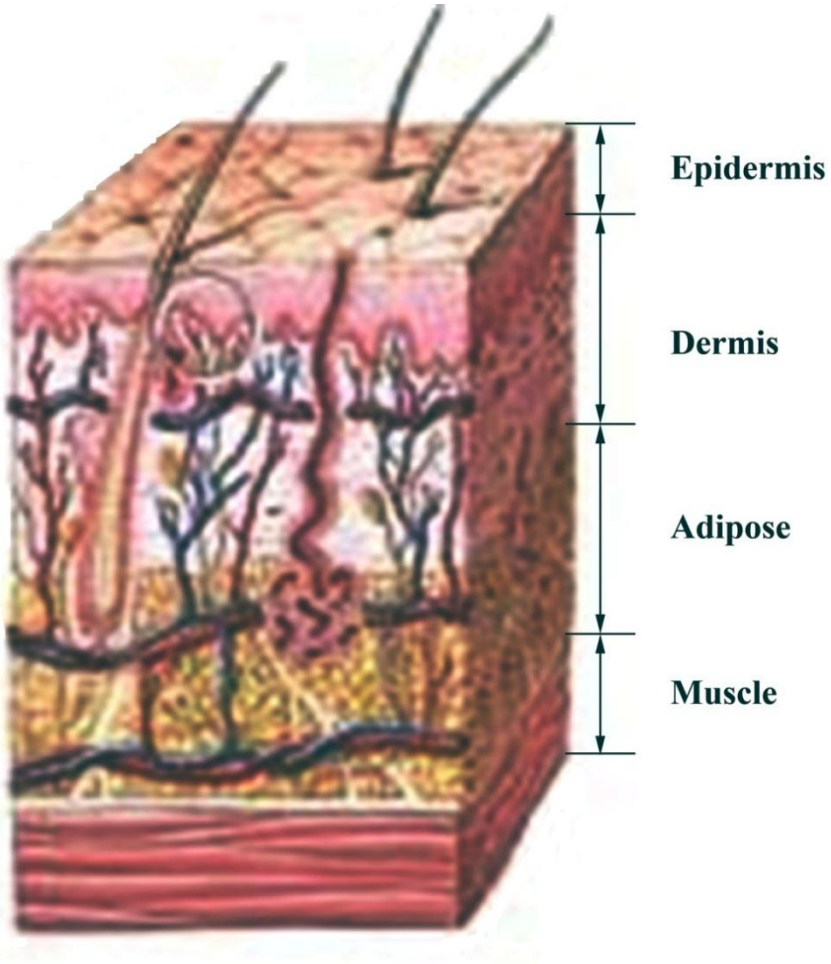

Figure 3-8 Lower Leg Tissue Layers

3.5.1. Skin

The skin is a part of the integumentary system whose function is to help regulate body temperature, protect body from physical damage and pathogens, and enable feelings of touch, heat, and cold. It is the largest organ of the body comprised of two primary layers: Epidermis and dermis (Figure 3-9, [63]). The epidermis is the top-most layer of the skin that provides

physical and pathogen protection, as well as helps maintain body hydration and temperature. It is comprised of stratum corneum, stratum lucidum, stratum granulosum, stratum spinosum, and stratum germinativum. The epidermis does not contain its own vasculature, however, its deeper layers obtain nutrients from the upper dermis through diffusion. Immediately below the epidermis is a layer of thin fibrous layer called basement membrane, which connects epidermis to dermis. The dermis consists of connective tissue and collagen fibers and it contains its own vasculature, hair follicles, sweat glands, and many mechanoreceptors. The primary function of dermis is to provide skin elasticity (connective tissue) and strength (collagen fibers), as well as to house appendages of the skin.

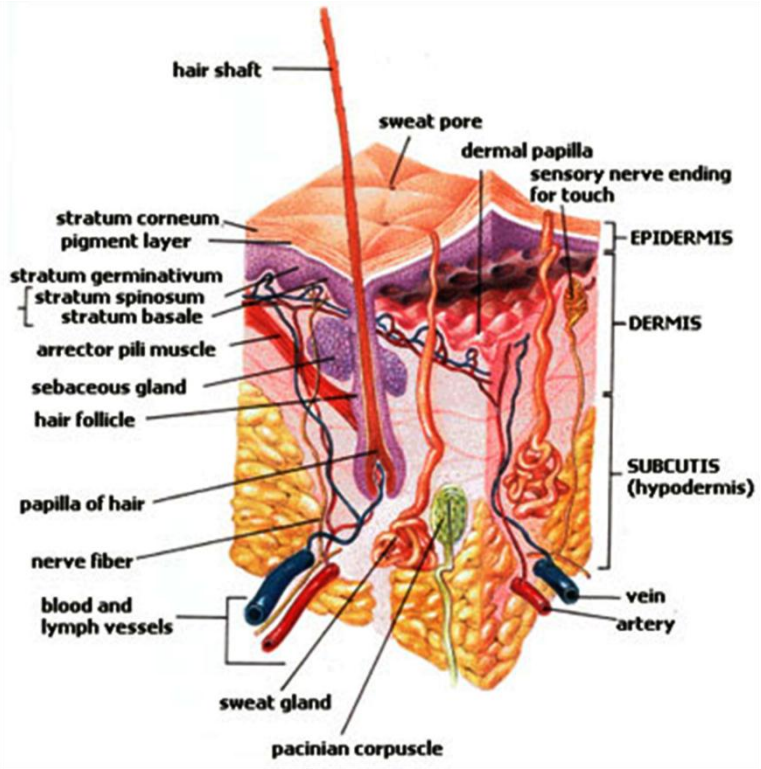

Figure 3-9 Skin Layers

Visible and near infrared light scattering in the skin can be explained using the Mie Theory, for large collagen fibers, and Rayleigh Theory, for small cellular structures. The epidermis scattering results primarily from keratin fibers while dermis scattering results primarily from large and small collagen fibers. Due to small epidermis thickness, its contribution to the total skin scattering is negligible [64]. Equations (3-22) through (3-25) describe approximate reduced scattering coefficient, μ'_s (λ_{total}), of dermis:

$$\mu'_s(\lambda_{Mie}) = 2x10^5 \cdot \lambda^{-\frac{3}{2}} \left[\frac{1}{cm}\right] \tag{3-22}$$

$$\mu'_s(\lambda_{Rayleigh}) = 2x10^{12} \cdot \lambda^{-4} \left[\frac{1}{cm}\right] \tag{3-23}$$

$$\mu'_s(\lambda_{total}) = \mu'_s(\lambda_{Mie}) + \mu'_s(\lambda_{Rayleigh}) \tag{3-24}$$

$$\mu'_s(\lambda_{total}) = 2x10^5 \cdot \lambda^{-\frac{3}{2}} + 2x10^{12} \cdot \lambda^{-4} \left[\frac{1}{cm}\right] \tag{3-25}$$

As mentioned above, absorption of light in tissue is caused by chromophores. Skin contains several chromophores in the visible and near infrared light region, including melanin, hemoglobin, water, and fat (i.e. adipose tissue). The first two chromophores, melanin and hemoglobin, are considered to be the primary absorbers in the skin (i.e. the principal absorption chromophores). Melanin is found in epidermis and, for the visible and near infrared light regions, has greater absorption coefficient than hemoglobin. Absorption contribution from hemoglobin comes from whole cutaneous blood in dermis layer of the skin. Skin absorption for both epidermis and dermis is defined by the baseline skin absorption, the principal absorption chromophore, and volume fraction of the principal absorption chromophore. The volume fraction of the principal chromophore in epidermis varies greatly from person-to-person and is in the range of 1.3 percent for fair-skinned individuals up to 43 percent for individuals with dark

skin. The volume fraction of the principal chromophore in dermis averages 0.2 percent, but it has local superficial volume fractions which range from two to five percent. Equation (3-26) shows baseline absorption coefficient approximation for both epidermis and dermis layers. It was derived empirically using bloodless and melanin-less rat skin [64]. For epidermis, the principal absorption coefficient of melanin is approximated using the expression in equation (3-27). Combining equations (3-26) and (3-27) and taking into the account approximate volume fraction of melanosomes in epidermis, f_{volm}, for specific person, yields the total absorption coefficient for epidermis, $\mu_a(\lambda_{epidermis})$, as described in equation (3-28).

$$\mu_a(\lambda_{baseline}) = 0.244 + 85.3^{-\left(\frac{\lambda-154}{66.2}\right)} \left[\frac{1}{cm}\right] \tag{3-26}$$

$$\mu_a(\lambda_{melanin}) = (6.6x10^{11}) \cdot \lambda^{-3.33} \left[\frac{1}{cm}\right] \tag{3-27}$$

$$\mu_a(\lambda_{epidermis}) = f_{volm} \cdot \mu_a(\lambda_{melanin}) + (1 - f_{volm}) \cdot \mu_a(\lambda_{baseline}) \left[\frac{1}{cm}\right] \tag{3-28}$$

For dermis, the principal absorption coefficient of whole blood, $\mu_a(\lambda_{blood})$, is found from Figure 3-10 (data from [65]). Combining equation (3-26), value of absorption coefficient, $\mu_a(\lambda_{blood})$, and volume fraction of whole blood in dermis layer, , f_{volb}, yields the total absorption coefficient for dermis, $\mu_a(\lambda_{dermis})$, as described in equation (3-29).

$$\mu_a(\lambda_{dermis}) = f_{volb} \cdot \mu_a(\lambda_{blood}) + (1 - f_{volb}) \cdot \mu_a(\lambda_{baseline}) \left[\frac{1}{cm}\right] \tag{3-29}$$

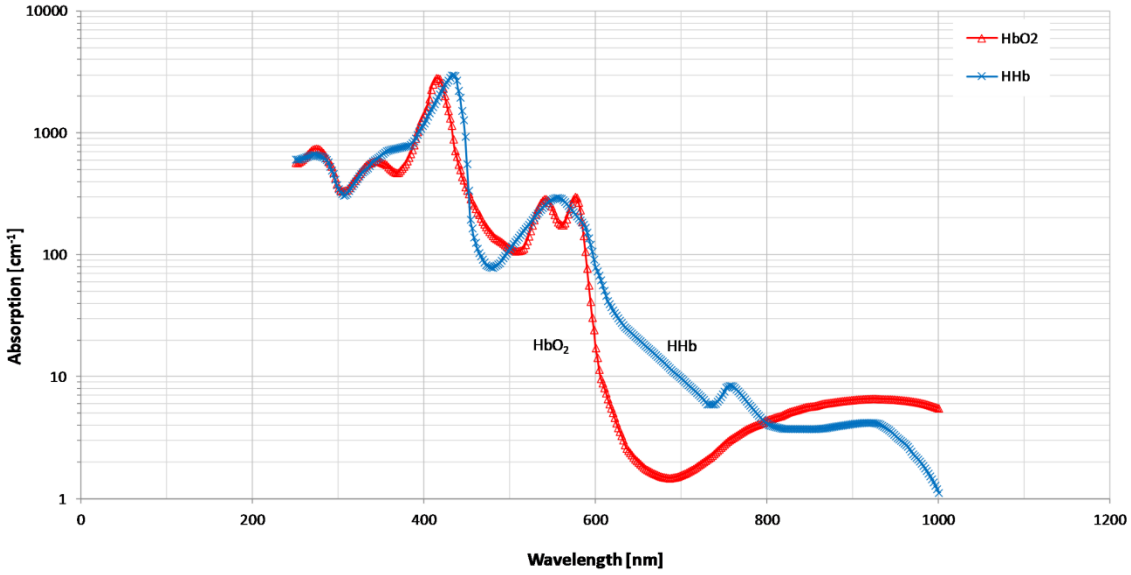

Figure 3-10 Absorption Spectra of Hemoglobin

Below dermis is a subcutaneous tissue layer which serves as the bond between the skin and the underlying muscle or bone. Subcutaneous (i.e. adipose tissue) layer is mainly composed of adipocytes and contains arteries, veins and nerves.

3.5.2. Adipose Tissue

Human body stores considerable quantities of fat in two primary tissues, adipose tissue and the liver. The former is located below the skin and is often referred to as fat deposits or simply fat. Adipose tissue has two main functions in the body: (1) It stores triglycerides that are used to provide energy in the body and (2) it provides a layer of thermal insulation for the body [18]. The main constituent of adipose tissue is cell called adipocyte, which ranges in size from 15 to 250 μm and in concentrations of up to 95 percent. These cells store triglycerides in the form of liquid and form small fat droplets located within the structural network of reticular fibers. In addition, the adipose tissue intracellular space contains a number of capillaries, which envelope

each adipose cell [66]. It is believed that scattering in adipose tissue is primarily caused by the light interaction with fat droplets and structural fibers, while absorption is attributed primarily to adipocytes and hemoglobin. Figure 3-11 (data from [65]) shows absorption spectra of fat in the visible and near infrared region.

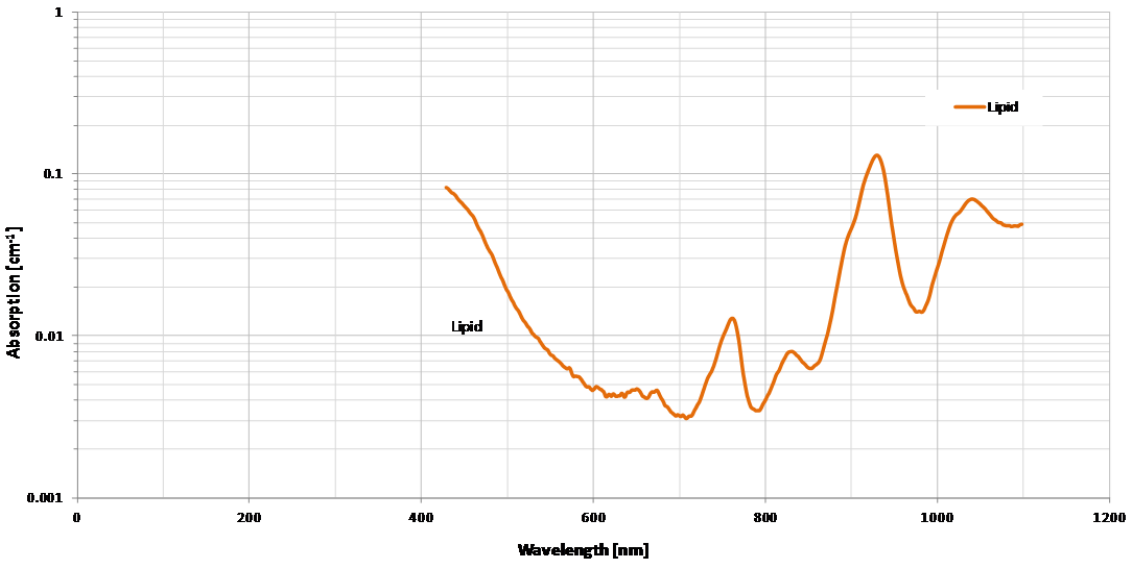

Figure 3-11 Absorption Spectra of Fat

3.5.3. Muscle

Skeletal muscles account for approximately forty percent of the human body. These muscles (Figure 3-12, [68]) are made up of a large number of myofibrils, a cylinder-like structures of about 1-2 μm in diameter, that are grouped in individual units called muscle fibers. Intra-myofibril space is filled with sarcoplasm or cellular organelles [67]. Each muscle fiber is approximately 10-80 μm in diameter and is surrounded by a thin layer of connective tissue called endomysium. Muscle fiber usually contains a single nerve ending near its mid-point. A group of muscle fibers are further assembled in larger units known as fascicles, which are encircled by a

layer of connective tissue called perimysium. Fascicles contain blood vessels and nerves that serve individual muscle fibers. Large numbers of fascicles are surrounded by a dense irregular connective tissue layer called epimysium and comprise a single muscle. Finally, a group of muscles are covered by a protective layer of dense fibrous connective tissue called deep fascia (Section 2.1).

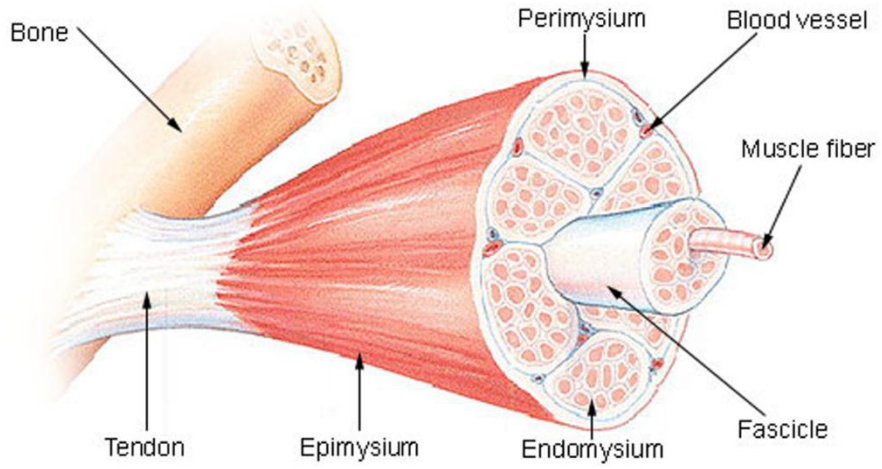

Figure 3-12 Structure of Skeletal Muscle

Due to their structure, skeletal muscles are optically anisotropic. Linear muscle fibers have higher refractive index along the fiber than in the direction perpendicular to fiber propagation [54]. In addition to directional dependence of refractive index, scattering in muscles is primarily caused by myofibrils and sarcoplasm while the absorption of visible and near infrared light is primarily caused by hemoglobin, which originates in the dense vascular network of muscle fascicles, and water. Figure 3-13 (data from [65]) shows absorption spectra of oxygenated hemoglobin, deoxygenated hemoglobin, and water.

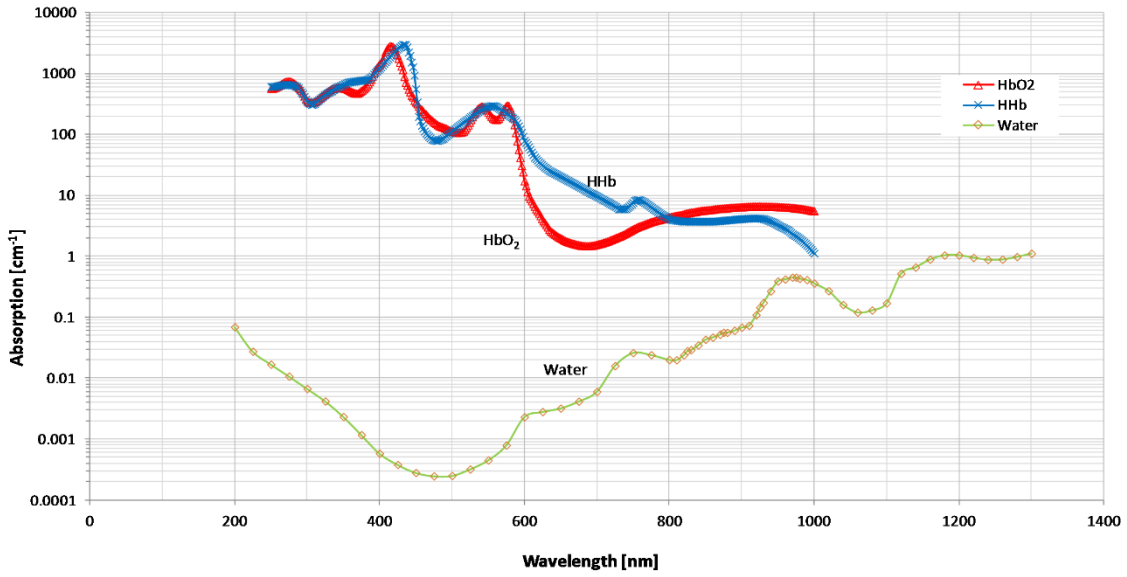

Figure 3-13 Absorption Spectra of Oxygenated and Deoxygenated Hemoglobin and Water

3.6. Monte Carlo Simulations

3.6.1. Background

Monte Carlo [MC] is a technique which uses a stochastic model to simulates physical processes [69]. It was first used to simulate laser-tissue interactions by Wilson [70] in 1983. Since then, many different computer applications, which use Monte Carlo techniques, have been developed to simulate light-tissue interactions. One of these applications is Monte Carlo modeling of photon transport in multi-layered tissue [MCML] developed by Wang *et al.* [71]. This application has been used and tested extensively throughout the years.

3.6.2. General MC Method

Monte Carlo technique implemented in MCML uses method described by Prahl *et al.* [72]. In this scheme, during each cycle, a photon, which has certain weight assigned to it, is moved a

small distance Δs after which its status is checked to verify if it was scattered, absorbed, propagated undisturbed, internally reflected, or if it left the tissue. The photon is followed until it is either absorbed or it has left the tissue sample under observation. In the case of the former, the position of the event is noted, while in the case of the latter, the values of reflection or transmission are noted, as applicable. The photon continues to propagate as long as its weight is above certain minimum value. If the photon weight falls below the minimum value, then "roulette" is used to determine if the photon should continue propagation in tissue or if it should be terminated. In the latter case, a new photon is then launched into the tissue and the process is repeated. Based on mathematical models, the recorded photon absorption position, reflection, and transmission will approach actual values as the number of launched photons approaches infinity. Figure 3-14 (recreated from [72]) shows the MC process for photon propagation in tissue.

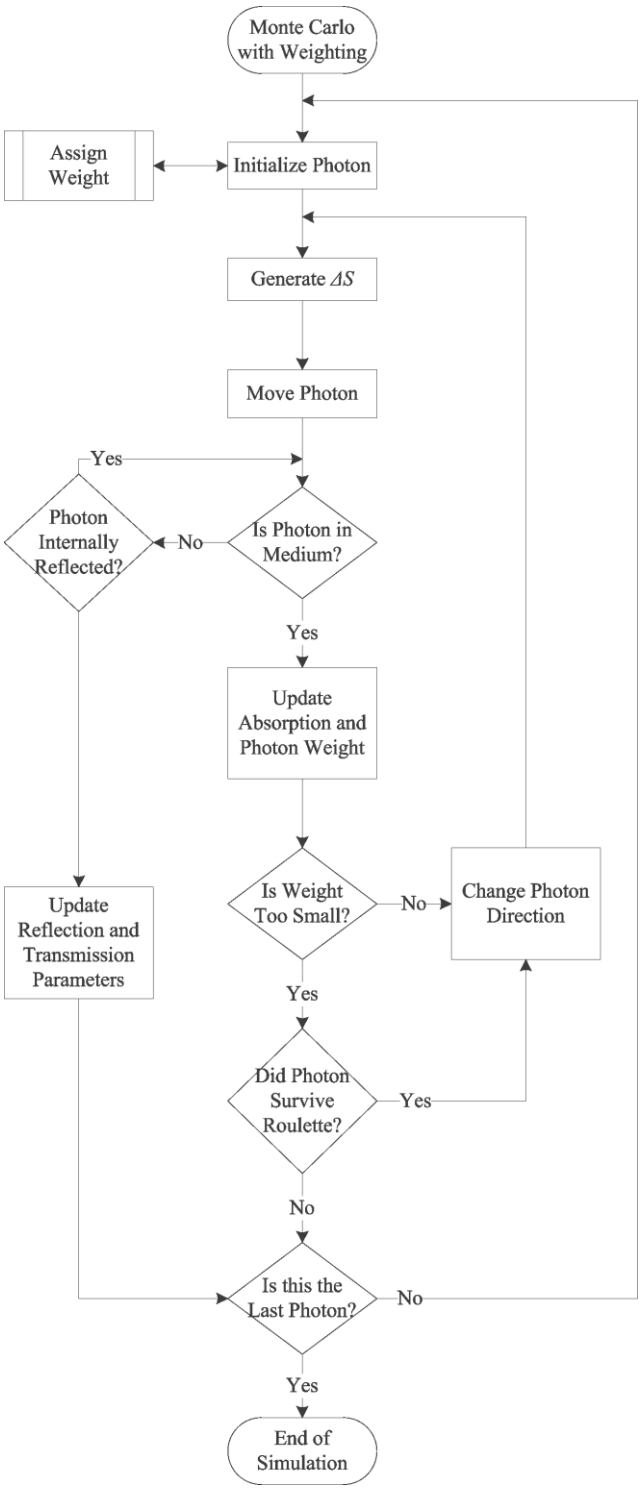

Figure 3-14 Monte Carlo Technique Implemented in MCML

3.6.3. "Dynamic" MC Application

The current MC simulations in MCML are "static." As defined here, the "static" refers to the fact that all simulation parameters are input at the beginning of the simulation run. If any of the parameters are to be changed, then a new simulation profile must be run for each changed parameter. In addition, the simulation data results need to be compiled from different runs manually. In order to enable a more optimized simulation of different pathologies and their effect on light propagation in tissue, we developed a MATLAB® application which allows us to conduct "dynamic" MC simulations.

The newly developed MATLAB® application utilizes existing MCML and Finite Beam Calculations [CONV] as the engines for running dynamic Monte Carlo simulations in tissue models with changing optical properties. A summary of optical tissue properties, their change, and possible pathology they may simulate is presented in Table 3-1. In addition to setting the MCML values of several tissue model parameters (Table 3-6), the application allows the user to set a range of values for one of those parameters indicating how it will change in time during simulation run. We implemented this dynamic capability into MC simulations as a way to simulate how changes in tissue optical properties may be used to simulate different pathologies, such as venous occlusion.

Table 3-1 Changes in Optical Tissue Properties and Possible Simulated Pathologies

Parameter	Change	Simulated Pathology
μ_a (HbO_2)	↑	Reperfusion
μ_a (HbO_2)	↓	Ischemia
μ_s'	↓	Increased compartment pressure (denser tissue yields less scattering)
z	↑	Edema, hemorrhage, occlusion
μ_a (HbO_2) → μ_a (H_2O)		Edema

3.6.4. Results of "Dynamic" MC Simulation

Based on the known pathophysiology of acute compartment syndrome (Section 2.3) and near infrared spectroscopy device operation, Monte Carlo simulation profiles or models were created for NIR (Figure 3-15) and visible (Figure 3-16) light sources using deoxygenated blood as the dynamic (i.e. changing) layer. MC models consisted of five layers: Skin, adipose tissue, muscle, blood, and muscle. For the skin layer, we used optical parameters that were measured on a sample that included epidermis, dermis, and some underlying tissue structures. Optical tissue parameters for dynamic Monte Carlo simulations were obtained from [73] and are summarized in Table 3-2.

NIR Light Simulation Parameters

Combined Skin (2 mm) **n = 1.55; μ_s = 70 1/cm; g = 0.8; μ_a = 3.1 1/cm; λ = 633 nm**
Adipose (3 mm) **n = 1.44; μ_s = 83 1/cm; g = 0.86; μ_a = 2.6 1/cm; λ = 1064 nm**
Muscle 1 (3 mm) **n = 1.37; μ_s = 215 1/cm; g = 0.96; μ_a = 2 1/cm; λ = 1064 nm**
Deoxygenated Blood, Hct = 0.41 (1-5 mm) **n = 1.35; μ_s = 668 1/cm; g = 0.992; μ_a = 1.68 1/cm; λ = 960 nm**
Muscle 2 (30 mm) **n = 1.37; μ_s = 215 1/cm; g = 0.96; μ_a = 2 1/cm; λ = 1064 nm**

Figure 3-15 NIR Light Tissue Layers Optical Parameters for MC Simulations

Visible Light Simulation Parameters

Combined Skin (2 mm) **n = 1.55; μ_s = 70 1/cm; g = 0.8; μ_a = 3.1 1/cm; λ = 633 nm**
Adipose (3 mm) **n = 1.44; μ_s = 83 1/cm; g = 0.86; μ_a = 2.6 1/cm; λ = 1064 nm**
Muscle 1 (3 mm) **n = 1.37; μ_s = 530 1/cm; g = 0.8; μ_a = 11.2 1/cm; λ = 515 nm**
Deoxygenated Blood, Hct = 0.41 (1-5 mm) **n = 1.35; μ_s = 509 1/cm; g = 0.995; μ_a = 4.87 1/cm; λ = 665 nm**
Muscle 2 (30 mm) **n = 1.37; μ_s = 530 1/cm; g = 0.8; μ_a = 11.2 1/cm; λ = 515 nm**

Figure 3-16 Visible Light Tissue Layers Optical Parameters for MC Simulations

Table 3-2 Simulated tissue layers and optical parameters for Monte Carlo simulations

Layer	Tissue (*in vitro*)	Index of Refraction, *n*	Scattering Coefficient, μ_s [cm^{-1}]	Absorption Coefficient, μ_a [cm^{-1}]	Anisotropy, *g*
1	***Skin (2mm)***	1.55*			
	633nm		70	3.1	0.80
2	***Adipose(3mm)***	1.44			
	1064nm		83	2.6	0.86
3	***Muscle (3mm)***	1.37			
	515nm		530	11.2	
	1064nm		215	2	0.96
4	***Blood (Hct = 0.41) (1mm – 5mm) Deoxygenated***	1.35			
	665nm		509	4.87	0.995
	960nm		668	1.68	0.992
5	***Muscle (30mm)***	1.37			
	515nm		530	11.2	
	1064nm		215	2	0.96

** value refers to stratum corneum*

In our Monte Carlo simulations, dynamic layer (i.e. deoxygenated blood) was varied from 0.1 centimeter (i.e. baseline) to 0.5 centimeter (i.e. venous occlusion), in 0.1 centimeter increments. This simulated pooling of venous blood during lower leg venous occlusion. Each simulation was run using 100 million photons with incident light beam of 1 milliwatt power. Depth and radial grids, *dz* and *dr*, respectively, were set to 1 millimeter resolution, while convolution beam and sensor sizes were set to 0.3 centimeters, each.

Results of MC simulations have shown that expected NIR light intensities at the surface range from several nanowatts to several hundred nanowatts (Table 3-3). Based on these results, electronic circuit for the novel NIRS system must provide the transimpedance gain of at least 1 million in order to obtain optical voltage levels suitable for analog-to-digital conversion (Section 4.2.1.2). Plots of NIR light intensities (log scale) for different sensor positions versus dynamic

layer thickness are shown in Figure 3-18. As expected, the increase in dynamic layer thickness from 0.1 to 0.5 centimeters caused reduction in detected light intensity due to the fact that more light was absorbed by the chromophore of interest (i.e. deoxy hemoglobin). In order to better understand dependence of expected light intensity at specific sensor position versus varying dynamic layer thickness, we calculated percent change of intensities with respect to baseline thickness value as follows:

$$NIR_d = \frac{NIR\ (d_t) - NIR\ (d_b)}{NIR\ (d_t)} \cdot 100\% \qquad (3\text{-}1)$$

where
NIR (d_b) is data at simulated baseline (d = 0.1cm)
NIR (d_t) is data at simulated venous occlusion (d = 0.2, 0.3, 0.4, 0.5cm)

Using equation (3-1) and NIR light intensity values from Table 3-3, the percent change values were plotted in Figure 3-17. The plot shows that light intensity experiences greater percent change for thicker dynamic layer values and for more distal sensors. These results may be attributed to two factors: First, thicker dynamic layers offer greater absorption of incident light and hence cause greater change in its intensity at the surface versus baseline; second, the more distal sensors detect smaller absolute light intensities (Figure 3-18) than proximal sensors and hence smaller changes in layer thickness result in greater percent change.

Table 3-3 NIR Light Intensities for Each Sensor with Deoxy Blood as Dynamic Layer

Sensor / Thickness	*0.1cm*	*0.2cm*	*0.3cm*	*0.4cm*	*0.5cm*
NIR-1	3.978E-09	3.408E-09	2.992E-09	2.790E-09	2.727E-09
NIR-2	5.210E-09	4.945E-09	4.631E-09	3.636E-09	3.541E-09
NIR-3	8.320E-09	7.908E-09	6.568E-09	6.393E-09	5.603E-09
NIR-4	1.172E-08	1.137E-08	9.161E-09	9.109E-09	8.179E-09
NIR-5	1.971E-08	1.869E-08	1.740E-08	1.588E-08	1.359E-08
NIR-6	4.042E-08	3.709E-08	3.304E-08	3.221E-08	2.908E-08
NIR-7	9.018E-08	8.296E-08	7.830E-08	7.299E-08	6.665E-08
NIR-8	2.569E-07	2.422E-07	2.240E-07	2.055E-07	1.945E-07

NIR-1 – most distal sensor; NIR-8 – most proximal sensor

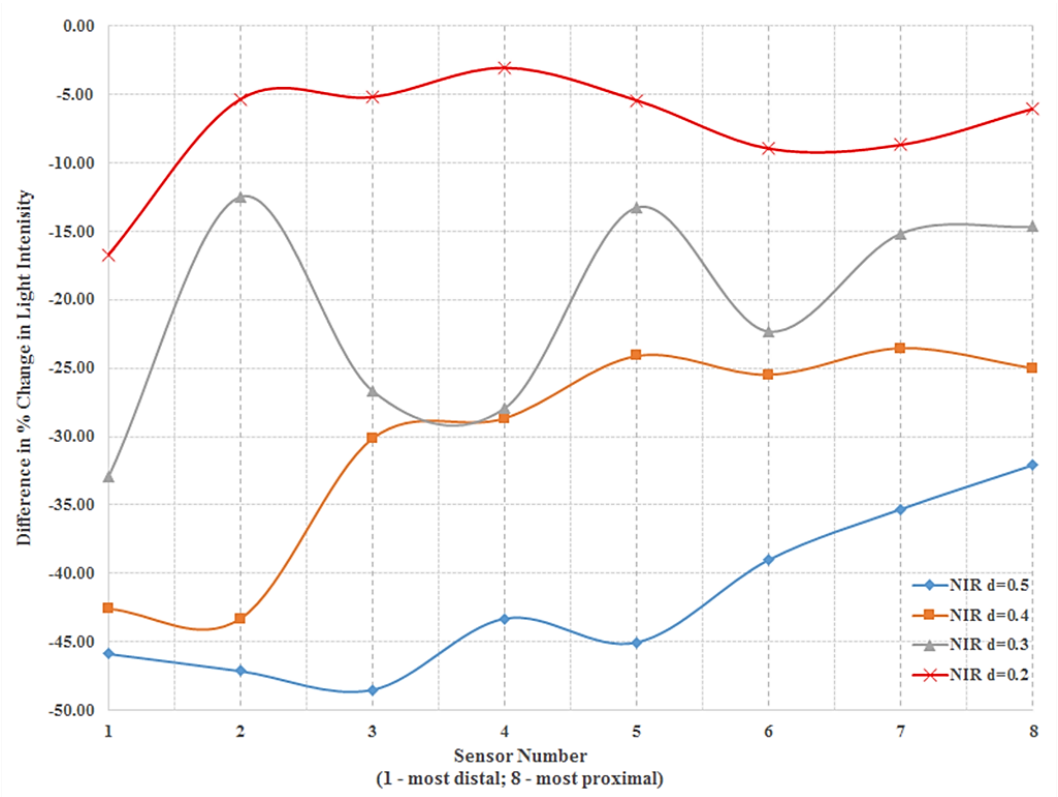

Figure 3-17 Percent Change of NIR Light for Varying Dynamic Layer Thicknesses Versus Sensor Number (Position)

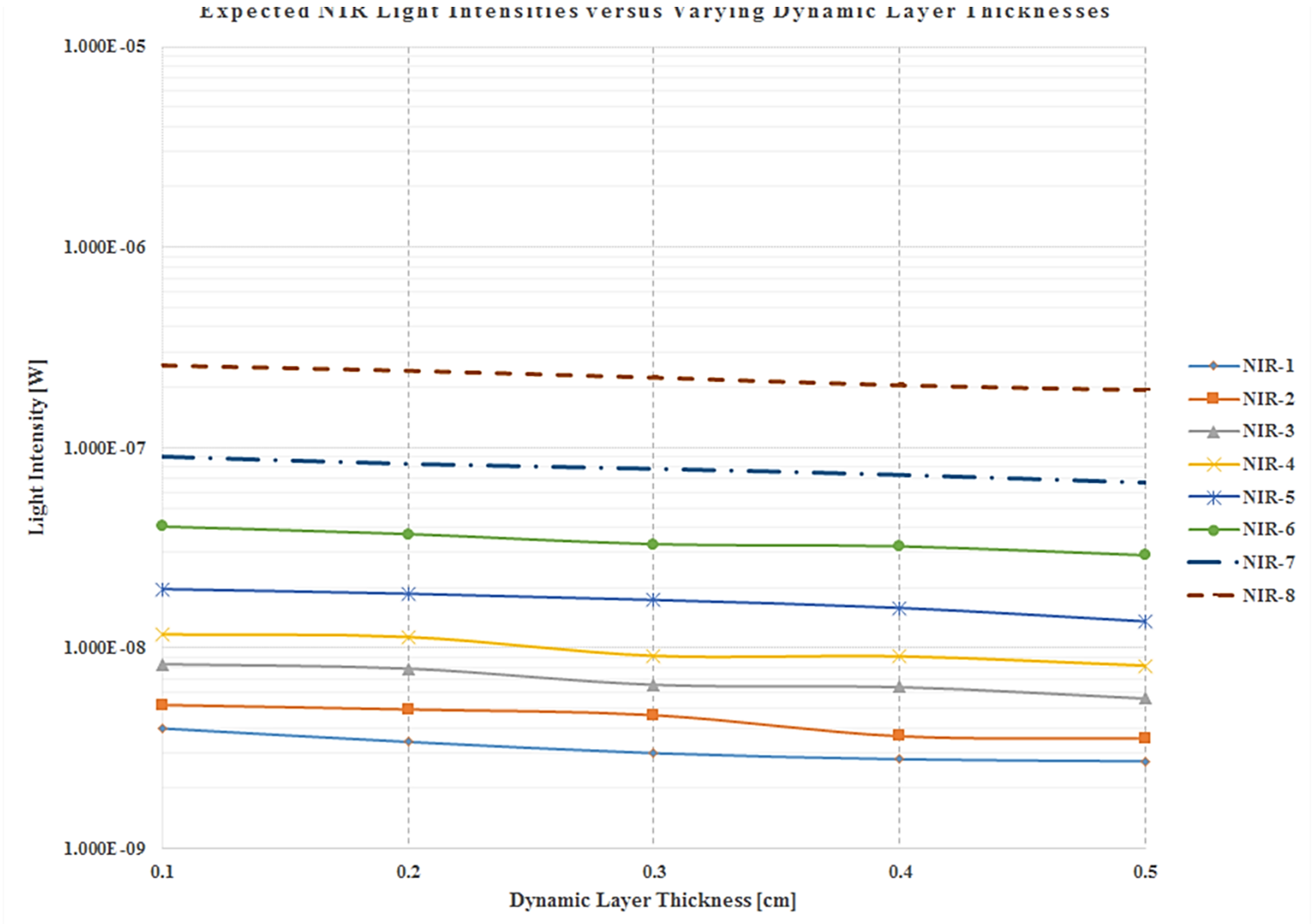

Figure 3-18 Simulation Results for Expected NIR Light Intensities versus Sensor Position for Different Dynamic Layer Thicknesses (NIR-1 is most distal sensor; NIR-8 is most proximal sensor)

In addition to NIR light, visible light simulations were also completed. The results showed that expected visible light intensities at the surface range from hundreds nanowatts to several milliwatts (Table 3-4). This indicates that electronic circuit for the novel NIRS system must provide visible light transimpedance gain in the range of several hundred thousand to approximately one million. Based on these gain values and values obtained from NIR light simulations above, iterative approach in the design of amplification gain stage should be implemented in order to determine optimal gain values for both NIR and visible light sensors. Plots of visible light intensities (log scale) for different sensor positions versus dynamic layer thickness are shown in Figure 3-20. Similarly to NIR light, the increase in dynamic layer thickness from 0.1 to 0.5 centimeters caused reduction in detected light intensity due to the fact that more light was absorbed by the chromophore of interest. The visible light intensity levels, however, are approximately an order of magnitude greater than the values obtained for NIR light. This could be explained by an order of magnitude difference in the absorption spectra (Figure 3-21) of deoxygenated hemoglobin for visible light wavelengths (e.g., 650nm) and NIR light wavelengths (e.g., 950nm). As in the case of NIR light intensities, we calculated percent change of visible light intensities with respect to baseline thickness value as follows:

$$Vis_d = \frac{Vis(d_t) - Vis\,(d_b)}{Vis\,(d_t)} \cdot 100\% \qquad (3\text{-}2)$$

where
Vis (d_b) is data at simulated baseline (d = 0.1cm)
Vis (d_t) is data at simulated venous occlusion (d = 0.2, 0.3, 0.4, 0.5cm)

Using equation (3-2) and visible light intensity values from Table 3-4, the percent change values were plotted in Figure 3-19. The visible light results are analogous to NIR light intensity findings.

Table 3-4 Visible Light Intensities for Each Sensor with Deoxy Blood as Dynamic Layer

Sensor / Thickness	*0.1cm*	*0.2cm*	*0.3cm*	*0.4cm*	*0.5cm*
Vis-1	1.682E-07	1.617E-07	1.539E-07	1.485E-07	1.408E-07
Vis-2	2.201E-07	2.112E-07	2.022E-07	1.933E-07	1.870E-07
Vis-3	2.882E-07	2.827E-07	2.675E-07	2.585E-07	2.497E-07
Vis-4	3.861E-07	3.686E-07	3.551E-07	3.365E-07	3.265E-07
Vis-5	5.587E-07	5.455E-07	5.406E-07	5.278E-07	5.162E-07
Vis-6	9.708E-07	9.491E-07	9.380E-07	9.226E-07	8.958E-07
Vis-7	1.875E-06	1.846E-06	1.794E-06	1.737E-06	1.715E-06
Vis-8	4.080E-06	3.951E-06	3.860E-06	3.747E-06	3.693E-06

Vis-1 – most distal sensor; Vis-8 – most proximal sensor

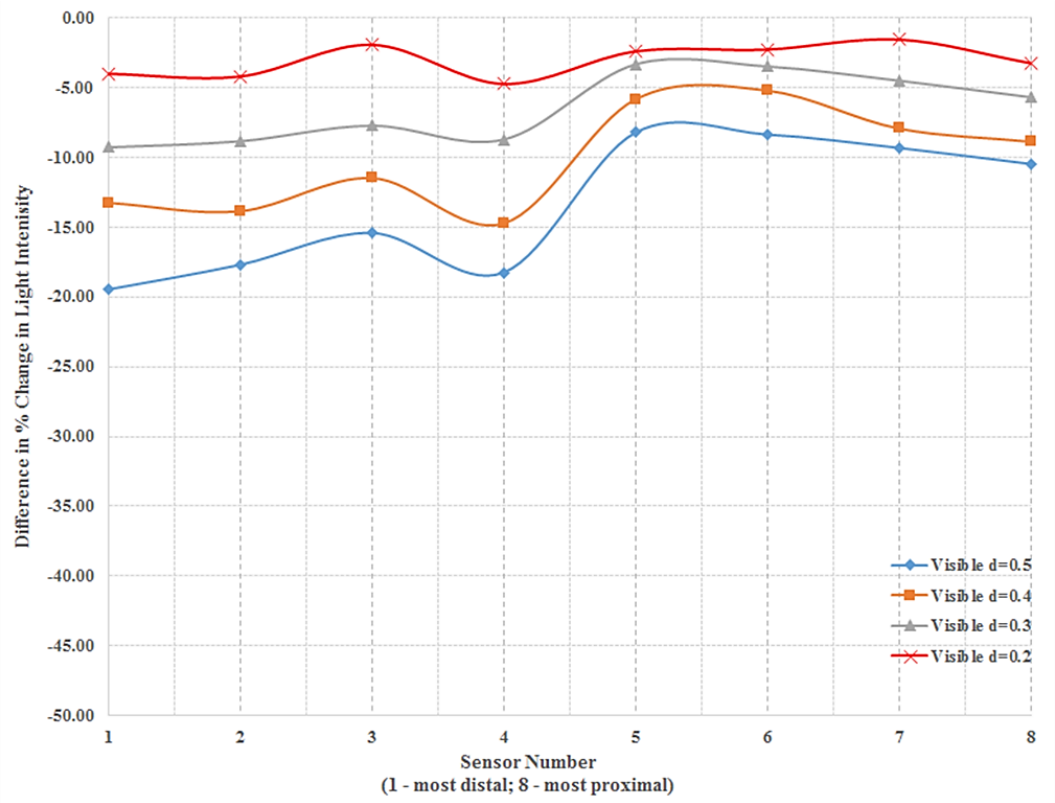

Figure 3-19 Percent Change of Visible Light for Varying Dynamic Layer Thicknesses Versus Sensor Number (Position)

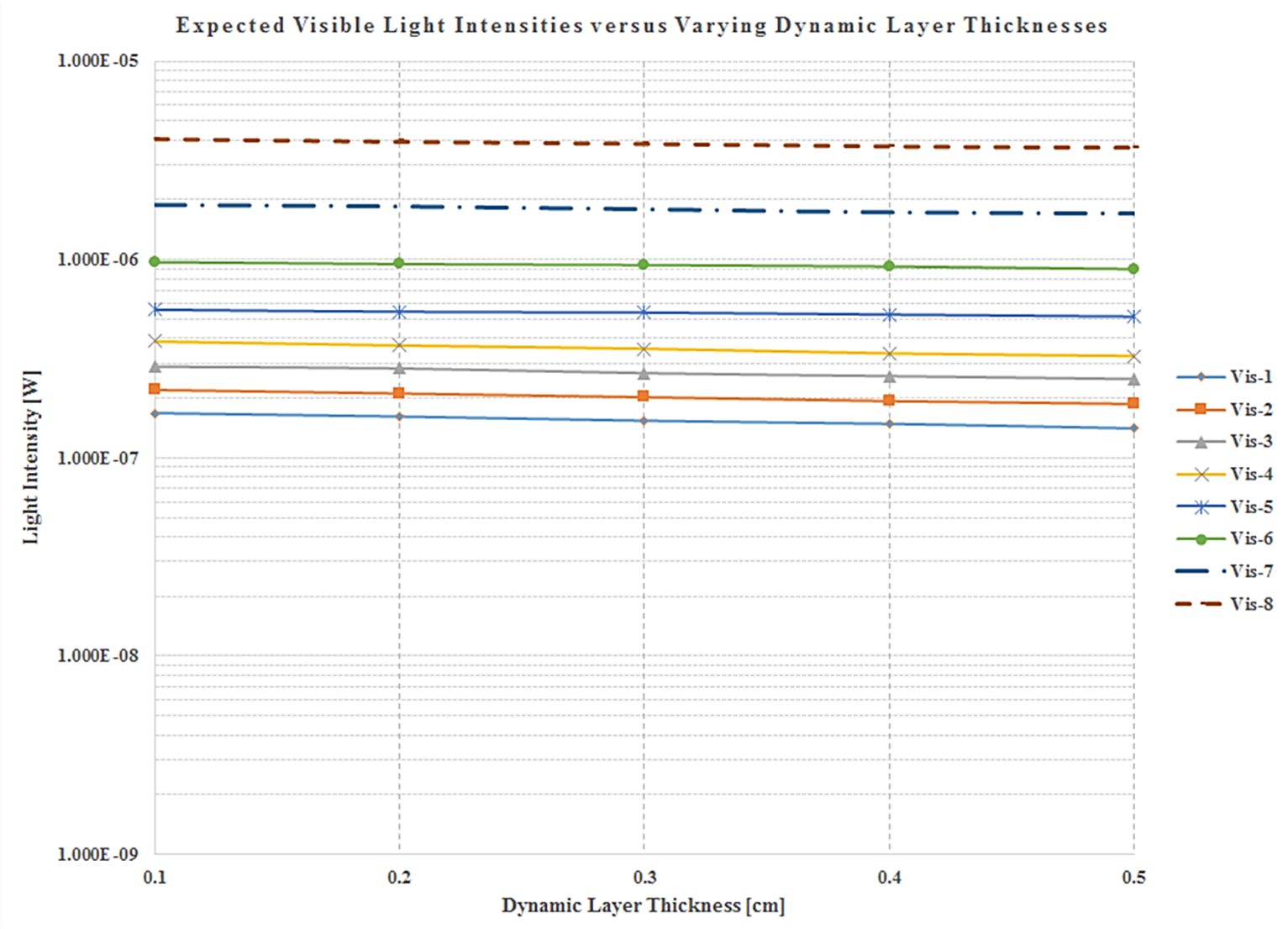

Figure 3-20 Simulation Results for Expected Visible Light Intensities versus Sensor Position for Different Dynamic Layer Thicknesses (Vis-1 is most distal sensor; Vis-8 is most proximal sensor)

The above simulation results should be taken only as a starting point for the development of the novel NIRS system due to several limiting factors. First, MC simulation values of optical tissue parameters (Table 3-2) were obtained from either fresh or frozen *ex vivo* tissue samples and may therefore be different from optical parameters present in live tissues [74]. Second, optical parameters were obtained by different investigators using sources at different wavelengths. Furthermore, optical parameters for combined skin and adipose tissues were only obtained at single wavelengths, 633 nm and 1064 nm, respectively; thus, they provide a source of error for NIR and visible light simulation runs, respectively. Third limiting factor is the fact that the muscle fascia was not included in the simulation models due to lack of optical parameter values. Muscle fascia consists of collagen fibers that are highly scattering for visible and NIR light. Finally, the MC model was created as layered structure of individual tissues. This model is not anatomically correct and presents a considerable limitation for these MC simulations.

3.7. Summary

This chapter provided an overview of theory of operation of near infrared spectroscopy devices. In particular, this chapter described three main physical phenomena that occur between the light and human tissue. The first phenomenon was partial reflection and partial transmission of incident light at tissue surface. This phenomenon is caused by the refractive index mismatch between the medium above the tissue (e.g., air) and the tissue itself. The second phenomenon discussed in this chapter was scattering. Light scattering is a process where light trajectory is changed due to local non-uniformities. Based on the size of non-uniformities and wavelength of light, the scattering can be explained by two different theories: Rayleigh scattering ($r << \lambda$) and Mie scattering, which is valid for any particle size. The third light-tissue interaction

phenomenon described in this chapter was absorption. Absorption is a way in which incident light or photon energy is extracted by the surrounding matter or absorber. It is considered one of the most important factors in biomedical optics. Based on initial and detected light intensities, attenuation of light (i.e. optical density) was described using Beer-Lambert law and the change in optical densities (e.g., pre and post event) was described via Modified Beer-Lambert law.

In addition, the effects three lower-leg tissue types have on the visible and near infrared light propagation were discussed. These three tissue types are: Skin, adipose tissue, and muscle. The main scatters and absorbers present in each of these tissues were discussed and are summarized in Table 3-5. Furthermore, a summary of scattering coefficient, absorption coefficient, and anisotropy values for epidermis, dermis, combined skin, adipose tissue, and muscle are presented in Table 3-6 [73]. This chapter also presented absorption spectra of the five main chromophores found in each of these tissues (Figure 3-21, data from [65]). Finally, a dynamic Monte Carlo simulations were performed to simulate the venous occlusion as the precursor to the onset of acute compartment syndrome. The results of these simulations have shown that intensities of expected optical signals range from nanowatts for NIR to milliwatts for visible light sources. These expected optical signal values provide a good starting point for the design of analog signal amplification section, as detailed in the next chapter.

Table 3-5 Summary of the main scatters and absorbers found in the lower-leg tissues for visible and near infrared light

Tissue	Scatter	Absorber
Skin		
Epidermis	Keratin	Melanin
Dermis	Collagen Fibers	Oxygenated and Deoxygenated Hemoglobin
Adipose Tissue	Fat droplets Structural Fibers	Adipocytes Oxy and Deoxy Hemoglobin
Muscle	Myofibrils Sarcoplasm	Oxy and Deoxy Hemoglobin Water

Table 3-6 Summary of index of refraction, scattering and absorption coefficients, and anisotropy values for the three main tissue types of the lower leg and blood

Tissue (*in vitro*)	Index of Refraction, *n*	Scattering Coefficient, μ_s [cm^{-1}]	Absorption Coefficient, μ_a [cm^{-1}]	Anisotropy, *g*
Skin				
Epidermis	1.55*			
633nm		450	35	0.80
800nm		420	40	0.85
Dermis	-			
633nm		187.5	2.7	0.80
800nm		175	2.3	0.85
Combined with underlying tissue				
633nm	1.55*	70	3.1	0.80
Adipose Tissue	1.44			
1064nm		83	2.6	0.86
Blood (Hct = 0.41)	1.35			
Oxygenated				
665nm		1246	11.2	0.995
960nm		505	2.84	0.992
Deoxygenated				
665nm		509	4.87	0.995
960nm		668	1.68	0.992
Muscle	1.37			
515nm		530	11.2	
1064nm		215	2	0.96

** value refers to stratum corneum*

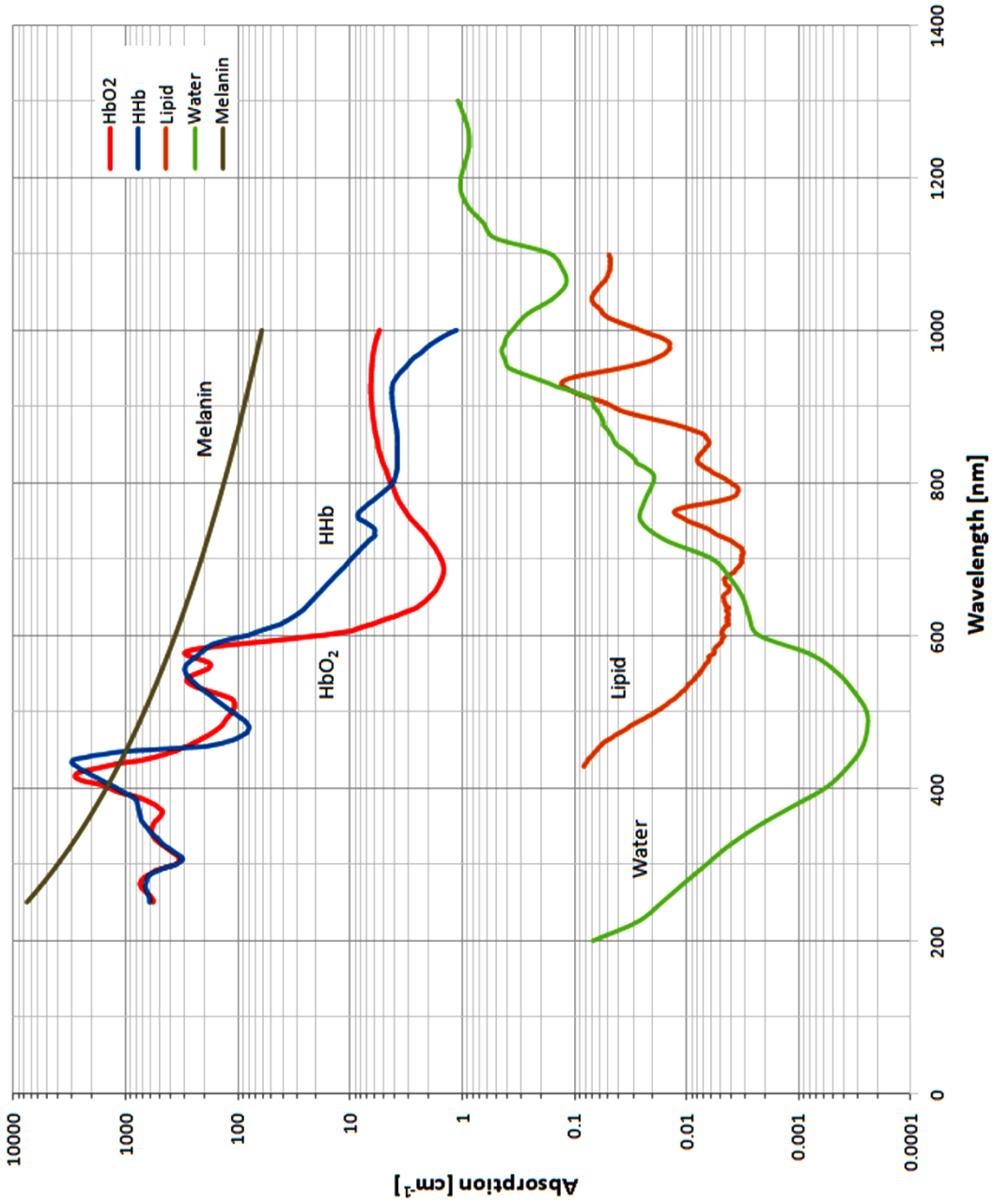

Figure 3-21 Absorption Spectra of the Five Main Chromophores Found in the Lower Leg

Chapter 4

System Design

This chapter describes design and testing of a near infrared spectroscopy system for lower leg tissue oxygenation monitoring. In particular, this chapter will describe clinical system requirements, proof-of-concept device design, and the updated NIRS system design. Additionally, in preparation for feasibility study, this chapter will present results of electronic circuit simulations, as well as system functional testing results.

Based on the clinical requirements, the NIRS system needed to be portable, light-weight non-invasive and designed to emit low level red and NIR light into human tissue and acquire, record, and display the reflected light from various tissue depths. The level of reflected red and NIR light varies, primarily, due to absorption by the chromophores of interest and the scattering coefficients of the tissues as described above. This system was designed to test the hypothesis that multi-channel depth-resolved near infrared spectroscopy can be used to monitor lower leg tissue oxygenation and lower leg oxygenation abnormalities.

The system requirements were based on a clinical need for a fully portable, compact multi-channel system capable of 36 hours standby time and 12 hours of continuous NIRS data acquisition time at 20 samples per second using a 700mAh rechargeable lithium-polymer battery. The sampling rate was based on the work by *Saager* [75], who found that 20 Hz offers more than sufficient sampling rate for characterizing hemodynamic fluctuations, which mostly occur in single- to sub-Hz range. Based on these requirements, the current consumption in the ready (i.e. standby) mode needed to be 19 mA and 58 mA in the active mode. In addition, the system

needed to display multi-channel real-time acquired data and save it to PC hard drive for off-line analysis.

Based on these clinical requirements, a proof-of-concept [POC] system was developed (Figure 4-1). The POC system consisted of: (1) An integrated data acquisition unit with four optical sources (i.e. LEDs) and four photo detectors [PDs] and (2) PC computer with software for data display and storage. Optical sources selected for the POC system were two red and two NIR LEDs. Using these four sources and four Si-PIN detectors, two red- and two NIR-specific detectors, it was possible to obtain eight channels of optical data from four different tissue depths. The POC system satisfied clinical requirement for a multi-channel data acquisition system. The remaining requirements, however, were not met by this early version of the NIRS system. Most importantly, the power consumption of the system was not achieved as intended. The reason for this was that each of the four photo detectors required individual analog circuitry and analog-to-digital channel. In addition, each of the sources were powered by their own LED driver circuitry. Finally, even though not a specific part of the clinical requirements, the total cost of the system was above the estimated commercially-viable value due to multiple PDs and numerous analog electronic components.

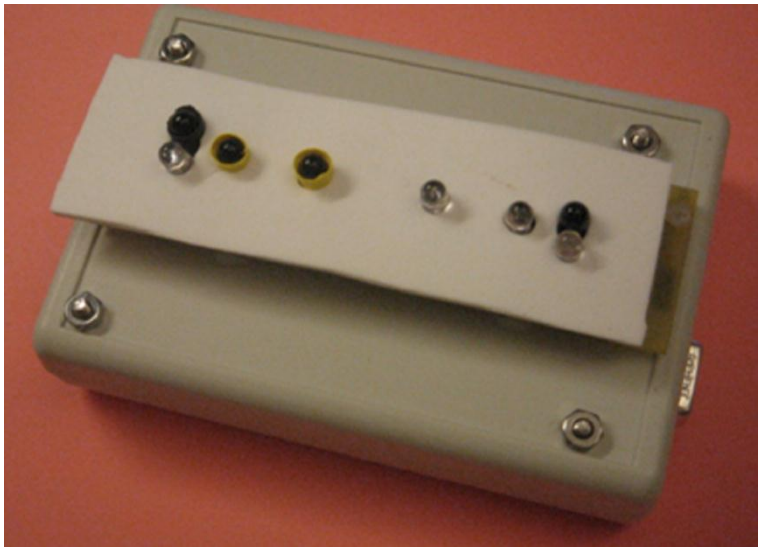

Figure 4-1 Proof-of-Concept System

Due to shortcomings of POC device, the current NIRS system was redesigned to include separate optical sensor module, data acquisition unit, and a PC computer, which is used for real-time data display, analysis, and storage (Figure 4-2). Designs of each of these sections are discussed next, as well as system functional testing and calibration results.

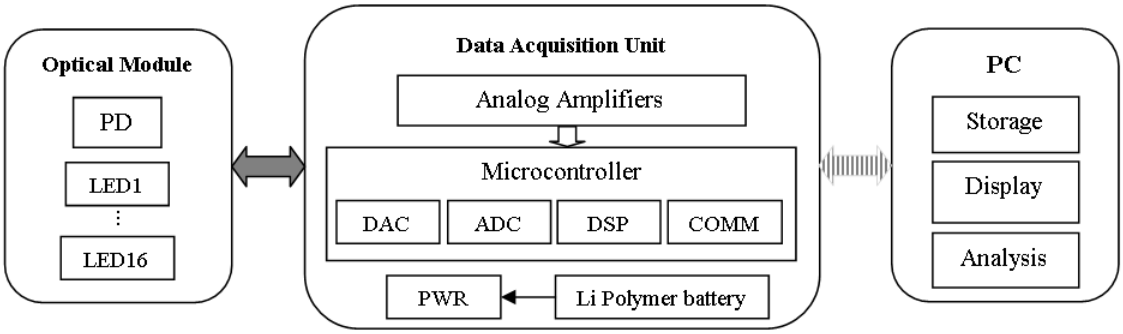

Figure 4-2 Block Diagram of the Complete NIRS System

4.1. Optical Module

Optical module consists of 16 light sources (expandable to 64) and a single photo detector, Si-PIN diode. The light sources and photo detector are discussed next, as well as the optical safety guidelines and Optical Module compliance with them.

4.1.1. Light Sources

Based on the absorption spectra of oxygenated [HbO_2] and deoxygenated [HHb] hemoglobin, Figure 3-21, the most suitable LED wavelengths will be in the range between 650nm- 700nm (minimal absorption of HbO_2) and 850nm – 930nm (minimal absorption of HHb). The reason for this is that at these intervals the difference between absorption of HbO_2 and HHb are the greatest. These intervals are also furthest away from HbO_2/HHb isosbestic point, which is located at approximately 805nm. Finally, Corlu *et al.* [6] determined that optimal wavelengths for detection of HbO_2/HHb are in the following ranges: 650 ±2 nm, 722 ±10 nm, 884 ±24 nm, and 930 ±2 nm. Based on the available off-the-shelf light sources within these ranges, LEDs at 650nm and 880 were selected as the NIRS system sources.

Light emitting diodes have similar electrical characteristics as other semiconductor diodes. Specifically, their current-voltage characteristic is described by an exponential function. Very small changes in LED voltage will result in exponential changes in LED current. In order to prevent excessive and potentially damaging LED currents, LEDs are normally powered by constant current sources. This means that the source sets the LED current to a fixed value while allowing voltage to follow as necessary. In addition to exponential current-voltage dependence, LED light color output is dependent on the value of the current flowing through it. For this

reason, the LEDs in the current NIRS system are driven by a constant-current source capable of delivering up to 600mA of current.

4.1.2. Photo Detector

The optical signal strength at the detector position on the surface of the skin was expected to be on the order of pico-watts [14], [75], depending on the actual radiant intensity of the light sources. Ideally, avalanche photodiodes [APDs] or photo multiplier tubes [PMTs] would be well suited as detectors. However, APDs and PMTs have several less-than optimal characteristics, the main one being high biasing voltage (from 30V up to more than 100V). This high biasing voltage is not well suited for portable systems. Therefore, the current NIRS will utilize silicone PIN [SiPIN] diodes. The PIN diodes have wide bandwidth, low capacitance, and low biasing voltage (if necessary). The optical sensitivity of SiPIN diodes is approximately two orders of magnitude smaller than that of APDs, however, it was determined that this reduced sensitivity does not present significant limitation to the current NIRS system.

4.1.3. Optical Safety

The Optical Module utilizes low power, non-ionizing red and infrared light emitting diodes [LEDs] as light sources. The NIR LEDs are classified as Infrared-A [IR-A] band light sources. Currently, there are no safety standards that exclusively deal with LEDs as light sources (such is the case with lasers). Prior to 2006, LEDs, as related to safety issues, were classified in the same category as lasers. Since 2006, however, LEDs are classified based on their application as LEDs used for data transmission (conforming to laser standard, IEC-60825) or, more commonly, lamp applications (lamp safety standard, IEC-62471) [76]. The Optical Module falls into the latter

category since the LEDs used in the system have epoxy shell that acts as an optical lens, filter, and a thermal barrier. Based on this classification, optical safety can be evaluated using the lamp application standard. The IEC-62471 standard addresses safety exposure limits for three tissue types: Cornea, skin, and retina. Under normal operating conditions, the cornea and retina will not be exposed to optical radiation from the current NIRS device. Therefore, the primary safety concern could be LED's thermal effect on the human skin. Based on the Statement from the International Commission on Non-Ionizing Radiation Protection [ICNIRP] on Light-Emitting Diodes and Laser Diodes Implications for Hazard Assessment, thermal injury of the skin requires sources with optical powers in the hundreds of miliwatts to watts ranges [77]. Light sources utilized in the Optical Module have optical (i.e. radiant) power levels of less than five (5) milliwatts, which is typical output power of a red laser pointer, class IIIA. These levels are well below the hazardous thermal injury levels as specified in [77]. Therefore, the current NIRS system presents no significant risk of thermal injury to subjects. Figure 4-3 shows the Optical Module with dimensions and source-detector configuration.

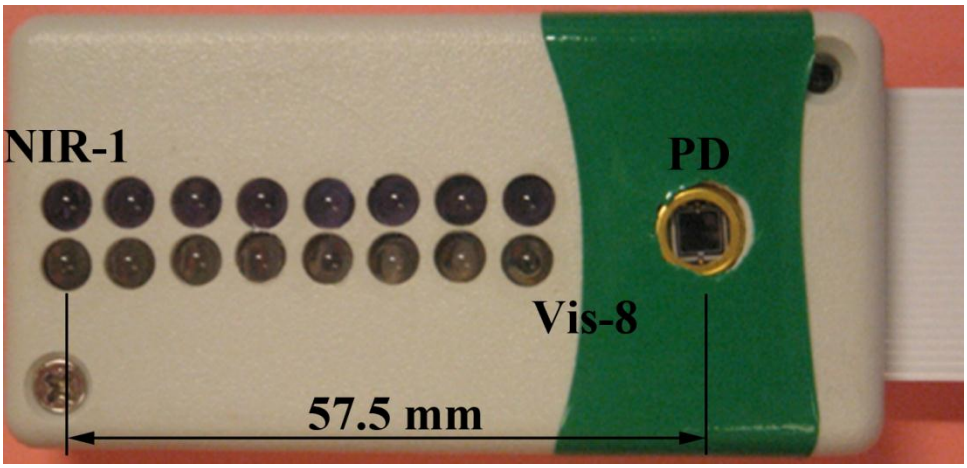

Figure 4-3 Optical Module

4.2. Data Acquisition Unit

Data acquisition unit consists of analog circuitry, analog-to-digital conversion section, and digital circuitry. The analog circuitry section is responsible for linear conversion of detected light levels (i.e. photo current) into voltage signal and its processing. Analog-to-digital section digitizes analog voltage into digital values, which are then further processed by digital circuitry and sent to PC for display and storage.

4.2.1. Analog Circuitry

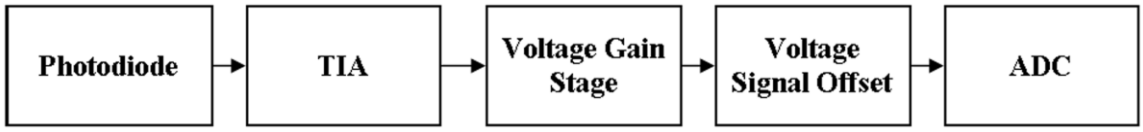

Figure 4-4 Block Diagram of the Complete Analog Signal Path

4.2.1.1. Transimpedance Amplifier [TIA]

Transimpedance amplifiers [TIA] are active electronic circuit elements used to convert current signals into corresponding voltage signals. The current sources are usually present in electric circuits that contain semi conductive photo detectors, such as photodiodes [PD]. These elements generate very small currents when exposed to light of specific wavelength. Currents from photodiodes, however, are not suitable for direct digitization. Consequently, they need to be either amplified and then sampled using current analog-to-digital converter [ADC], or they need to be converted to a corresponding voltage signal and then sampled using traditional voltage ADC. Given the fact that TIA converts current to voltage, the gain of TIA is represented by

resistance (i.e. impedance), hence the name transimpedance. The gain of a TIA has units of ohms (Ω) and is found using the following equation:

$$K = R_f = \frac{v_{out}}{i_{in}} \tag{4-1}$$

where V_{out} is voltage at TIA output and i_{in} is current at TIA inputs

From equation (4-1), the output voltage is calculated as a function of photodiode current and feedback resistor, R_f (Figure 4-5):

$$v_{out} = i_{in} R_f \tag{4-2}$$

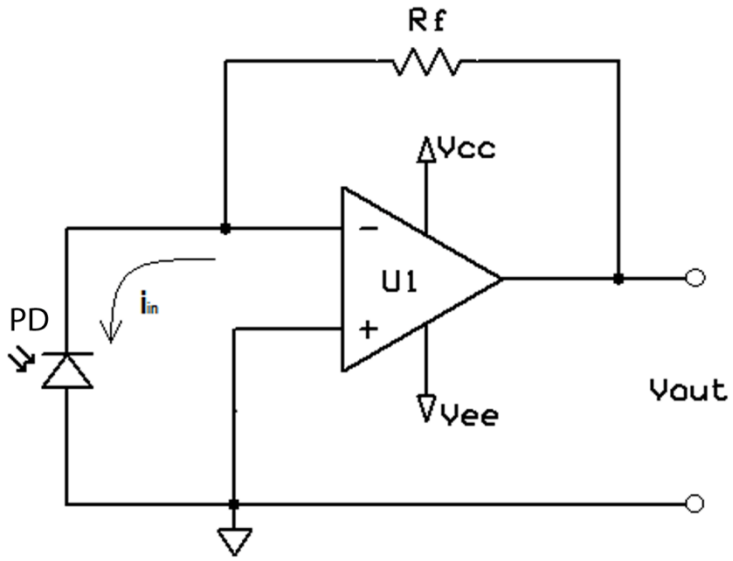

Figure 4-5 A Basic Transimpedance Amplifier Circuit

The circuit of Figure 4-5 provides a linear conversion of photodiode current to voltage. Since photodiode currents are very small, in practice a very large R_f resistor is used to obtain practical voltage levels at the output. In addition, a large feedback resistance improves (i.e. reduces)

voltage noise at the output of the op-amp. This is explained by Johnson or thermal noise. Johnson noise originates in resistive elements of electronic circuits. Specifically, Johnson noise is caused by thermal motion of charged particles. This type of noise is considered to be a "white noise," which has noise spectral density that is constant with frequency. The following equations are derived for calculating the power, voltage, and current values for Johnson noise:

$$P_J(rms) = kT\Delta f \tag{4-3}$$

where k is Boltzmann's constant (1.38×10^{-23} J/K), T is temperature in °K, and Δf is an effective noise bandwidth in Hz

$$V_J(rms) = \sqrt{4kTR_f\Delta f} \tag{4-4}$$

where R_f is resistance of circuit element in ohms (Ω)

$$i_J(rms) = \sqrt{\frac{4kT\Delta f}{R_f}} \tag{4-5}$$

Equation (4-4) shows that voltage noise at the output is proportional to the square-root of the feedback resistance, R_f, while the output signal voltage is directly proportional to it (equation (4-2). Therefore, the signal-to-noise ratio (SNR) at the output is improved by a factor of square-root of R_f ($\sqrt{R_f}$) by using large feedback resistance.

Single-ended high-value feedback resistance (Figure 4-5), however, causes this circuit to be highly susceptible to coupling noise from electrostatic, magnetic, and radio frequency sources. The simplest way to reduce coupling noise from external sources is to utilize both

inputs of the operation amplifier (op-amp) and its common-mode rejection (CMR) characteristic. To accomplish this, a second resistor, R_2, is added between the positive input of the op-amp U1, photodiode anode and system ground as shown in Figure 4-6.

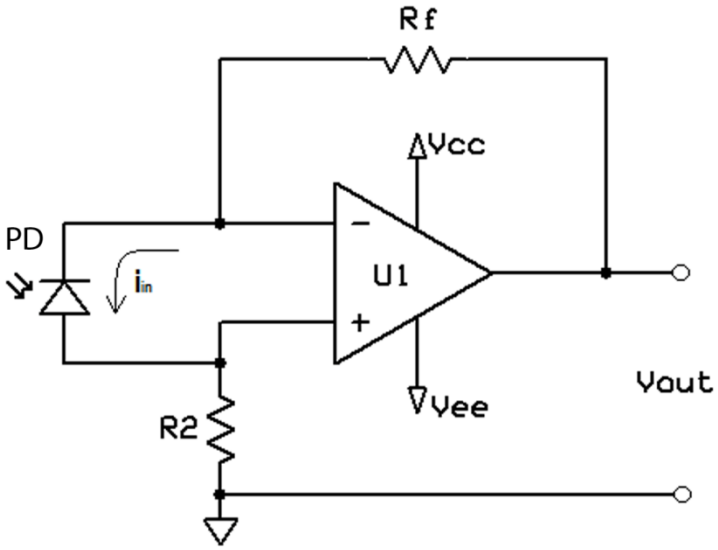

Figure 4-6 Transimpedance Amplifier Circuit with Improved Noise Characteristics

The addition of R_2 into the circuit causes photodiode current to drive the positive input of the op-amp. This effectively causes DC voltage as well as the leakage current from the photodiode to also be zero, since the voltage between positive and negative inputs of the op-amp is essentially zero. Transimpedance amplifier circuit of Figure 4-6 will perfrom well with respect to sensitivity, linearity, and interference noise suppression.

This circuit, however, may exhibit oscillations and gain peaking at its output. The oscillations are a direct result of the op-amp feedback configuration while gain peaking is a phenomena that occurs due to high input capacitance at the feedback op-amp terminals. Gain peaking is usually present at high frequencies. A solution that may address both of these

unwanted circuit disturbances features a small-value feedback capacitor, C_f, connected in parallel with the feedback resistor, R_f (Figure 4-7). Additional benefit of this capacitance is its ability to limit the output signal bandwidth, which consequently reduces introduction of unwanted noise into the system.

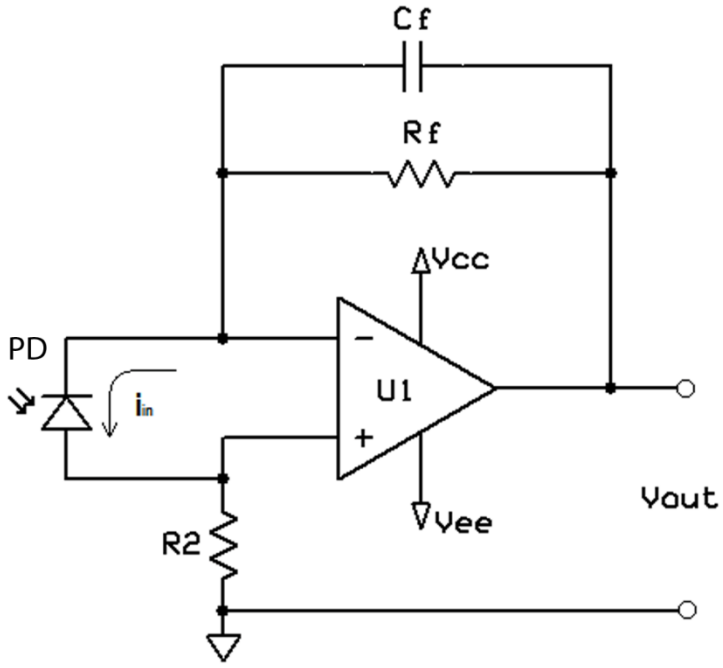

Figure 4-7 Transimpedance Amplifier Circuit with Improved Noise Characteristics and Stability

Due to improved noise and stability, as well as bandwidth limiting capability, the transimpedance amplifier circuit of (Figure 4-7) was utilized in the current NIRS system. Component values for TIA circuit were selected as follows:

$R_f = 1M\Omega$ $C_f = 3.9pF$ $R_2 = 1M\Omega$

Based on these values, TIA gain was calculated using equation (4-1) as follows:

$$K = \frac{v_{out}}{i_{in}}$$

$$K = \frac{i_{in}(R_f + R_2)}{i_{in}} = 2M\Omega \quad (4\text{-}6)$$

The value found in equation (4-6) actually represents the TIA responsivity in volts per watt (V/W). Additionally, bandwidth of this TIA circuit is limited by the parallel connection of the feedback capacitor and feedback resistor as follows:

$$f_{V_{out}} = \frac{1}{2\pi R_f C_f} = \frac{1}{2\pi(1x10^{6})(3.9x10^{-12})} = 40.808x10^{3}Hz \quad (4\text{-}7)$$

where $R_f C_f = 1/\omega_c$

4.2.1.2. Voltage Amplification and Gain

Based on system block diagram of Figure 4-4, the voltage signal is further amplified and offset. This additional voltage amplification and offset are needed in order to utilize full ADC range. The total voltage gain in Stages 1 and 2 was set to 9.25, while offset was set to ADC's mid-range value at 1.25V. After the analog signal is amplified and offset, it is passed to ADC for digitization.

4.2.1.3. Analog System Parameter Characterization Using SPICE

This section presents results of simulation program with integrated circuit emphasis [SPICE] calculations of the analog system gain and frequency response. The simulations were performed using the LTspice®, freely-available simulation software developed by Linear Technology Corporation.

The photodiode element was modeled using a pulsed current source with 1nA amplitude, 10μs rise and fall times, 1.25ms pulse duration, and 7.5ms period (see Figure 4-12 for ADC

timing example). Transimpedance amplifier and gain stages were simulated using the LT1126 dual operation amplifier, while the offset circuitry was realized using the LTC2054 operational amplifier. Both operational amplifiers are made by Linear Technology Corporation (Milpitas, California, USA). Waveform in Figure 4-8 shows the output of the TIA circuit with proper signal shape and transimpedance gain amplitude of 2mV. Figure 4-9 displays TIA circuit frequency response (i.e. magnitude and phase) plot. As mentioned above, the signal gain of the second stage was set to 9.5. The value of second stage gain is verified by superimposing the Gain Stage output waveform over the TIA output (Figure 4-10). Finally, the output of the complete analog signal chain is shown in Figure 4-11. The waveform at the final analog signal chain output is buffered, inverted, and offset by 1.25V. Again, the pulse shape waveform of the original source signal is preserved. This verifies that the analog chain bandwidth is sufficiently large to handle fast rise and fall times of the expected pulsed source signal.

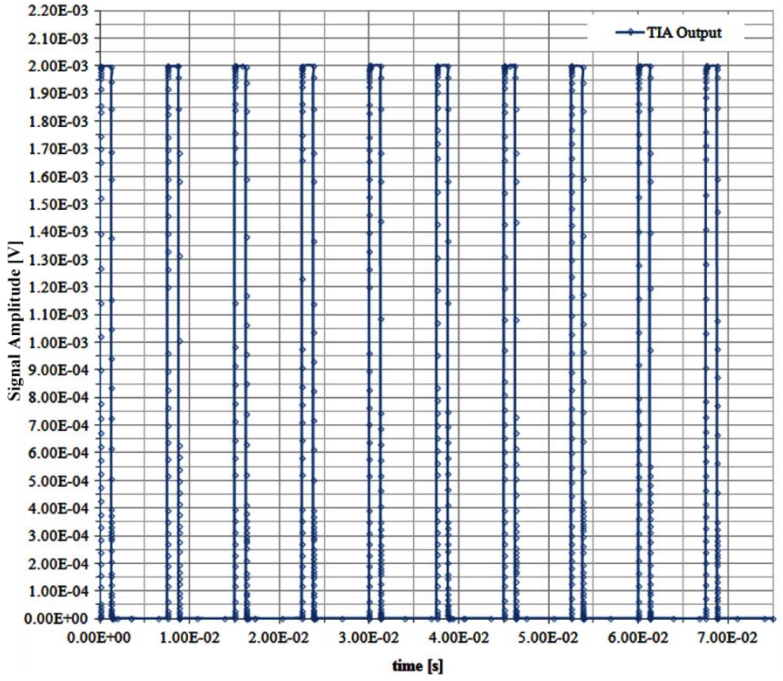

Figure 4-8 TIA Output Waveform from SPICE

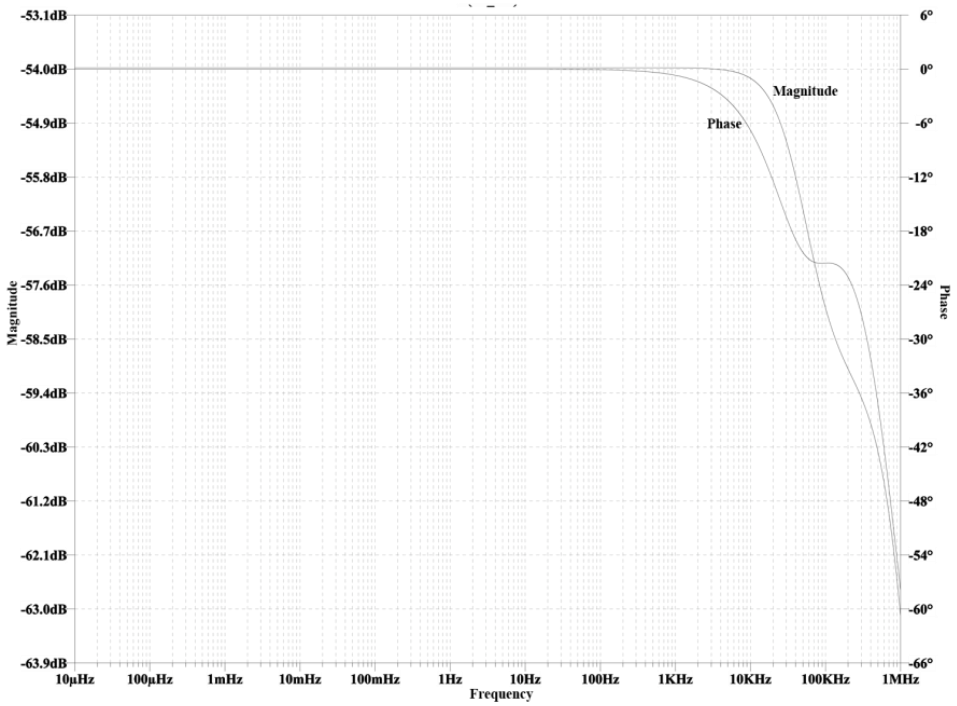

Figure 4-9 TIA Magnitude and Phase Waveforms from SPICE

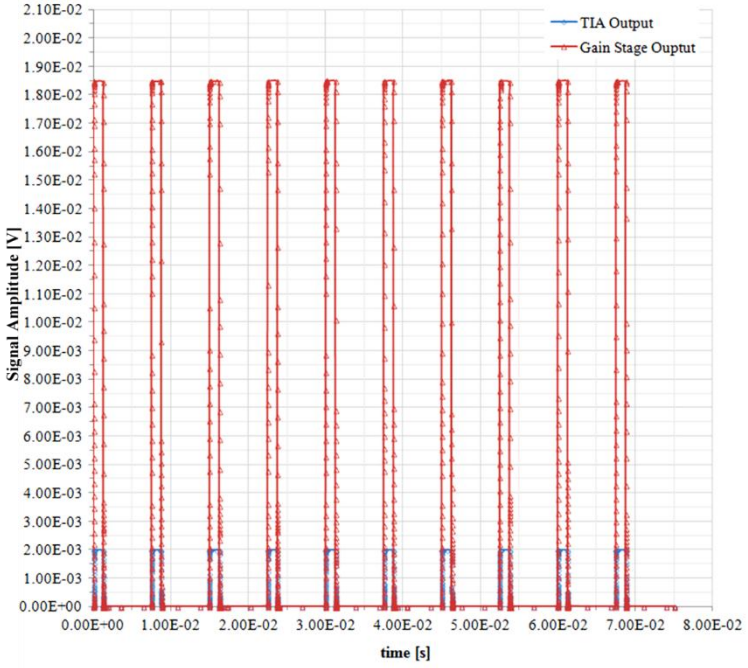

Figure 4-10 TIA and Gain Stage Output Waveforms from SPICE

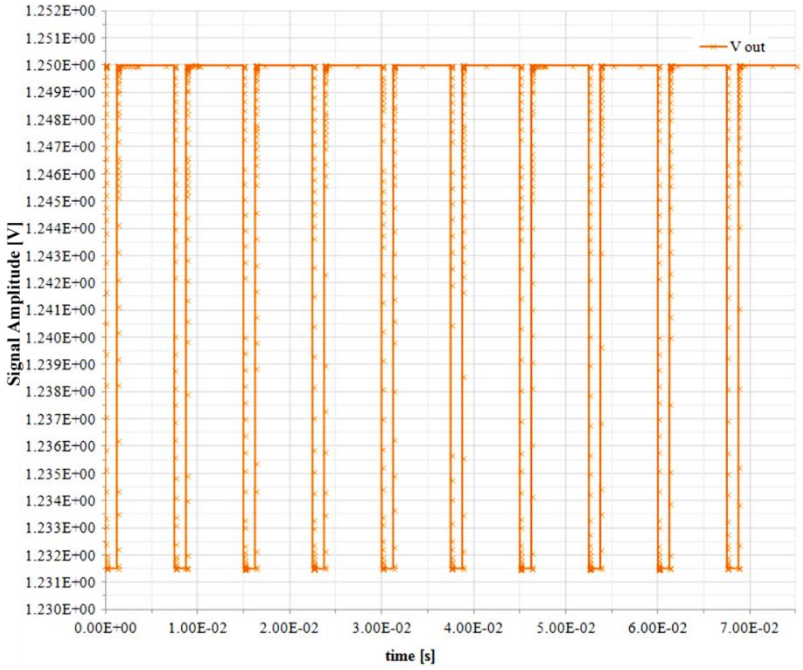

Figure 4-11 Analog Signal Chain Output Voltage Waveform from SPICE

4.2.2. Digital Circuitry

At the heart of the NIRS system is an ultra-low power microcontroller, MSP430-family by Texas Instruments (Dallas, Texas, USA). The MSP430 family was selected because of its ultra-low power requirements and processing capabilities. Based on project requirements and microcontroller capabilities, the MSP430FG4618 device features a powerful 16-bit RISC CPU, 16-bit registers, and constant generators that attribute to maximum code efficiency. The digitally controlled oscillator (DCO) allows wake-up from low-power modes to active mode in less than 6µs. In addition, the MSP430FG461x series has configurations with two 16-bit timers, a high performance 12-bit 12 channel A/D converter, dual 12-bit D/A converters, three configurable operational amplifiers, one universal serial communication interface (USCI), one universal synchronous/asynchronous communication interface (USART), and direct memory access

(DMA). Digitized data is sent to the PC in binary format using the serial communication protocol. Serial communication protocol (i.e. serial port profile, SPP) is one of the most common protocols used for Bluetooth® wireless interface.

As mentioned above, the MSP430FG461x series utilizes a 12-bit 12-channel successive approximation [SAR] analog-to-digital converter. The NIRS system was designed to utilize this ADC due to its very low power consumption, as well as its resolution. Furthermore, in order to reduce the number of components, the NIRS system uses MSP430's internally-provided 2.5V voltage reference during data conversion. This voltage reference also defines ADC's full-scale voltage digitization range. Using this range and ADC resolution, the least significant bit [LSB] was calculated as follows:

$$LSB = \frac{voltage\ range}{2^{resolution\ bits}} = \frac{2.5V}{2^{12}} = \frac{2.5V}{4096} = 610x10^{-6}V \qquad (4\text{-}8)$$

The value from equation (4-8) represents the minimal voltage or voltage change that may be detected using the MSP430FG461x internal ADC. Based on the expected NIRS signal level changes, this LSB value provides sufficient resolution for the current system.

The analog-to-digital conversion is controlled by the microcontroller's embedded software, which also controls the sequencing of LEDs. Figure 4-12 shows a sample of timing sequence relationship between ADC and four LED sources. After LED1 has been turned on and its light output stabilized for a period of approximately 625μs, the ADC reads in and digitizes the voltage value from the photodiode ("ON" state). Next, LED2 is turned on and allowed to stabilize. Again, after approximately 625μs, ADC reads in and digitizes the voltage value from the photodiode. This sequence is repeated for all LED sources, respectively. This sequence

minimizes ADC power consumption and it also provides stable light output from each light source.

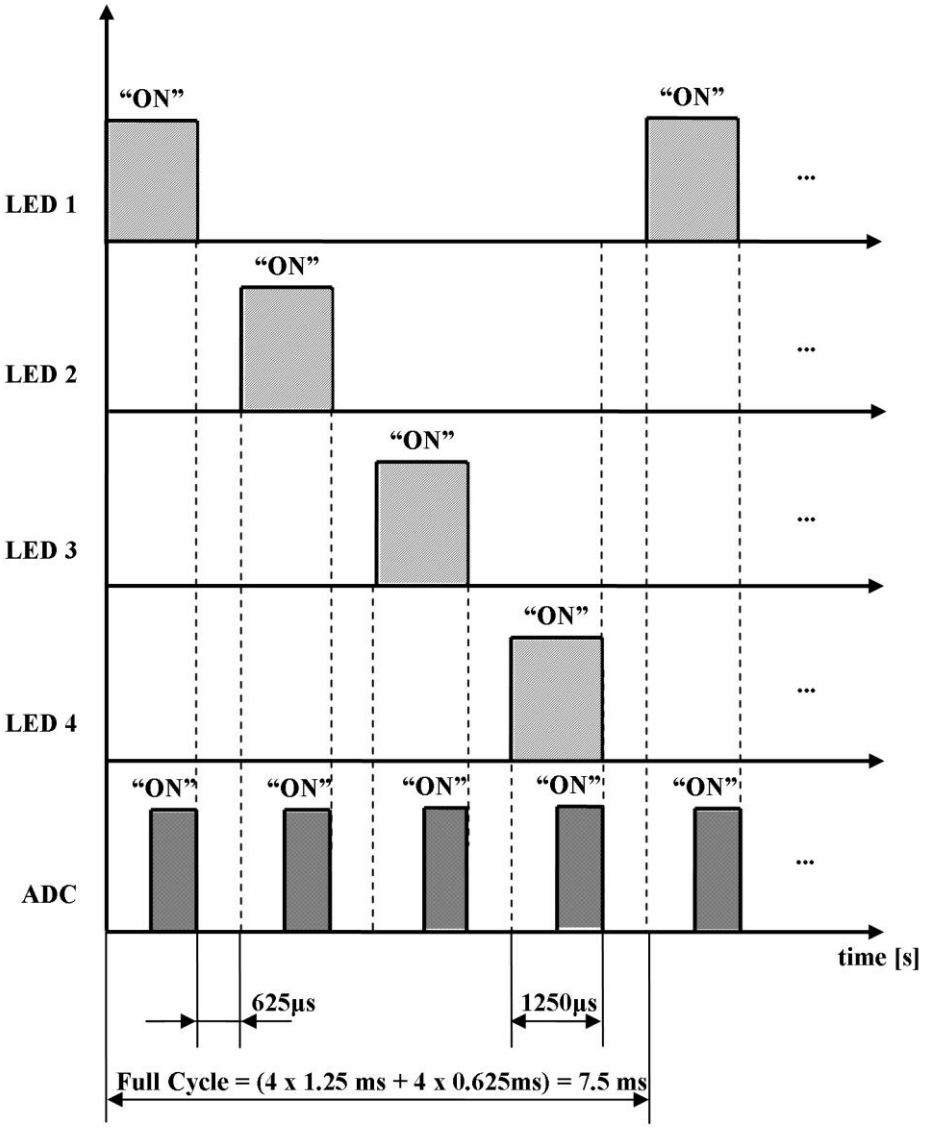

Figure 4-12 Example of ADC and LED Timing Sequence for Four Sources

4.2.3. Power Supply Circuitry

The power supply module provides necessary regulated DC voltages for various electrical and optical components in NIRS system. In general, the power supply is divided into analog and digital (including optical) sections. The reason for separating power supplies is the noise. Digital (i.e. switching) components tend to introduce larger noise in the system than analog components. Since the NIRS device is acquiring very low level optical (i.e. analog) signals, it was imperative that the analog power supply and analog ground plane remain separate from the noisier digital components.

The power source for the portable signal acquisition unit comes from the secondary (i.e. rechargeable) lithium-polymer battery. This type of battery has a very high charge-storage density that yields smaller and lighter battery pack. The nominal voltage of a single-cell lithium battery is 3.6V. The NIRS system, however, uses two lithium-polymer cells connected in series to obtain 7.2V nominal voltage. This voltage level was required in order to minimize number of components in the power supply circuitry, as well as to increase system power efficiency. Due to the chemical nature of lithium-polymer batteries, each battery pack is equipped with the manufacturer-recommended protection circuit, which protects the battery cells from over-charge and under-discharge conditions.

4.2.4. Electrical Safety

The current NIRS system utilizes Optical Module (i.e. sensor strip), which contains LEDs and a PD. The sensor strip consists of four layers (Figure 4-13): (1) Insulating film (e.g., acrylic paint); (2) Copper layer which provides electrical connections between the electro-optical components (i.e. LEDs and a PD) and the Device; (3) Polyimide film (e.g., Kapton®) or FR-4,

which provide a substrate for copper layer; and (4) Insulating film (e.g., acrylic paint, ABS plastic). During operation, the sensor strip is placed in direct contact with the subject's skin. Based on the strip design, however, there is no direct electrical connection between the subject's skin and NIRS system.

The current NIRS system utilizes two rechargeable Li-polymer 3.7 V cells with 700 mAh capacity, connected in series. This yields nominal 7.3 V, 700 mAh battery pack with battery manufacturer's recommended safety circuit. This safety circuit protects the battery from accidental short circuit and overcharging as well as over discharging conditions. The battery cells are UL listed and UN approved as non-dangerous goods regulated [NDGR].

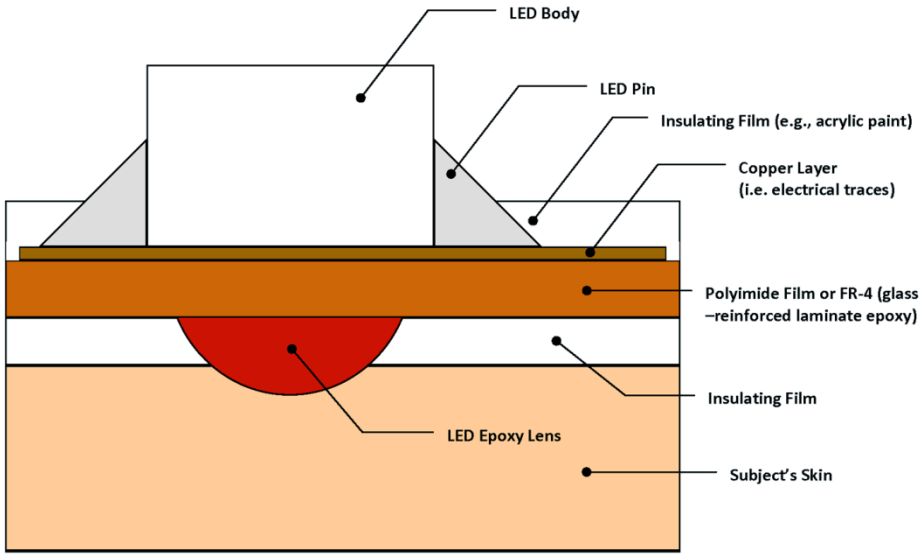

Figure 4-13 Optical Module LED Mounting Detail (not-to-scale)

Figure 4-14 shows the data acquisition unit and optical module of the current NIRS system.

Figure 4-14 Current NIRS System (Data Acquisition Unit, left, with Optical Module)

4.3. PC Software

The PC software for the current NIRS system data display and storage utilizes custom-designed application developed with Microsoft® DirectX® technology. The application is capable of displaying up to 64 channels of data with various user-configurable parameters such as display scale, signal grouping, and displayed data color. Furthermore, the application has the capability to implement various signal processing algorithms depending on the NIRS system application.

4.4. Functional System Testing Results

Four bench-top tests were conducted to evaluate initial performance of the current NIRS system. First, the system current was measured using the ampere meter in the Agilent E3631A triple power supply. The voltage was set to 7.6V DC, and the current was measured in "ready" mode and then in "active mode. In ready mode, system is set to acquire data with the optical module

disabled. In active mode, the system is acquiring and sending NIRS data to PC for display and storage. The design goal for the ready mode current was set to 19mA and was measured to be 16.5mA, which is approximately 15 percent improvement over the design goal. Active mode current goal was set to 58mA but was measured to be 60.3mA. Second, in order to be able to monitor certain physiologic parameters, the system needed to be able to sample acquired optical signals at 20 samples per second [sps]. We used Agilent 33120A arbitrary function generator, Agilent DSO1024A oscilloscope, and PC application to test the accuracy of our analog-to-digital conversion, as well as to verify our maximum data sampling rate. The current version of the system is able to acquire NIRS data at a rate of 50sps. Third, total system weight was measured to be 95 grams, which was five grams below design goal. Finally, the last major design goal was achieved by successfully displaying 64 channels of data in real-time. The summary of NIRS system functional testing results is shown in Table 4-1. The system succeeded in accomplishing four of the five main goals. The one parameter that required further optimization was the active mode current consumption, which exceeded design goal by four percent. This goal was achieved by making improvements to the embedded control software and by reducing device sampling rate.

Table 4-1 Functional Testing Design Success Metrics for the NIRS System

Parameter	Design Goal	Testing Results	Goal Achieved
Current Consumption [mA]			
Ready Mode	19	16.5	Yes
Active Mode	58	60.3	No
Sampling Rate per Channel [sps]	20	50	Yes
Total Weight [g]	100	95	Yes
Real-time Multi-channel Data Display	64	64	Yes

4.5. Device Calibration

In addition to four bench-top tests, which were conducted to evaluate initial performance of the current NIRS system, the analog amplification chain noise measurements were also conducted on three current NIRS systems. The noise levels were measured with optical module disabled, which allowed for the noise testing of analog circuitry only. The results of these tests are presented in Table 4-2.

The noise level measurements of the analog amplification chain show that the noise mean ranges from 2.091 LSBs for Device 001 to 78.610 LSBs for Device 003. Based on LSB value from equation (4-8), the noise mean ranges from 1.276mV to 47.952mV, respectively. The largest mean noise value, measured in Device 003, represents approximately two percent of the total ADC range. The corresponding probability density functions [PDFs] of analog amplification chain noise levels are shown in Figure 4-15.

Table 4-2 Analog Circuitry Noise Levels for Three NIRS Systems without Calibration

Device	***001***	***002***	***003***
Mean [LSB]	2.091	31.155	78.610
Standard Deviation	2.792	4.132	4.245
Variance	7.796	17.078	18.025
Maximum Value	16.00	46.063	93.938
% of ADC Range	0.39	1.12	2.29
Minimum Value	0.000	16.750	63.438
% of ADC Range	0.00	0.41	1.55
Total Samples	3023	3020	3020

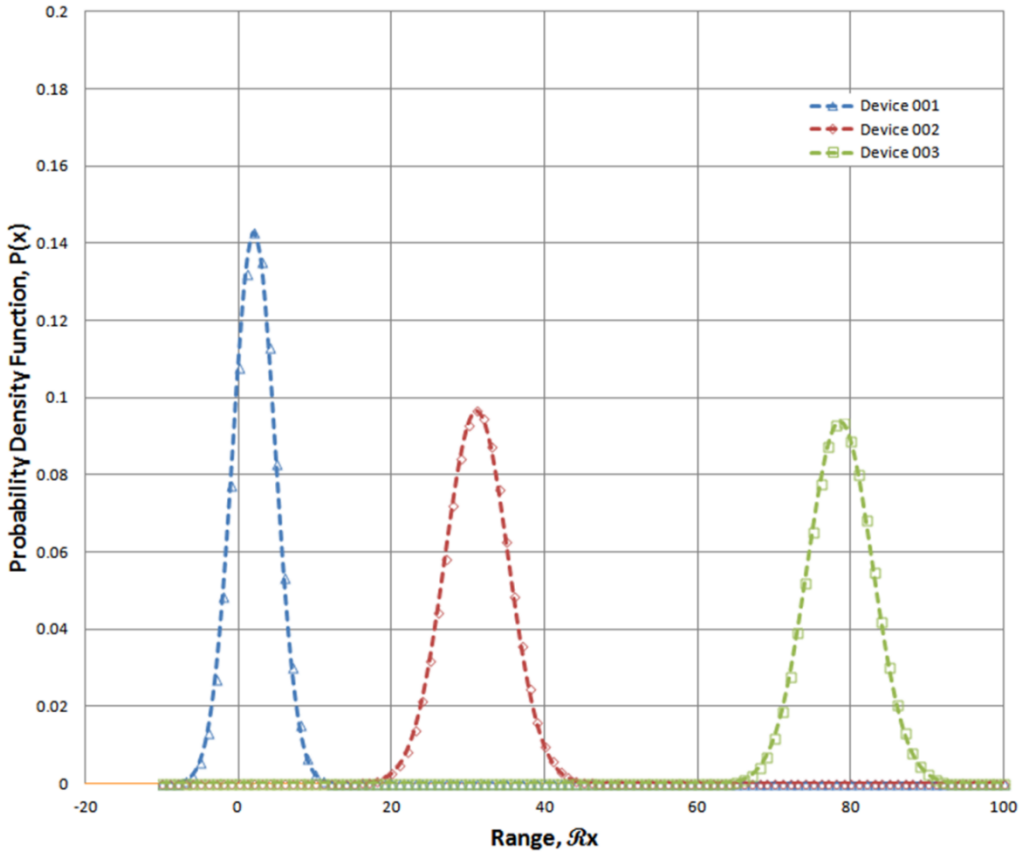

Figure 4-15 Probability Density Function of Analog Amplification Chain Noise Levels Before Calibration

The PDF plots of Figure 4-15 indicated that the inter-device variability with respect to analog noise levels warranted improvement. One of the ways to improve noise level performance between devices was to implement calibration on per-device basis. The calibration coefficients were calculated based on each device's noise level data and were hard coded into the microcontroller of each device. This procedure allowed us to customize noise compensation to each device's analog circuitry variations (Table 4-3). The PDFs of three devices with calibration coefficients are shown in Figure 4-16, while Figure 4-17 summarizes PDFs of both pre- and post-calibration results.

Table 4-3 Analog Circuitry Noise Levels for Three NIRS Systems with Calibration

Device	***001***	***002***	***003***
Mean [LSB]	1.190	2.335	2.961
Standard Deviation	2.126	2.847	3.188
Variance	4.523	8.107	10.165
Maximum Value	13.813	16.063	17.625
% of ADC Range	0.34	0.39	0.43
Minimum Value	0.000	0.000	0.000
% of ADC Range	0.00	0.00	0.00
Total Samples	3022	3024	3020

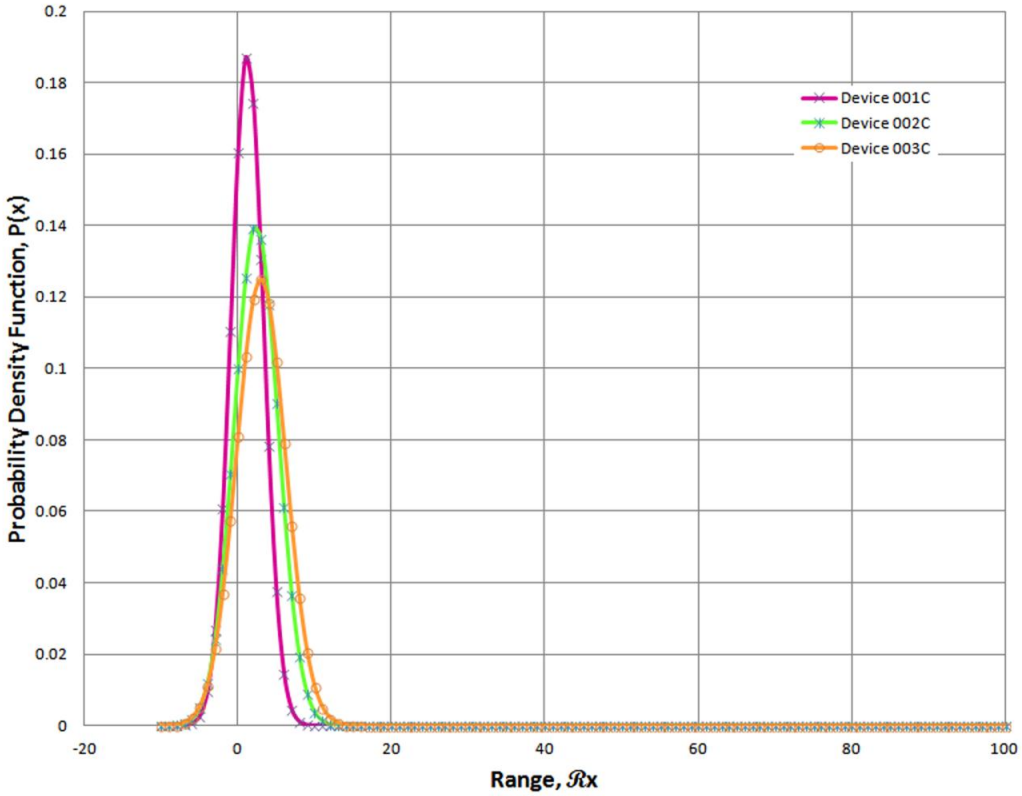

Figure 4-16 Probability Density Function of Analog Amplification Chain Noise Levels After Calibration

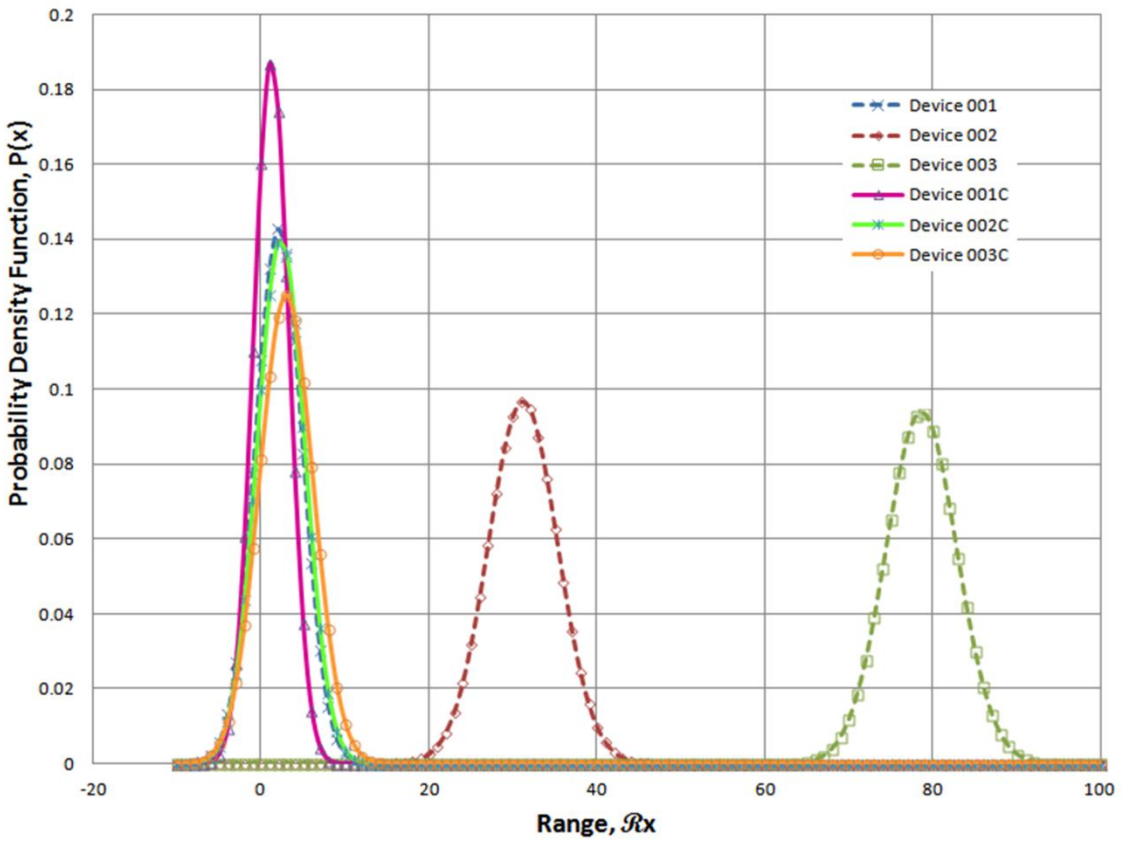

Figure 4-17 Probability Density Function of Analog Amplification Chain Noise Levels Before and After Calibration

4.6. Summary

This chapter described clinical system requirements, proof-of-concept device design, and the updated NIRS system design and development. The system design was based on a clinical need for a fully portable, compact multi-channel system capable of 36 hours standby time and 12 hours of continuous NIRS data acquisition time at 20 samples per second using a 700mAh rechargeable lithium-polymer battery. In order to facilitate longer battery lifetime and safe device handling, low level red and NIR light emitting diodes were used to shine corresponding

light into human tissue. We set out to accomplish five functional goals for the novel system: Current consumption of 58mA in active mode, sampling rate of 20sps, total system weight of 100g, and real-time multi-channel data display. Initially, the novel system accomplished four of the five goals we set out. The single missed goal, however, was achieved by optimizing our embedded control software to minimize active current consumption.

After conducting functional tests, the analog signal amplification chain was characterized with respect to amplification and noise levels. Due to variability in electronic components, a calibration procedure was instituted to reduce inter-device analog signal noise level variability. Calibration coefficients were derived individually for each device and loaded respectively. Implementation of calibration coefficients reduced analog signal noise levels from 2.29 percent to 0.43 percent for the worst-case device. The design and testing results of the novel NIRS system confirm device's readiness for clinical testing. Device feasibility study design, procedure, and expected outcomes are outlined in the next chapter.

Chapter 5

Clinical Testing

5.1. Introduction

The purpose of this feasibility study was to evaluate the performance of a novel NIRS system in detection of oxygenated and deoxygenated hemoglobin changes at various tissue depth levels during venous occlusion in the lower leg. Our hypothesis states that multi-channel depth-resolved near infrared spectroscopy can be used to monitor lower leg tissue oxygenation and lower leg oxygenation abnormalities and that depth-resolved data collection will provide useful information for analyzing the oxygenation state of tissue. The venous occlusion enables the pooling of venous outflow in the lower leg (i.e. below the knee) compartments while still allowing arterial inflow. This scenario simulates several abnormal perfusion conditions in the lower leg, one of them being the acute compartment syndrome (ACS). As mentioned in Chapter 2, compartment syndrome is a condition in which increased pressure within the limited space (i.e. compartment) endangers vascular circulation and regular function of local tissue within that space [21], [29]. The compartment syndrome is the most important and the second most frequent complication encountered in the course of lower leg trauma treatment [22], [78]. The initial diagnosis of the compartment syndrome is, most often, based on the clinical presentation of excruciating pain (i.e. out-of-proportion pain), pain on the passive stretch of the muscles of the affected compartment, partial loss of sensory stimuli, and tension of the compartment boundaries

[29]. However, it is important to note that the severe pain presentation may not be as sufficient in young patients (i.e. children) or may not be present in unconscious patients [79]. As a result of missed or absent symptoms, the patient's health condition can quickly deteriorate so speedy diagnosis and aggressive treatment are needed in order to avoid the loss of a limb. Currently, the most widely used method for diagnosis of compartment syndrome is based on invasive measurement of the intra-compartmental pressure (ICP) using a needle and arterial line transducer [80].

5.2. Study Overview

This feasibility study was designed as a cross-sectional single arm study (Figure 5-1). The study attempted to accomplish two main objectives: The first objective was to perform initial evaluation of novel device's signal acquisition performance from lower leg in healthy human subjects during venous occlusion, while the second objective was to evaluate device's design with respect to inter-optode distance, as well as optode geometrical configuration. This feasibility study was reviewed and approved by the University of California, Los Angeles Institutional Review Board [IRB].

The study population consisted of healthy volunteers, age 18 to 30, with each subject acting as their own control. This population was selected because of minimized risk for the development of serious complications during the study procedure. Table 5-1 shows the summary of the subject inclusion and exclusion criteria.

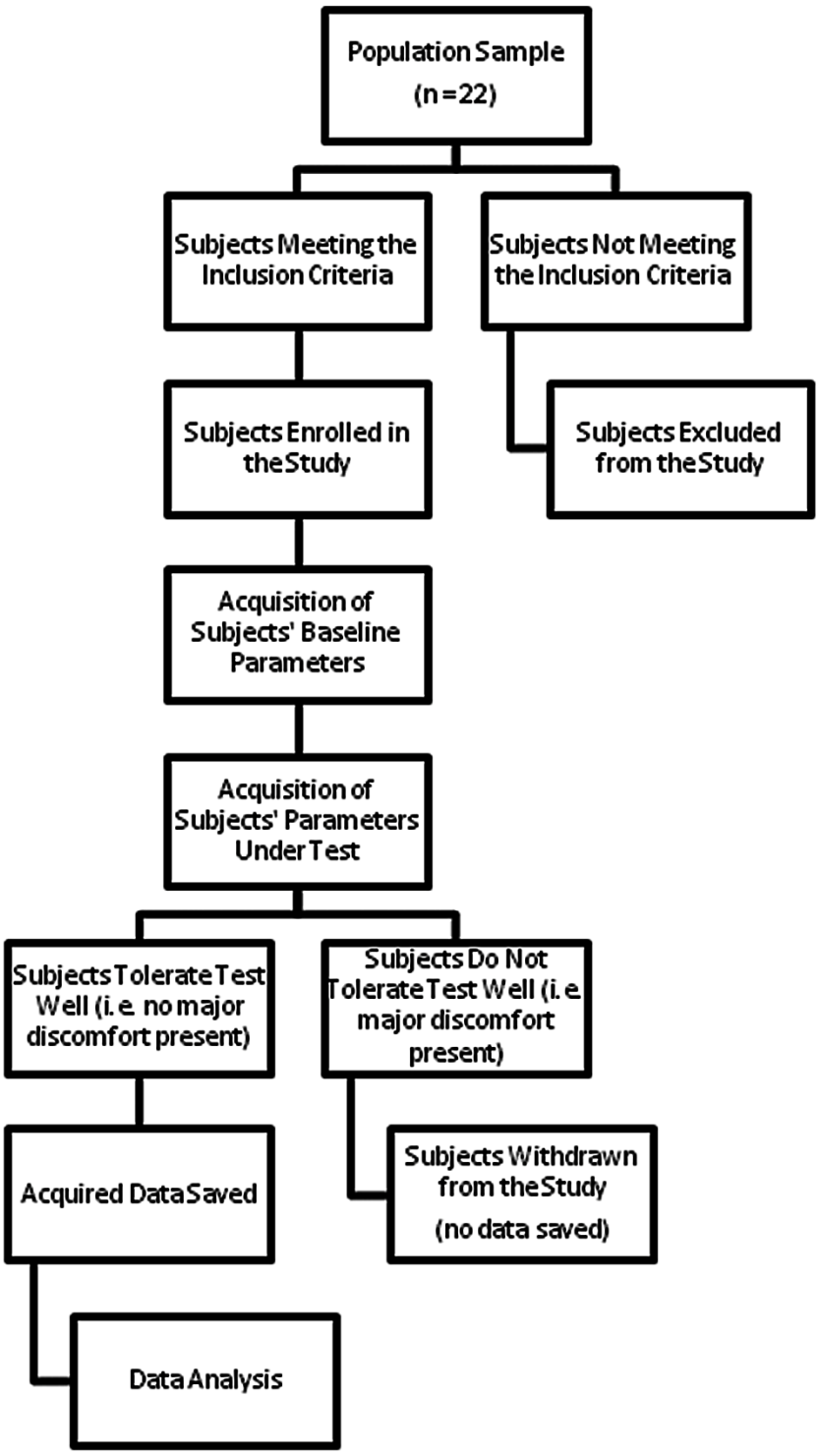

Figure 5-1 Study Design Outline

Table 5-1 Subject Inclusion and Exclusion Criteria for Study Enrollment

Inclusion Criteria	***Exclusion Criteria***
18-30 years old;	History of cardiac abnormalities;
No current or previous extremity injury;	History of peripheral vascular disease;
Able to lie still in supine position for up to one (1) hour;	History of pulmonary disease;
Able and willing to provide written informed consent in English language.	Smoking;
	History of diabetes, Type I and II;
	Pregnancy;
	Current use of contraceptives;
	Current abnormal blood pressure values (systole $\geq$ 140 mmHg, diastole $\geq$ 90 mmHg) as recorded in Health History Questionnaire.

Based on previous studies by Shuler *et al* [50], [81], which are similar to the current study, the following statistical parameters and calculations have been utilized to calculate the sample size (i.e. total number of legs). It is important to mention that each subject will serve as both control and test (i.e. one leg will be used as a control while the other as a test).

$\alpha = 0.05$ ($p < 0.05$)	CI = 0.95
$\beta = 0.1$	$\sigma = 0.08$ (7.7%) [50]
Power = $1 - \beta = 0.9$	$Z_{critical} = 1.96$ [82]
D = 0.1 (10%) [81]	$Z_{Power} = 1.28$ [82]

N = ?

where,

α	significance criterion (probability of type I error)	CI	confidence interval
β	probability of type II error	σ	standard deviation
D	minimum expected difference between two means	$Z_{critical}$	standard normal deviate for desired significance criterion
N	sample size (number of control and test legs) [82]	Z_{Power}	standard normal deviate for desired statistical power

$$N = \frac{4\sigma^2(\mathrm{Z}_{\mathrm{critical}} + \mathrm{Z}_{\mathrm{Power}})^2}{D^2} \tag{5-1}$$

$$N = \frac{4(0.08)^2(1.96 + 1.28)^2}{0.1^2} \tag{5-2}$$

$$N = \frac{0.0256(10.4976)}{0.01} = 26.874 \tag{5-3}$$

Using the result of equation (5-3), the minimum statistical sample size of 28 (i.e. 14 subjects) was required for the current study. We recruited a total of 22 subjects.

5.3. Study Procedure

Prior to obtaining any health information or collecting physiological data, an informed written consent was executed for each subject. After obtaining the subject's consent, a blood pressure reading was taken and recorded in Health History Questionnaire to verify normal levels.

The NIRS system is a non-invasive investigational device designed to emit and acquire low power red and near infrared light from various depths of human tissue. The device utilizes light sources and detectors similar to the ones found in clinical and over-the-counter (OTC) pulse oximeters. At the beginning of the study procedure, the NIRS device will be applied to each of

the subject's anterior lower leg compartments using the adjustable elastic strap (similar to elastic knee brace) for the duration of the study procedure. Start and stop of light emission and acquisition is accomplished using the PC Acquisition Station (i.e. battery-powered laptop computers) via serial port cable (i.e. RS232 cable) which is connected to the device. After applying the NIRS devices to anterior compartments of each leg, a pneumatic cuff, a commercially available blood pressure device, and two commercially available pulse oximeters will be placed on the subject's body as per Figure 5-2. In addition, subject's leg under test will then be slightly elevated in reference to subject's torso (heart). The blood pressure device (BPC 81U, K061959, Medron, Inc., Taipei Hsien, Taiwan) is capable of storing up to 80 blood pressure readings in its internal memory and transferring them offline for display and storage onto PC. The pulse oximeter devices (CMS50D, K082641, Contec Medical System Co., Ltd., Shanghai, PRC) have the capability of transmitting heart rate (HR) and SpO_2 signals in "real-time" to PCs for display and storage.

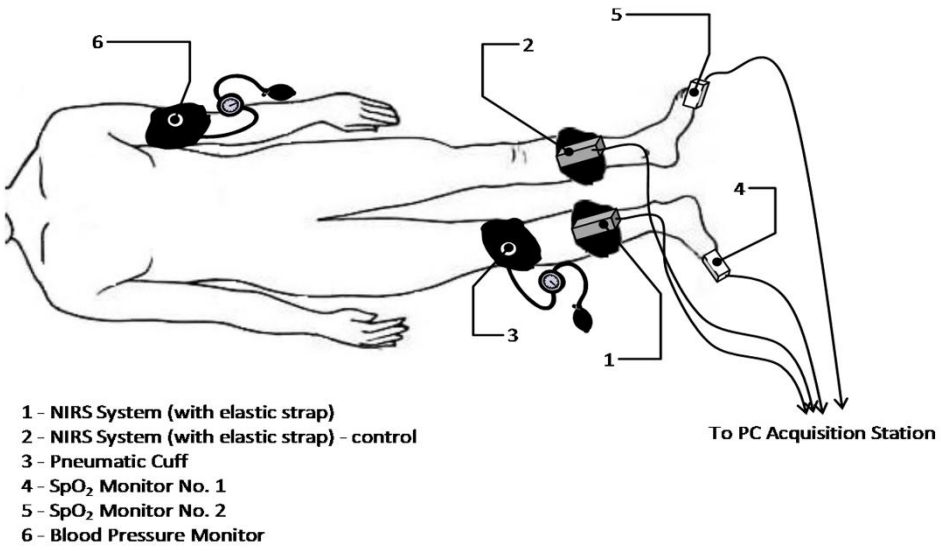

Figure 5-2 Study Procedure Setup

Once all devices are placed on the subject, acquisition of NIRS, HR, and SpO_2 signals will commence. The baseline blood pressure (BP1) value was taken and stored in device's internal memory. To verify normal (i.e. un-occluded) lower leg venous flow, the sound from a commercially available portable Doppler ultrasound device (Dopplex MD2, K930200, Huntleigh Diagnostics, Cardiff, UK) was recorded from either the great saphenous vein, the small saphenous vein, or the dorsal venous foot arch. The exact location depended on individual subject's vascular foot anatomy; however, once the specific site was selected, it was marked with a felt-tip marker for easier location during the study procedure. The Windows® Sound Recorder software was used to record Doppler sound onto laptop hard drive. Based on the procedure diagram and timeline outlined in Figure 5-3 and Figure 5-4, first 180 seconds of recorded data corresponded to subject's baseline (i.e. pneumatic cuff pressure at 0 mmHg) values. After 180 seconds, pneumatic cuff was inflated until a complete lower leg venous occlusion occured as verified by the Dopplex MD2 device. After 60 seconds of venous occlusion, pneumatic cuff was completely deflated. Blood pressure value was obtained and stored in device's memory (BP2). The study session signal recordings continued for additional 300 seconds. During this time, the venous flow in the lower leg returned to baseline level as verified by Doppler ultrasound. After 300 seconds, the final blood pressure value (BP3) was obtained and stored. At this point, the acquisition of NIRS data, HR, and SpO_2 signals was stopped. This indicated the end of the study procedure.

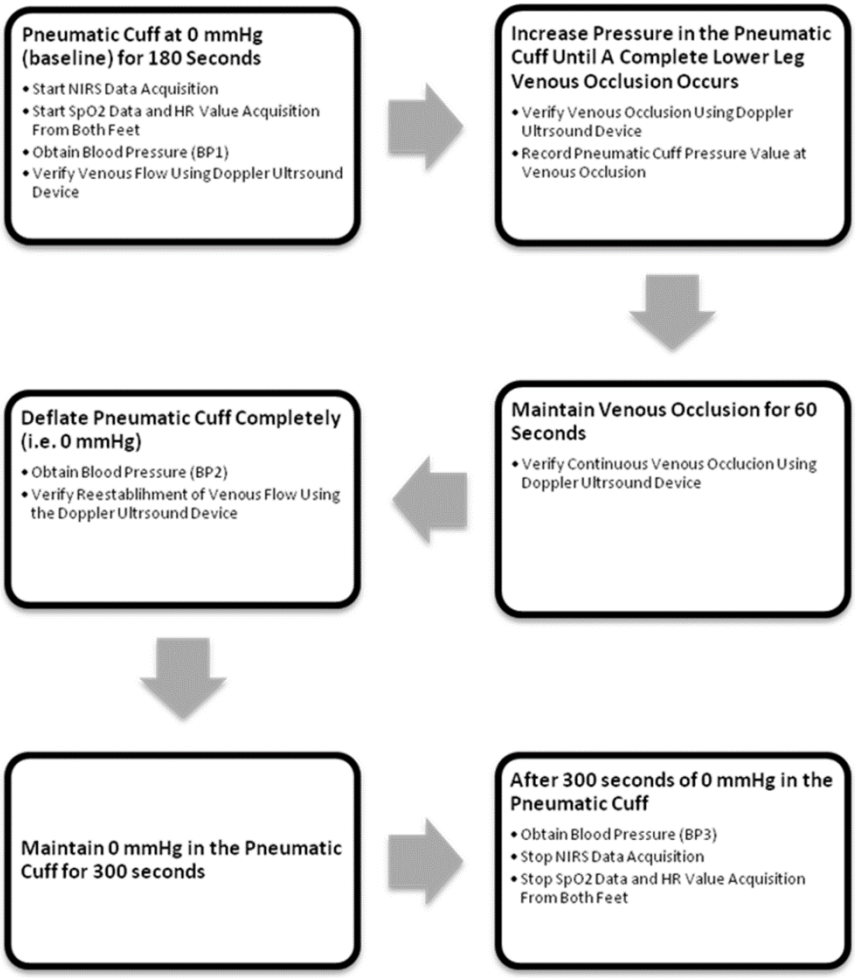

Figure 5-3 Study Procedure Outline

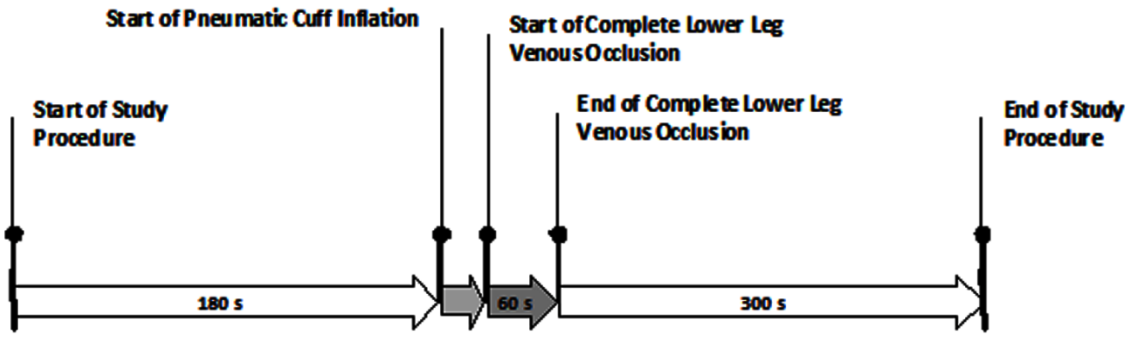

Figure 5-4 Study Procedure Timeline

5.4. Study Outcome Data

The study procedure calls for the acquisition of NIRS data and recording of BP, HR, and SpO_2 values. The NIRS data represents the changes in the amount of oxygenated (HbO_2) and deoxygenated (HHb) hemoglobin present at various depths in subject's anterior lower leg compartment. During the study procedure, NIRS data will be acquired prior (i.e. at baseline), during, and after the complete lower leg venous occlusion. The data from these three distinct scenarios should cause variations in the amount of HbO_2 and HHb present in the monitored compartment tissue. Recording of SpO_2 values (as percentage of arterial HbO_2 in blood) from toes of both feet will provide oxygenation levels of extremity under test and oxygenation of contralateral (i.e. "control") limb. In addition, SpO_2 devices provide arterial pulsatile waveform, which could be used for verification of continued arterial flow during the study. The blood pressure and heart rate readings were used to monitor subject's health status during the study procedure.

The recorded NIRS data was tested if the mean NIRS values from the leg under test [μ_T] are not significantly different from the mean NIRS values obtained from the contralateral (i.e. control) leg [μ_C] at baseline, during complete venous occlusion, and after the occlusion. The independent two-sided t-test with equal sample size and unknown variance using the 95-percent confidence interval was used for the analysis of all subjects. The hypothesis for this test is described as follows:

$$H_0: \mu_T - \mu_C = 0 \Rightarrow \mu_T = \mu_C$$

$$H_1: \mu_T - \mu_C \neq 0 \Rightarrow \mu_T \neq \mu_C$$

In addition to analysis on all subjects, the hypothesis that that data in female and male subjects are different was also tested. Specifically, we used a two sided *t*-test with equal means and equal but unknown variances of the null hypothesis that mean values from female subjects are equal to mean values from male subjects, against the alternative that the means are not equal. The hypothesis for this test is described as follows:

$$H_0: \mu_F - \mu_M = 0 \Rightarrow \mu_F = \mu_M$$

$$H_1: \mu_F - \mu_M \neq 0 \Rightarrow \mu_F \neq \mu_M$$

Chapter 6

Results of Clinical Testing

Based on the clinical protocol described in Chapter 5, physiological and near infrared spectroscopy data was collected from 22 healthy subjects during a two-week period at UCLA. Summary of subjects' age, blood pressure, and calf circumference are shown in Table 6-1. A total of 23 subjects were recruited, however, one subject was excluded from the study prior to data collection due to an exclusion condition marked in the Health History Questionnaire (Appendix A-2). From 22 subjects who completed the study, 16 were female and six male. Data file from one male subject was corrupt and was not used in data analysis.

Table 6-1 Study Subjects' Summary

Subject (n = 22)	***Minimum***	***Maximum***	***Mean***	***Median***
Age	22	27	23.89	24
S-BP at 0	81	143	110.56	111
D-BP at 0	56	78	66.96	67
S-BP at 240	90	135	108.81	107
D-BP at 240	52	73	62.74	66
S-BP at54 0	90	129	108.48	107
D-BP at 540	53	75	65.89	65
L-Calf Circumference* [mm]	280	410	34.42	345
R-Calf Circumference* [mm]	271	410	329.74	335

****Calf circumference was measured in 14 of 22 subjects at the optical module placement site.***

S-BP at 0 - systole blood pressure value at time (0 seconds); D-BP at 540 - diastole blood pressure value at time (540 seconds); L - left; R - right.

Based on the procedure diagram and timeline outlined in Figure 5-3 and Figure 6-1, respectively, the first 180 seconds of recorded data corresponded to subject's baseline (i.e. pneumatic cuff pressure at 0 mmHg) values. After 180 seconds, pneumatic cuff was inflated until a complete lower leg venous occlusion occurred as verified by Doppler ultrasound device. This period was marked as the venous occlusion [VO] and defined as follows:

$$Venous\ Occlusion\ [VO] = t_2 - t_1 \tag{6-1}$$

where
t_1 - three minutes after the start of the recording session
t_2 - five minutes before the end of the recording session

After 60 seconds of venous occlusion, pneumatic cuff was completely deflated (at time t_2) and the study session continued for additional 300 seconds. During this time, the venous flow was allowed to return to normal levels as verified by Doppler ultrasound. After the final 300 seconds, all data acquisition was stopped. This indicated the end of the study procedure. Throughout the clinical trial, two NIRS devices were alternatively placed on control and test legs of subjects in order to minimize inter-device bias. As a result, 11 subjects were recorded with device 001 on control (i.e. left) leg and 11 subjects were recorded with device 001 on test (i.e. right) leg.

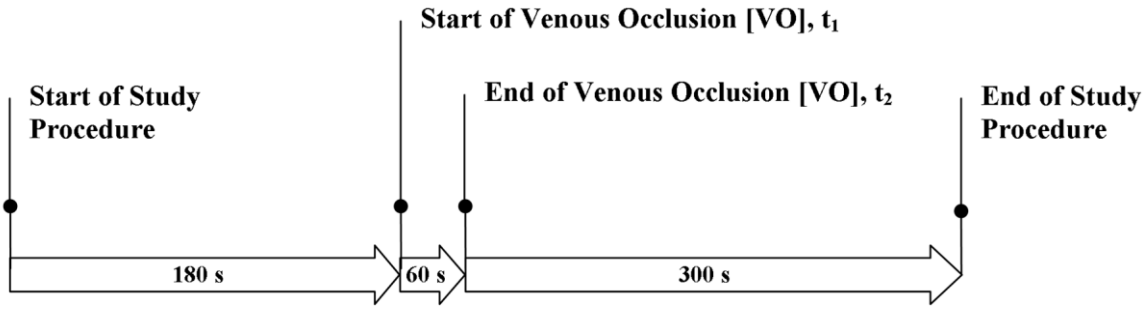

Figure 6-1 Study Procedure Timeline

The acquired NIRS data was sampled at 50 Hz. This sampling rate proved to be too high and data was down sampled to 20 Hz before analysis. We conducted data analysis using several different data modes, including raw data, normalized, pre- and post-venous occlusion, NIR and visible light. Raw data represents data that has only been down sampled to 20 Hz. Normalized (i.e. percent change) data was found from the following relationship:

$$Data_N = \frac{Data\,(t_1) - Data\,(t_2)}{Data\,(t_1)} \cdot 100\% \qquad (6\text{-}2)$$

where
Data (t_1) is raw data at the start of venous occlusion
Data (t_2) is raw data at the end of venous occlusion

We utilized data normalization in order to minimize any inter-device variations with respect to gain, offset, and optical components variations. Figure 6-2 shows typical data acquired from control and test legs during the study. Plots are displaying arbitrary units versus time. The arbitrary unit [AU] represents analog-to-digital converter LSB value as specified in equation (4-8). The beginning and ending of venous occlusion are marked with red vertical lines and denoted with t_1 and t_2, respectively. The periodic higher frequency signals visible in NIRS data

are artifacts originating from the PC computer used to acquire data from both devices simultaneously. These artifacts are due to the fact that two serial-to-USB port adapters were used to record NIRS data onto same PC hard drive. The PC bus priority was not always given to our serially-interfaced devices over internally connected PC peripherals (e.g., wireless card, Ethernet card).

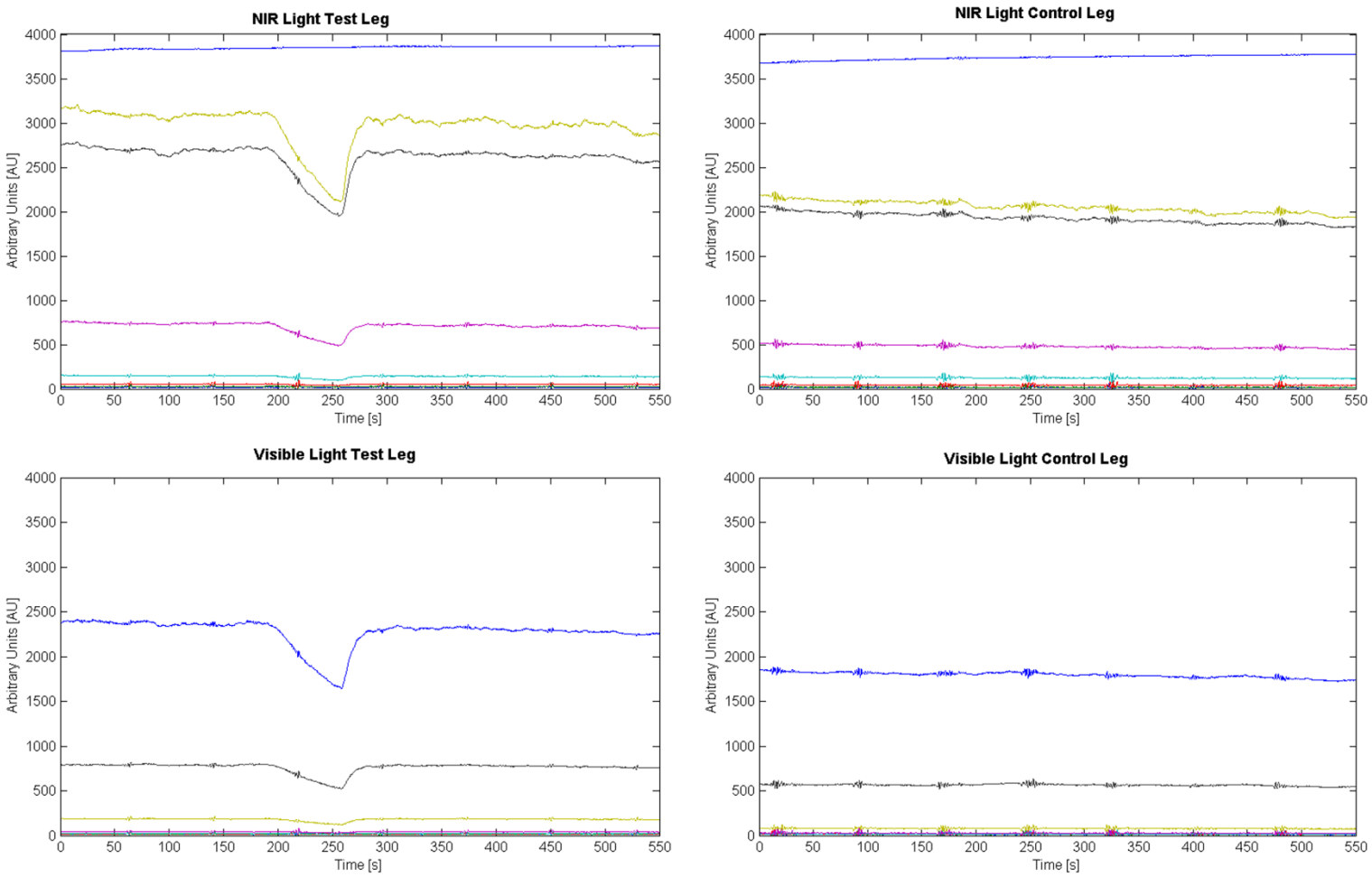

Figure 6-2 Acquired NIR (top left) and Visible (bottom left) Test Leg Data and NIR (top right) and Visible (bottom right) Control Leg Data

Before we start analyzing clinical significance of acquired NIRS data, we investigated the variability of our recorded data between subjects (control versus test) and between two NIRS devices used during the study. First, inter-subject variability and correlation were examined by plotting data from NIR sensors #3 and #5 (Figure 6-3) and visible light sensors #3 and #5 (Figure 6-4) at time t_1. These sensors were used as representative sensors which provided a broad range of light intensities while minimizing the possibility of saturating the detector or providing very low-level signals. The results show that both NIR and visible light sensors have very good correlation between control and test legs at time t_1. The variances seen between subjects may be attributed to variations of concentrations of specific chromophores of interest (e.g., oxygenated and deoxygenated hemoglobin) between different subjects.

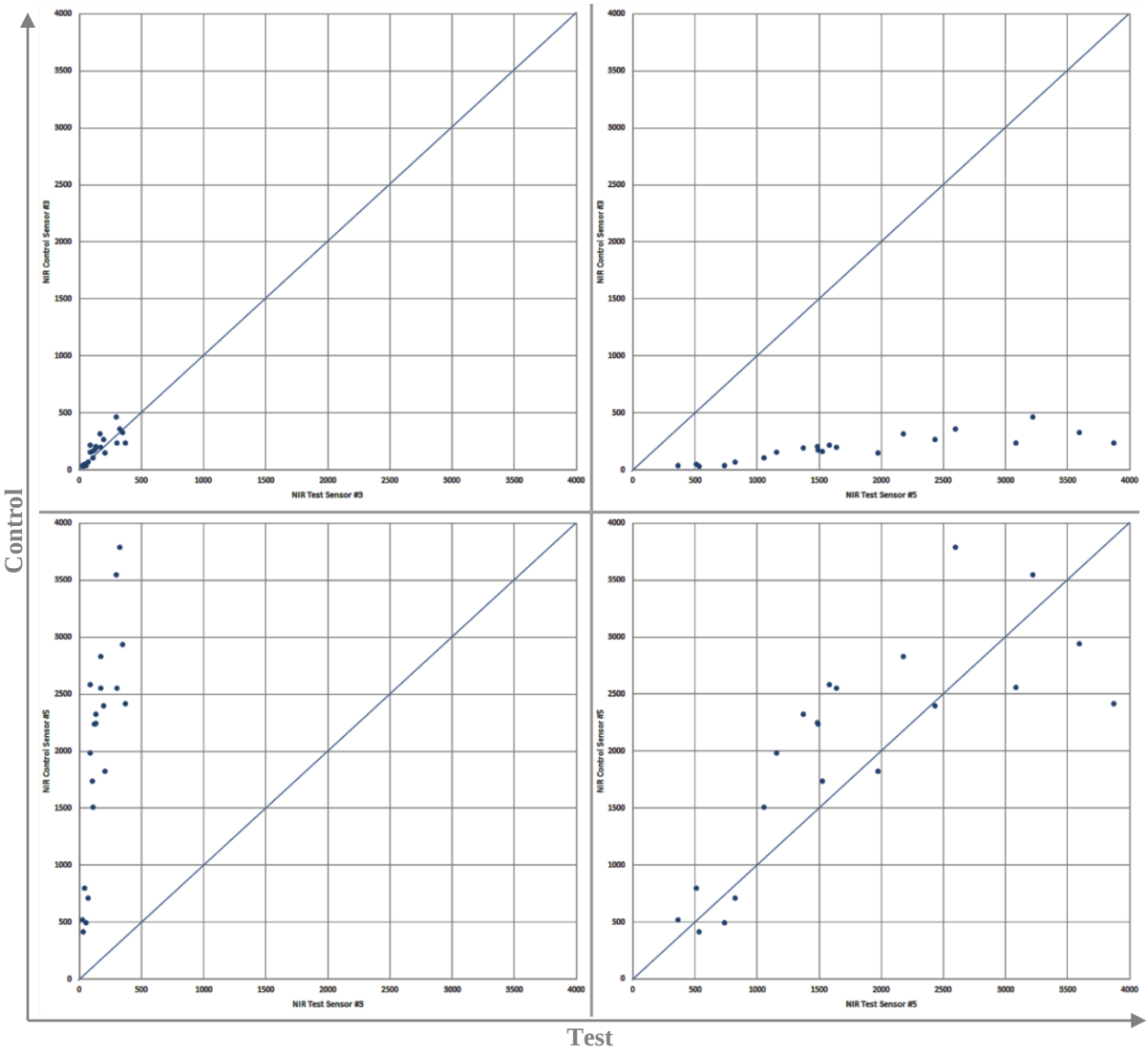

Figure 6-3 Example of NIR Light Sensors Correlations at Time t_1 Between Control Leg and Test Leg; top-left: Control S3 vs. Test S3; top-right: Control S3 vs. Test S5; bottom-left: Control S5 vs. Test S3; bottom-right: Control S5 vs. Test S5 (S – sensor)

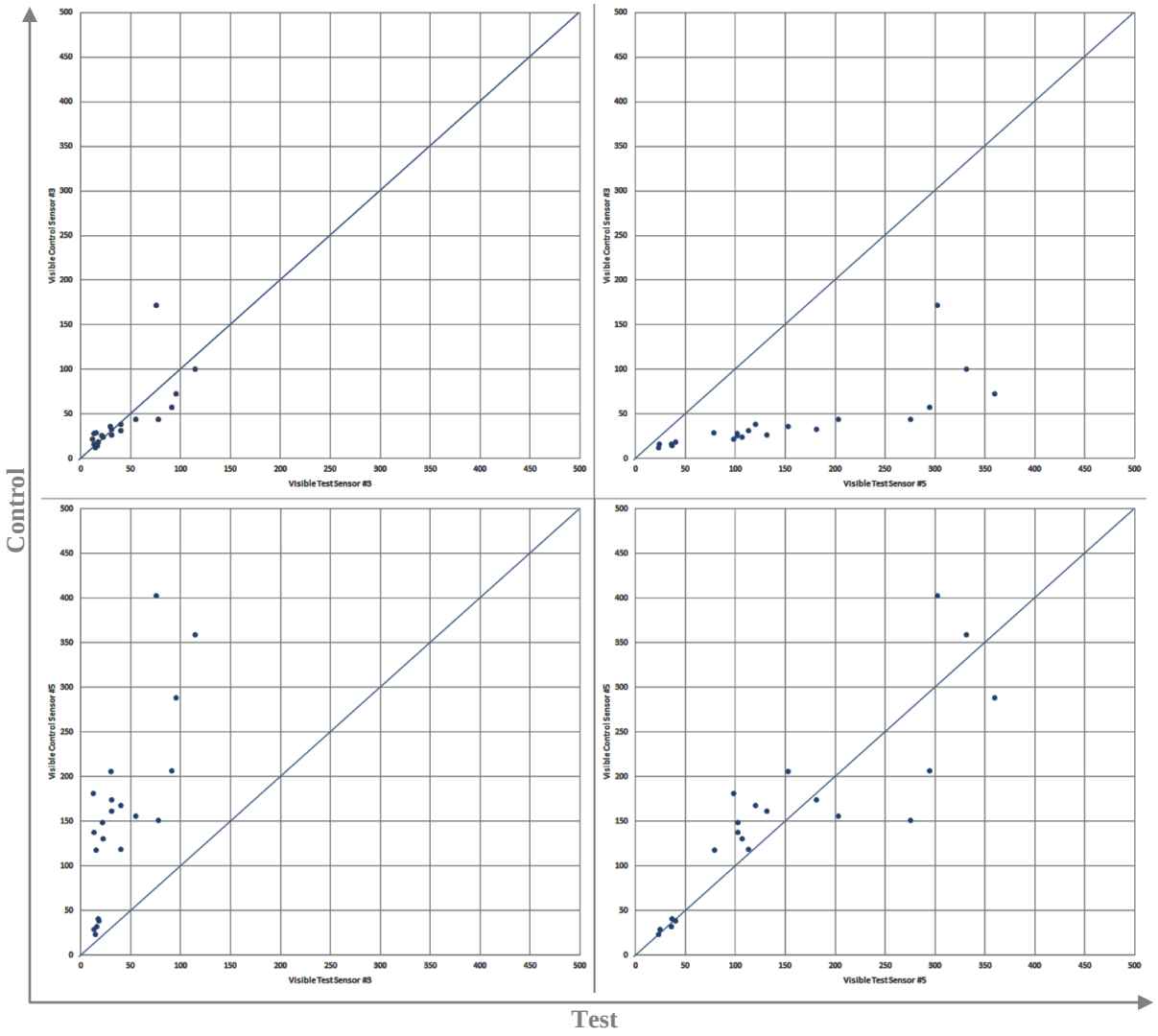

Figure 6-4 Example of Visible Light Sensors Correlations at Time t_1 Between Control Leg and Test Leg; top-left: Control S3 vs. Test S3; top-right: Control S3 vs. Test S5; bottom-left: Control S5 vs. Test S3; bottom-right: Control S5 vs. Test S5 (S – sensor)

In addition to exploring the variations between subjects, we wanted to better understand how much variance was present between two NIRS systems used in the study (control and test leg devices) for each subject. To do this, we used data for NIR Sensor #3 from control and test legs at time t_1 and from control leg at time t_2 (Table 6-2). First, we calculated mean and standard deviation values for each subject. Mean values ranged from 31 to 398 and standard deviations ranged from 1.35 to 87. Due to large range of mean and standard deviation values, we calculated

coefficient of variation [CV] as the ratio of standard deviation and mean. The CV provides us with the measure of how much variability is present in our data. Data of Table 6-2 shows that, in general, there is low variability between two devices per each subject. There are several subjects (e.g., 19, 9, 14), however, which could be considered as "outliers." In order to investigate if these outliers are result of inter-device variations, we explored the variation of the control leg device only between time t_1 and t_2. We accomplished this by removing data from test leg device, Test Time 1 column, and calculated intra-device CV (Table 6-3).

Table 6-2 NIR Light Sensor #3 Variations Between Control and Test Legs at Time t_1 and Control Leg at Time t_2

Subject	Control Time1	Test Time 1	Control Time 2	Mean [μ]	Standard Deviation [σ]	Coefficient of Variation [σ/μ]
1	197.16	170.64	201.74	189.8467	16.7904	0.0884
2	328.2	347.82	312.52	329.5133	17.6866	0.0537
3	463.02	299	432.64	398.2200	87.2593	0.2191
4	238.02	304.86	230.98	257.9533	40.7746	0.1581
5	108.4	110.28	107.66	108.7800	1.3507	0.0124
6	236.22	369.76	238.68	281.5533	76.3991	0.2713
7	164.74	106.3	163.08	144.7067	33.2715	0.2299
8	204.7	134.82	205.14	181.5533	40.4729	0.2229
9	313.14	169.32	309.1	263.8533	81.8932	0.3104
10	151.42	206.08	151.7	169.7333	31.4774	0.1855
11	32.32	29.44	31.04	30.9333	1.4430	0.0466
12	357.78	325.72	362.82	348.7733	20.1232	0.0577
13	189.98	131.84	188.58	170.1333	33.1704	0.1950
14	154.1	85.62	149.88	129.8667	38.3768	0.2955
15	265.04	197.02	277.78	246.6133	43.4189	0.1761
16	37.28	23.26	35.62	32.0533	7.6603	0.2390
17	66.24	72.44	63.12	67.2667	4.7441	0.0705
18	175.96	119.94	166.48	154.1267	29.9836	0.1945
19	219.68	89.36	219.1	176.0467	75.0734	0.4264
20	50.62	40.06	49.84	46.8400	5.8846	0.1256
21	38.18	52.5	47.62	46.1000	7.2800	0.1579

Table 6-3 NIR Light Sensor #3 Variations in Control Leg at Time t_1 and at Time t_2

Subject	Control Time1	Control Time 2	Mean [μ]	Standard Deviation [σ]	Coefficient of Variation [σ/μ]
1	197.16	201.74	199.4500	3.2385	0.0162
2	328.2	312.52	320.3600	11.0874	0.0346
3	463.02	432.64	447.8300	21.4819	0.0480
4	238.02	230.98	234.5000	4.9780	0.0212
5	108.4	107.66	108.0300	0.5233	0.0048
6	236.22	238.68	237.4500	1.7395	0.0073
7	164.74	163.08	163.9100	1.1738	0.0072
8	204.7	205.14	204.9200	0.3111	0.0015
9	313.14	309.1	311.1200	2.8567	0.0092
10	151.42	151.7	151.5600	0.1980	0.0013
11	32.32	31.04	31.6800	0.9051	0.0286
12	357.78	362.82	360.3000	3.5638	0.0099
13	189.98	188.58	189.2800	0.9899	0.0052
14	154.1	149.88	151.9900	2.9840	0.0196
15	265.04	277.78	271.4100	9.0085	0.0332
16	37.28	35.62	36.4500	1.1738	0.0322
17	66.24	63.12	64.6800	2.2062	0.0341
18	175.96	166.48	171.2200	6.7034	0.0392
19	219.68	219.1	219.3900	0.4101	0.0019
20	50.62	49.84	50.2300	0.5515	0.0110
21	38.18	47.62	42.9000	6.6751	0.1556

The values of coefficient of variability for control leg device range from 0.0013 to 0.1556 versus 0.0124 to 0.4264 for the case which also considered test leg device. Specifically, the CV values for "outlier" subjects mentioned above changed from 0.4246 to 0.0019 for subject #19, from 0.3104 to 0.0092 for subject #9, and from 0.2955 to 0.0196 for subject #14. These results indicates that variance in data between control and test sensors S3 on each subject may be attributed to variance in optical components. It may be recalled that in Chapter 4 we implemented calibration procedure in order to minimize inter-device variations in analog amplification chain (Section 4.5). The calibration procedure, however, did not address

differences that may exist between optical module components. Based on the above results, use of single device per patient in clinical setting may be justified in order to minimize variations caused by different optical modules. Now that data correlation between subjects has been verified and possible source of variance between control and test devices for each subject determined, we can examine clinical significance of acquired NIRS data.

The following sections will present analysis and results of feasibility study data and possible clinical implications of these findings. Results of our data analysis present data on a per-sensor basis and not on a device as a whole. The reason for this is a need to examine our research hypothesis that collection of depth-resolved NIRS data will provide useful information for analyzing the oxygenation state of the tissue. Based on subject population and possible clinical applications of the novel NIRS system, we divided data analysis into four main sections: (1) Detection of oxygenation abnormality without baseline data, (2) Oxygenation monitoring with baseline data; (3) Effect of venous occlusion on NIRS signal at different tissue depths; and (4) Gender differences. The first section explored the utility of NIRS system to detect the presence of venous occlusion. This situation may represent a clinical case where the perfusion abnormality is present at the time of application of the NIRS device. The second section investigated the utility of the NIRS system to detect onset of venous occlusion. Information gained from analyzing data in this section may be clinically applicable to cases where long-term monitoring of lower leg oxygenation is indicated due to the possibility of development of lower leg perfusion abnormalities, such as acute compartment syndrome. The third section explores information we obtained from different sampled tissue depths during venous occlusion and their effect on detected NIR and visible light intensities. We investigated depth-dependence with the hopes of gathering information that will enable us to customize novel NIRS device for specific

perfusion pathologies that are depth-dependent in order to maximize acquisition of clinically-relevant information from a patient. Data was analyzed on the entire sample and between genders. The fourth section examines the inter-gender dependence of the acquired NIRS data based on the known lower leg anatomical and physiological differences between females and males. The aim of this analysis was to see if NIRS system may detect inter-gender differences with the idea of using that information in the design of future clinical system.

6.1. Detection of Oxygenation Abnormality without Baseline

We performed statistical analysis to evaluate NIRS system performance without baseline data. This was done by looking at raw data at time t_2 at both control leg and test leg. Clinically, for example, this scenario simulates a case when the patient had suffered acute lower leg trauma or the monitoring of the patient's leg has started after the onset of the perfusion pathology. We performed a paired *t*-test with equal but unknown variance of the null hypothesis that the mean light intensity at time t_2 in control leg was equal to the mean light intensity at time t_2 in test leg. The alternative hypothesis stated that means control and test legs were not equal.

$$H_0: \mu_{Ct2} - \mu_{Tt2} = 0 \Rightarrow \mu_{Ct2} = \mu_{Tt2}$$

$$H_1: \mu_{Ct2} - \mu_{Tt2} \neq 0 \Rightarrow \mu_{Ct2} \neq \mu_{Tt2}$$

The result of hypothesis testing was returned as either a '1' or a '0'. The overall significance level was set at 0.05. Per-sensor significance level was set using the Bonferroni correction method, 0.05/8 = 0.0063 (i.e. 0.63 percent). If the result was a '1', then the null hypothesis was rejected at the overall five percent significance level (i.e. 95 percent confidence interval). If the hypothesis

testing results was a '0', then the test failed to reject the null hypothesis at the overall five percent significance level (i.e. 95 percent confidence interval).

We first analyzed data between control and test legs from NIR light sensors at time t_2, equation (6-8). To see how well data is correlated between sensors on control and test legs, we plotted the raw NIR control leg data versus raw NIR test leg data (Figure 6-5) for all subjects and eight NIR sensors. The results showed that three (out of eight total) sensors detected statistically significant values at the post-occlusion time (Figure 6-6 and Table 6-4).

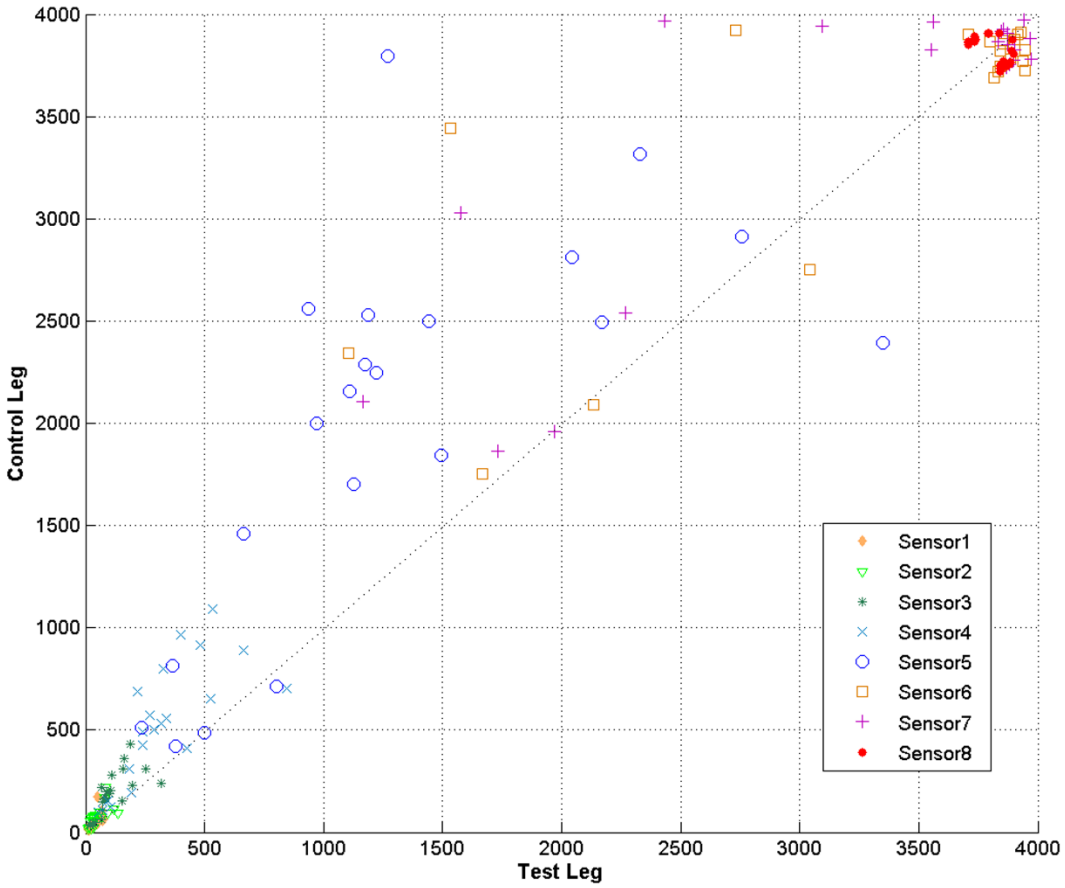

Figure 6-5 Control versus Test Legs Raw NIR Light Intensities per Each Sensor at Time t_2

$$x = NIRControlTime2$$

$$y = NIRTestTime2$$

$$boxplot = NIRControlTime2 - NIRTestTime2 \quad (6\text{-}3)$$

where
NIRControlTime2 – raw NIR light data from the control leg at time t_2
NIRTestTime2 – raw NIR light data from the test leg at time t_2

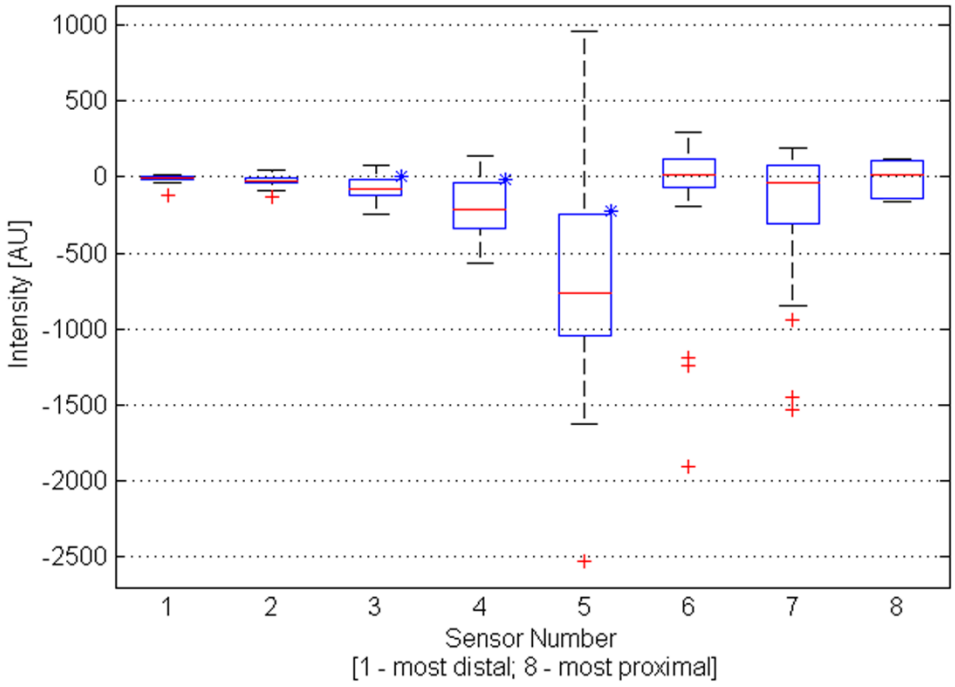

Figure 6-6 Change in Raw NIR Light Intensity Between Control and Test Legs at Time t_2

Table 6-4 Raw NIR Light Intensity Data Between Control and Test Legs at Post Occlusion Time (t_2)

Channel (distal->proximal)	1	2	3	4	5	6	7	8
Reject Ho at α = 0.0063?	0	0	1	1	1	0	0	0
Reject Ho at α = 0.05?	0	1	1	1	1	0	1	0
P Value	0.064	0.007	0.000	0.000	0.000	0.211	0.033	0.629

H_0: mean of NIR light intensity in control leg at t_2 equal to mean of test leg at t_2
H_1: mean of NIR light intensity in control leg at t_2 not equal to mean of test leg at t_2

Next, we analyzed data between control and test legs from visible light sensors at time t_2, equation (6-9). To see how well data is correlated between visible light sensors on control and test legs, we plotted the raw visible control leg data versus raw visible test leg data (Figure 6-7) for all subjects and all visible sensors. We see that data is highly correlated and it shows decrease in test leg intensity due to venous occlusion as compared to the non-occluded control leg. In this group, two of eight sensors showed statistical significance.

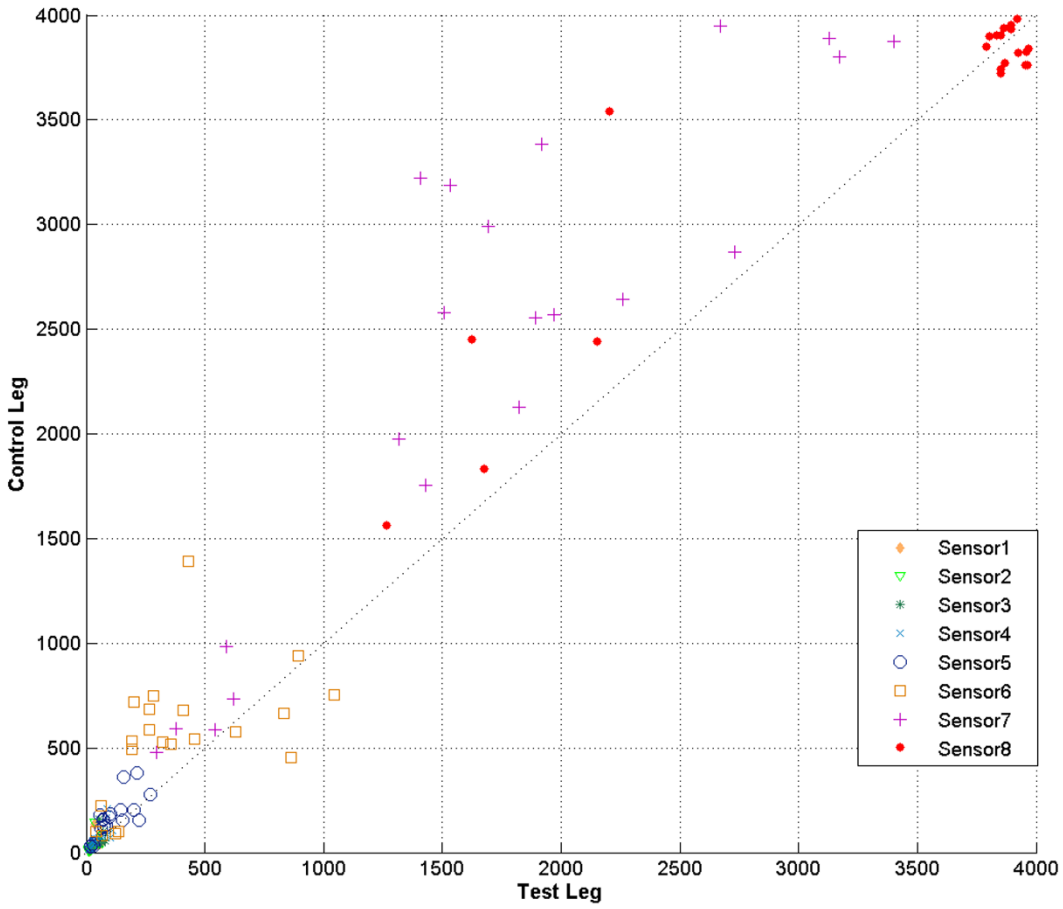

Figure 6-7 Control versus Test Legs Raw Visible Light Intensities per Each Sensor at Time t_2

$$x = visControlTime2$$

$$y = visTestTime2$$

$$boxplot = visControlTime2 - visTestTime2 \quad (6\text{-}4)$$

where
visControlTime2 – raw visible light data from the control leg at time t_2
visTestTime2 – raw visible data from the test leg at time t_2

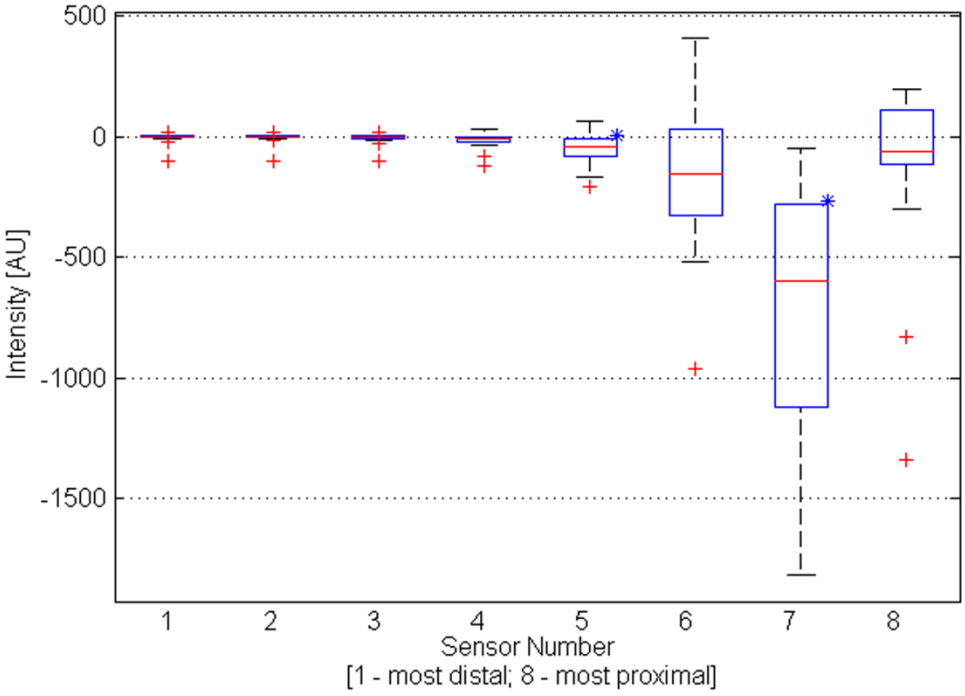

Figure 6-8 Change in Raw Visible Light Intensity Between Control and Test Legs at Time t_2

Table 6-5 Raw Visible Light Intensity Data Between Control and Test Legs at Post Occlusion Time (t_2)

Channel (distal->proximal)	1	2	3	4	5	6	7	8
Reject Ho at α = 0.0063?	0	0	0	0	1	0	1	0
Reject Ho at α = 0.05?	0	0	0	1	1	1	1	0
P Value	0.481	0.465	0.194	0.019	0.001	0.026	0.000	0.170

H_0: mean of visible light intensity in control leg at t_2 equal to mean in test leg at t_2
H_1: mean of visible light intensity in control leg at t_2 not equal to mean in test leg at t_2

These results indicate that the NIRS system is capable of detecting the existence of lower leg tissue oxygenation abnormality in five out of sixteen sensors using raw data without baseline. It is worth mentioning that statistical results were obtained using the Bonferroni correction method, which is a very conservative method of obtaining corrected significance level. If, for example, we had used the 0.05 level per-sensor, we would have obtained statistically significant results in nine out of sixteen sensors. Clinically, these results may provide useful information about which sensors are better suited for detecting depth-dependent pathologies and may, therefore, be used to customize optical module and data acquisition unit.

6.2. Oxygenation Monitoring with Baseline

We investigated the utility of the NIRS system to detect onset of venous occlusion (i.e. oxygenation abnormality). Clinically, this scenario simulates a case where NIRS system would be placed on a patient to monitor tissue oxygenation state when there is a possibility for development of lower leg perfusion abnormality.

To accomplish this, we used raw data to perform a paired *t*-test with equal but unknown variance of the null hypothesis that the mean light intensity at time t_2 (oxygenation abnormality) was equal to the mean light intensity at time t_1 (baseline). The alternative hypothesis stated that means at t_2 and t_1 were not equal.

$$H_0: \mu_{t2} - \mu_{t1} = 0 \Rightarrow \mu_{t2} = \mu_{t1}$$

$$H_1: \mu_{t2} - \mu_{t1} \neq 0 \Rightarrow \mu_{t2} \neq \mu_{t1}$$

The result of hypothesis testing was returned as either a '1' or a '0'. The overall significance level was set at 0.05. Per-sensor significance level was set using the Bonferroni correction method, 0.05/8 = 0.0063 (i.e. 0.63 percent). If the result was a '1', then the null hypothesis was rejected at the overall five percent significance level (i.e. 95 percent confidence interval). If the hypothesis testing results was a '0', then the test failed to reject the null hypothesis at the overall five percent significance level (i.e. 95 percent confidence interval).

First, we tested the hypothesis for the change of raw NIR light intensity in control leg during venous occlusion, equation (6-5). The results show that three most proximal NIR sensors (out of eight total) exhibited significant change in the NIR light between times t_2 and t_1 (Figure 6-9 and Table 6-6). As mentioned above, the more proximal sensors sample more superficial levels of tissue. During the approximately 60 seconds of venous occlusion period, blood flow at the surface changes more readily than in the deeper parts of the tissue. This is a known phenomenon in pulse oximetry which introduces baseline drift in the acquired signal where surface oxygenation varies due to local auto regulation and sympathetic outflow, as well as due to respiratory fluctuations in central venous pressure [83]. Therefore, these surface changes may explain the significance of NIR sensors six and seven. The most proximal NIR sensor, sensor number eight, however, has been determined to provide mostly unreliable data due to its close proximity to the photo detector.

$$\begin{aligned} x &= NIRControlTime2 \\ y &= NIRControlTime1 \\ boxplot &= NIRControlTime2 - NIRControlTime1 \end{aligned} \qquad (6\text{-}5)$$

where
NIRControlTime2 – raw NIR light data from the control leg at time t_2
NIRControlTime1 – raw NIR light data from the control leg at time t_1

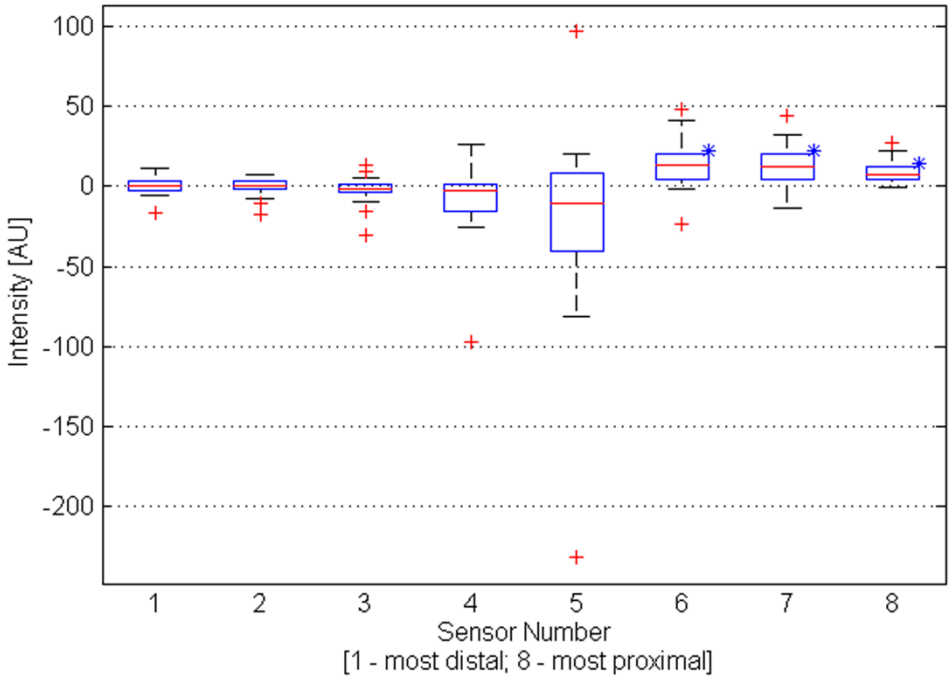

Figure 6-9 Change in Raw NIR Light Intensity In Control Leg During Venous Occlusion

Table 6-6 Change in NIR Light Intensity in Control Leg During Venous Occlusion

Channel (distal->proximal)	1	2	3	4	5	6	7	8
Reject Ho at α = 0.0063?	0	0	0	0	0	1	1	1
Reject Ho at α = 0.05?	0	0	0	0	0	1	1	1
P Value	0.995	0.680	0.259	0.112	0.113	0.001	0.000	0.000

H_0: mean of NIR light intensity at t_2 equal to mean at t_1
H_1: mean of NIR light intensity at t_2 not equal to mean at t_1

Second, we tested the hypothesis for the change of raw visible light intensity in control leg during venous occlusion, equation (6-6). The results show that only the most proximal visible sensors (out of eight total) exhibited significant change in the visible light between times t_2 and t_1 (Figure 6-10 and Table 6-7). Once again, this significance in the control leg change of visible light could be explained by the surface oxygenation variability of the superficial tissue levels.

$$x = visControlTime2$$
$$y = visControlTime1$$
$$boxplot = visControlTime2 - visControlTime1 \quad (6\text{-}6)$$

where
visControlTime2 – raw visible light data from the control leg at time t_2
visControlTime1 – raw visible light data from the control leg at time t_1

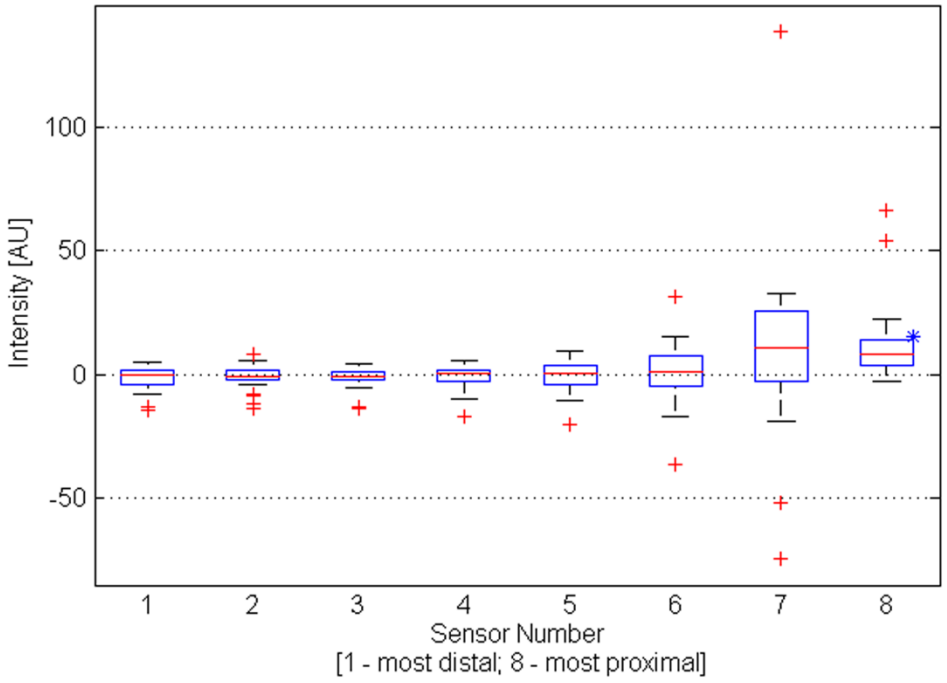

Figure 6-10 Change in Raw Visible Light Intensity On Control Leg During Venous Occlusion

Table 6-7 Change in Visible Light Intensity in Control Leg During Venous Occlusion

Channel (distal->proximal)	1	2	3	4	5	6	7	8
Reject Ho at α = 0.0063?	0	0	0	0	0	0	0	1
Reject Ho at α = 0.05?	0	0	0	0	0	0	0	1
P Value	0.164	0.355	0.137	0.217	0.441	0.921	0.268	0.004

H_0: mean of visible light intensity at t_2 equal to mean at t_1
H_1: mean of visible light intensity at t_2 not equal to mean at t_1

Next, we tested the hypothesis for detected raw NIR light intensity change in test leg during venous occlusion, equation (6-7). The results show that there are five (out of eight total) NIR sensors that reported statistically significant changes in detected light intensities in test leg (Figure 6-11). The sensors that did not report statistical significance at the 0.63 percent level were sensors number one, six, and seven. Again, these results were obtained using the Bonferroni correction method, which is a very conservative method of obtaining corrected significance level.

$$x = NIRTestTime2$$
$$y = NIRTestTime1$$
$$boxplot = NIRTestTime2 - NIRTestTime1 \quad (6\text{-}7)$$

where
NIRTestTime2 – raw NIR light data from the test leg at time t_2
NIRTestTime1 – raw NIR light data from the test leg at time t_1

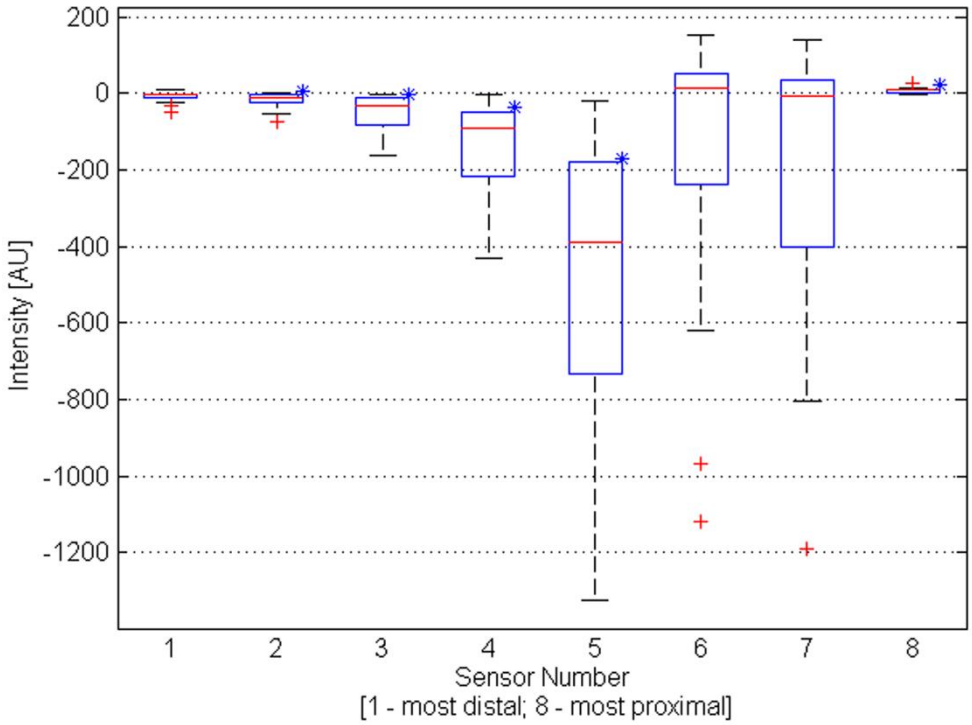

Figure 6-11 Change in Raw NIR Light Intensity On Test Leg During Venous Occlusion

Table 6-8 Change in NIR Light Intensity in Test Leg During Venous Occlusion

Channel (distal->proximal)	1	2	3	4	5	6	7	8
Reject Ho at α = 0.0063?	0	1	1	1	1	0	0	1
Reject Ho at α = 0.05?	1	1	1	1	1	0	1	1
P Value	0.010	0.000	0.000	0.000	0.000	0.058	0.013	0.000

H_0: mean of NIR light intensity at t_2 equal to mean at t_1
H_1: mean of NIR light intensity at t_2 not equal to mean at t_1

Finally, we tested the hypothesis for detected visible light intensity change in test leg during venous occlusion. We found that five (out of eight total) visible sensors reported statistically significant changes in detected raw light intensities in test leg (Figure 6-12 and Table 6-9).

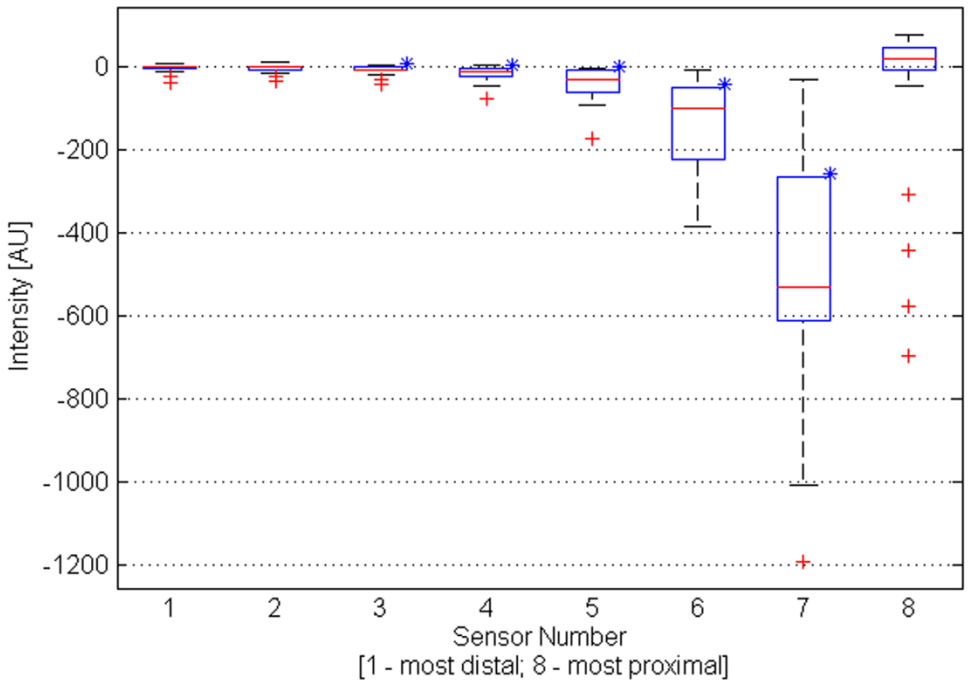

Figure 6-12 Change in Raw Visible Light Intensity On Test Leg During Venous Occlusion

Table 6-9 Change in Visible Light Intensity in Test Leg During Venous Occlusion

Channel (distal->proximal)	1	2	3	4	5	6	7	8
Reject Ho at α = 0.0063?	0	0	1	1	1	1	1	0
Reject Ho at α = 0.05?	1	1	1	1	1	1	1	0
P Value	0.036	0.028	0.004	0.001	0.000	0.000	0.000	0.160

H_0: mean of visible light intensity at t_2 equal to mean at t_1
H_1: mean of visible light intensity at t_2 not equal to mean at t_1

The above results for both NIR and visible light changes in test leg during venous occlusion indicate that the novel NIRS system is able to reliably detect onset of lower leg oxygenation abnormality (i.e. venous occlusion) in 10 out of 16 sensors at the 0.63 percent significance level per sensor. These results were obtained using the conservative Bonferroni correction method. If, for example, we had used the 0.05 level per sensor, we would have obtained statistically significant results in 14 out of 16 sensors. This information may be clinically applicable to cases where long-term monitoring of lower leg oxygenation is indicated due to the possibility of development of lower leg perfusion abnormalities.

6.3. Effect of Venous Occlusion on NIRS Signal at Different Tissue Depths

We wanted to explore the relationship between the control and test leg data for NIR and visible light intensities versus the approximate depth of sampled tissue. To do this, we plotted the mean differences in percent change of NIR light data (equations (6-8) and (6-9)) and of visible light data (equations (6-10) and (6-11)) between test and control legs versus the approximate depth of sampled tissue and sensor position (Figure 6-13).

$$y_{NIR} = \overline{\left[\frac{NIR_{test}(t_1) - NIR_{test}(t_2)}{NIR_{test}(t_1)} \cdot 100\%\right]} - \overline{\left[\frac{NIR_{control}(t_1) - NIR_{control}(t_2)}{NIR_{control}(t_1)} \cdot 100\%\right]} \quad (6\text{-}8)$$

$$y_{NIR} = y_{NIRtest} - y_{NIRcontrol} \quad (6\text{-}9)$$

where
$NIR_{test}(t_1)$ is raw NIR light data from test leg at the start of venous occlusion
$NIR_{control}$ (t_2) is raw NIR light data from the control leg at the end of venous occlusion
$y_{NIRtest}$ is mean percent change of NIR light test leg data
$y_{NIRcontrol}$ is mean percent change of NIR light control leg data

$$y_{VIS} = \overline{\left[\frac{VIS_{test}(t_1) - VIS_{test}(t_2)}{VIS_{test}(t_1)} \cdot 100\%\right]} - \overline{\left[\frac{VIS_{control}(t_1) - VIS_{control}(t_2)}{VIS_{control}(t_1)} \cdot 100\%\right]} \quad (6\text{-}10)$$

$$y_{VIS} = y_{VIStest} - y_{VIScontrol} \quad (6\text{-}11)$$

where
$VIS_{test}(t_1)$ is raw visible light data from test leg at the start of venous occlusion
$VIS_{control}$ (t_2) is raw visible data from the control leg at the end of venous occlusion
$y_{VIStest}$ is mean percent change of visible light test leg data
$y_{VIScontrol}$ is mean percent change of visible light control leg data

For NIR light data, the minimum depth of sampled tissue was 5.56 mm, while the maximum depth of sampled tissue was 28.25 mm (as set by the shortest and longest inter-optode distances, respectively). The range of mean difference in percent change of intensity for NIR

light was measured from -26.38 % to -0.039 %. This range is approximately the same as the difference between the baseline and venous occlusion states obtained using dynamic Monte Carlo simulations (Section 3.6.4). The negative percentage changes denote decrease in light intensity during venous occlusion that is attributed to the increase in the concentration of specific chromophores in sampled tissue. In other words, decrease in detected light intensity means that more light was absorbed by the increased number of chromophores. The standard deviation for the mean difference in percent change was 9.01 with overall mean value of -17.70%. For visible light data, the approximate depth of sampled tissue was the same as for the NIR light. The range of mean difference in percent change of visible light intensity was measured from -28.93 % to -0.896 %. This range is approximately twice as large as the difference between the baseline and venous occlusion states obtained using dynamic Monte Carlo simulations (Section 3.6.4). Possible cause for these different values may be attributed to the limitations of Monte Carlo simulations, as outlined in Section 3.6.4. The standard deviation for the mean difference in percent change was 10.72 with overall mean value of -16.09 %.

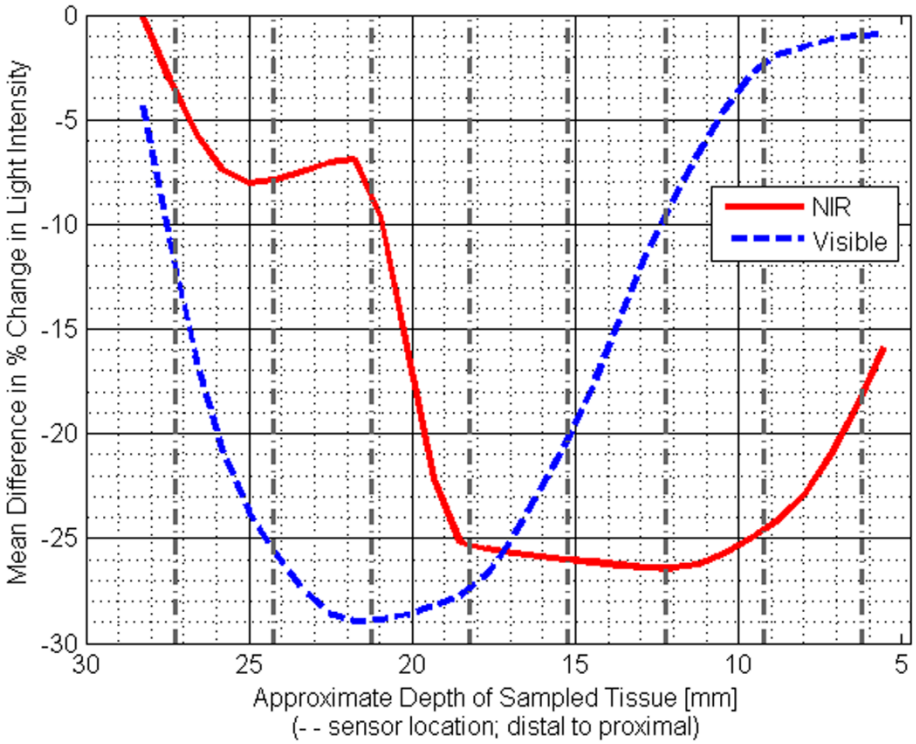

Figure 6-13 Mean Difference In Percent Change of NIR and Visible Light Versus Approximate Depth of Sampled Tissue

The results obtained above for the entire subject sample, indicate that, during venous occlusion, deeper muscle tissues experience greater change in deoxygenated hemoglobin levels, while more superficial tissues show more pronounced changes in oxygenated and very little changes in the deoxygenated hemoglobin levels.

In addition to looking at the entire sample size, mean difference in percent change of NIR and visible light intensities between test and control legs were plotted for female and male subjects. NIR light data plot (Figure 6-14) shows that female subjects experienced greater oxygenated hemoglobin changes in superficial tissues, while male subjects did in deeper tissues.

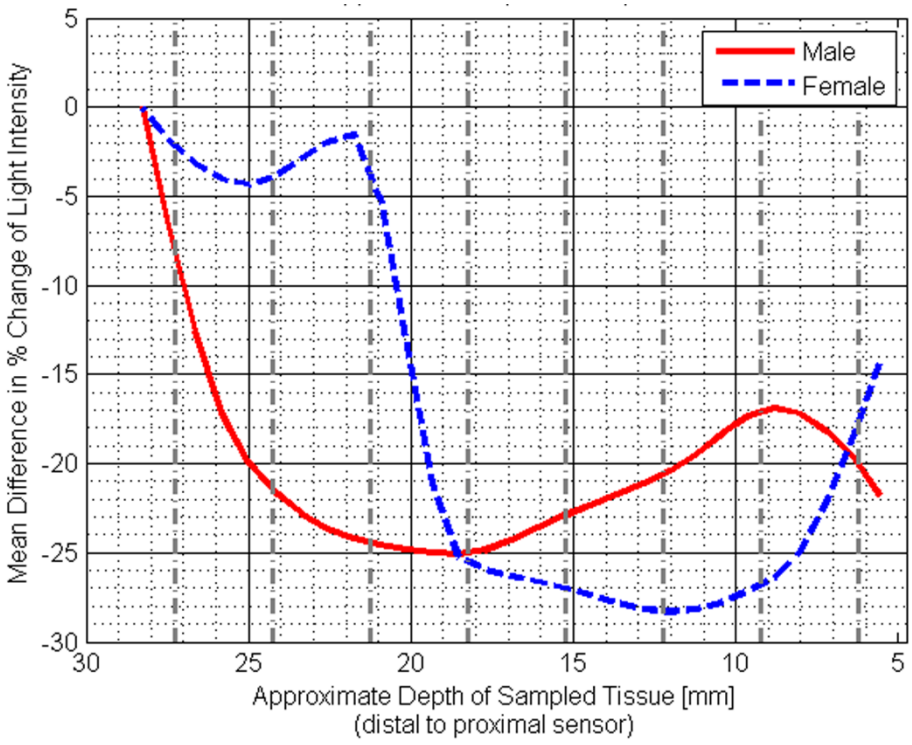

Figure 6-14 Mean Difference In Percent Change of NIR Light Versus Approximate Depth of Sampled Tissue for Female and Male Subjects

On the other hand, visible light data plot (Figure 6-15) shows that both female and male subjects experienced similar deoxygenated hemoglobin changes for both superficial and deeper tissues.

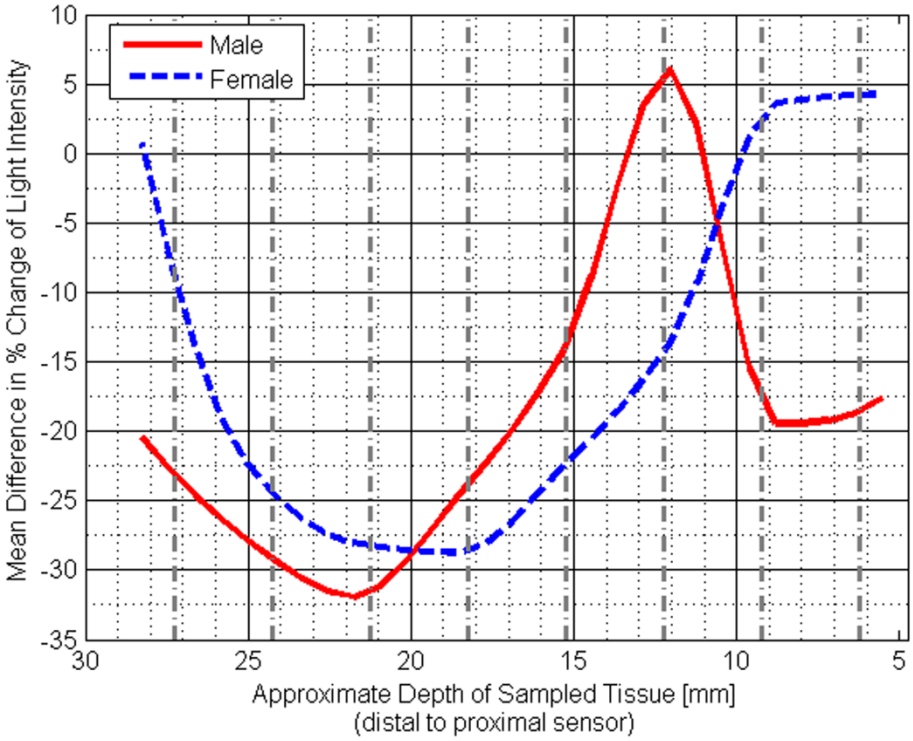

Figure 6-15 Mean Difference In Percent Change of Visible Light Versus Approximate Depth of Sampled Tissue for Female and Male Subjects

Based on the above results, it may be possible to customize optical configuration and per-sensor gain of the novel NIRS system for specific depth-dependent perfusion pathologies in order to maximize acquisition of clinically-relevant information.

6.4. Gender Differences

Based on the known lower leg anatomical and physiological differences between females and males, we hypothesized that there were inter-gender variations in the acquired NIRS data. We tested for these variations in both control and test legs, as well as for NIR and visible lights. The hypothesis was tested using an unpaired two sided *t*-test with equal means and equal but unknown variances. The null hypothesis stated that mean values from female subjects were

equal to mean values from male subjects. The alternative hypothesis stated that the means were not equal. The hypothesis testing is described as follows:

$$H_0: \mu_F - \mu_M = 0 \Rightarrow \mu_F = \mu_M$$

$$H_1: \mu_F - \mu_M \neq 0 \Rightarrow \mu_F \neq \mu_M$$

The result of hypothesis testing was returned as either a '1' or a '0'. As in Section 6.1, the overall significance level was set at 0.05, while per-sensor significance level was set using the Bonferroni correction method, 0.05/8 = 0.0063 (i.e. 0.63 percent). If the result was a '1', then the null hypothesis was rejected at the overall five percent significance level (i.e. 95 percent confidence interval). If the hypothesis testing result was a '0', then the test failed to reject the null hypothesis at the overall five percent significance level (i.e. 95 percent confidence interval).

Using the raw NIRS data, we performed statistical analysis between females and males to see if light intensities on control leg before venous occlusion (i.e. at time t_1) presented significant difference between these two populations. The results showed a statistically significant difference between females and males in six out of eight NIR light sensors and in four out of eight visible light sensors, at 0.63 percent significance level per-sensor. The NIR sensors that did not show statistically significant difference were the most distal and most proximal sensors. The four visible light sensors that did not show statistically significant difference were four most distal sensors. Summary of these results, along with corresponding *p* values are shown in Table 6-10.

Table 6-10 Raw NIR and Visible Light Intensities on Control Leg Between Genders at Pre-Occlusion Time (t_1)

NIR								
Channel (distal->proximal)	1	2	3	4	5	6	7	8
Reject Ho at α = 0.0063?	0	1	1	1	1	1	1	0
Reject Ho at α = 0.05?	1	1	1	1	1	1	1	0
P Value	0.040	0.003	0.000	0.000	0.000	0.000	0.000	0.602
Visible								
Channel (distal->proximal)	1	2	3	4	5	6	7	8
Reject Ho at α = 0.0063?	0	0	0	0	1	1	1	1
Reject Ho at α = 0.05?	0	0	0	1	1	1	1	1
P Value	0.153	0.114	0.073	0.012	0.000	0.000	0.000	0.000

H_0: raw light intensity values of male equal to values of female on control leg
H_1: raw light intensity values of male not equal to values of female on control leg

Next, we performed statistical analysis on raw data between females and males to see if light intensities on test leg before venous occlusion exhibited significant difference between these two populations. The results showed a statistically significant difference between females and males in five out of eight NIR light sensors and in four out of eight visible light sensors, at 0.63 percent significance level per sensor. The three NIR sensors that did not show statistically significant difference were two most distal and the most proximal sensors. The four visible light sensors that did not show statistically significant difference were again four most distal sensors. Summary of these results, along with corresponding *p* values are shown in Table 6-11.

Table 6-11 Raw NIR and Visible Light Intensities on Test Leg Between Genders at Pre-Occlusion Time (t_1)

NIR								
Channel (distal->proximal)	1	2	3	4	5	6	7	8
Reject Ho at α = 0.0063?	0	0	1	1	1	1	1	0
Reject Ho at α = 0.05?	1	1	1	1	1	1	1	0
P Value	0.042	0.016	0.003	0.001	0.001	0.000	0.000	0.803
Visible								
Channel (distal->proximal)	1	2	3	4	5	6	7	8
Reject Ho at α = 0.0063?	0	0	0	0	1	1	1	1
Reject Ho at α = 0.05?	0	0	1	1	1	1	1	1
P Value	0.098	0.088	0.045	0.013	0.002	0.004	0.000	0.000

H_0: raw light intensity values of male equal to values of female on test leg
H_1: raw light intensity values of male not equal to values of female on test leg

In addition to conducting statistical analysis on raw data between females and males at time t_1, we also wanted to see if there were inter-gender differences between control and test legs at time t_2. First, we conducted a statistical analysis on data from the control leg. The results showed a statistically significant difference between females and males in six out of eight NIR light sensors and in five out of eight visible light sensors. The two NIR sensors that did not show statistically significant difference were the most distal and the most proximal sensors. The four visible light sensors that did not show statistically significant difference were the four most distal sensors. Summary of these results, along with corresponding *p* values are shown in Table 6-12.

Table 6-12 Raw NIR and Visible Light Intensities on Control Leg Between Genders at Post Occlusion Time (t_2)

NIR								
Channel (distal->proximal)	1	2	3	4	5	6	7	8
Reject Ho at α = 0.0063?	0	1	1	1	1	1	1	0
Reject Ho at α = 0.05?	0	1	1	1	1	1	1	0
P Value	0.067	0.003	0.000	0.000	0.000	0.000	0.000	0.525
Visible								
Channel (distal->proximal)	1	2	3	4	5	6	7	8
Reject Ho at α = 0.0063?	0	0	0	0	1	1	1	1
Reject Ho at α = 0.05?	0	0	0	1	1	1	1	1
P Value	0.190	0.148	0.061	0.010	0.000	0.000	0.000	0.000

H_0: raw light intensity values of male equal to values of female on control leg
H_1: raw light intensity values of male not equal to values of female on control leg

Second, we conducted a statistical analysis on data from the test leg. The results showed significant difference in four out of eight NIR light sensors and in three out of eight visible light sensors, at 0.63 percent significance level per sensor. Summary of these results, along with corresponding *p* values are shown in Table 6-13.

Table 6-13 Raw NIR and Visible Light Intensities on Test Leg Between Genders at Post Occlusion Time (t_2)

NIR								
Channel (distal->proximal)	1	2	3	4	5	6	7	8
Reject Ho at α = 0.0063?	0	0	0	1	1	1	1	0
Reject Ho at α = 0.05?	1	1	1	1	1	1	1	0
P Value	0.046	0.027	0.007	0.002	0.004	0.000	0.000	0.807
Visible								
Channel (distal->proximal)	1	2	3	4	5	6	7	8
Reject Ho at α = 0.0063?	0	0	0	0	1	0	1	1
Reject Ho at α = 0.05?	0	0	0	1	1	1	1	1
P Value	0.056	0.064	0.053	0.013	0.003	0.007	0.000	0.000

H_0: raw light intensity values of male equal to values of female on test leg
H_1: raw light intensity values of male not equal to values of female on test leg

The results from pre- and post-venous occlusion times data in both control and test legs indicate that the NIRS system is capable of recording statistically significant information regarding the oxygenated and deoxygenated hemoglobin levels between genders during normal and abnormal oxygenation states of lower leg tissues. The importance of these findings, for both baseline and venous occlusion cases, rests in the fact that the future clinical NIRS system optical module and detection algorithms may be optimized in order to maximize acquisition of clinically-relevant information.

6.5. Discussion

The purpose of this feasibility study was to evaluate the performance of the novel NIRS system in detection of oxygenated and deoxygenated hemoglobin changes at various tissue depth levels during venous occlusion in the lower leg. Our research hypothesis states that multi-channel depth-resolved near infrared spectroscopy can be used to monitor lower leg tissue oxygenation and lower leg oxygenation abnormalities. To simulate lower leg oxygenation abnormality, we induced venous occlusion, which enables the pooling of venous outflow in the lower leg (i.e. below the knee) compartments while still allowing arterial inflow. This scenario simulates several abnormal perfusion conditions in the lower leg, one of them being the acute compartment syndrome [ACS]. In order to test our research hypothesis, a novel portable light-weight non-invasive NIRS system was developed and tested. The clinical testing and results described in this chapter present a proof-of-concept effort to record a multi-channel depth-resolved near infrared spectroscopy data from healthy subjects. This effort is a first step toward the development of a clinical system to be used in future studies (Section 7.2).

Before we analyzed data for clinical applicability of the novel NIRS system, we explored variations between subjects and variations between two devices used in the study. Our results showed that both NIR and visible light sensors have very good correlation between subjects at time t_1. Chromophore concentration variations between different subjects may explain variances seen in our inter-subject data. In addition to correlation between subjects, we investigated the variance of control and test devices per each subject. To determine how variable our data was, we calculated coefficient of variability for each subject using sensor #3 (i.e. S3) data from control leg at times t_1 and t_2 and test leg at time t_1. The values of coefficient of variability for control leg device range from 0.0013 to 0.1556 versus 0.0124 to 0.4264 for the case which also considered test leg device. This indicates that variance in data between control and test sensors S3 on individual subject may be attributed to variance in optical components. It may be recalled that in Chapter 4 we implemented calibration procedure in order to minimize inter-device variations in analog amplification chain (Section 4.5). The calibration procedure was only implemented for analog amplification chain and it did not address differences that may exist between optical module components. As a result of these findings, use of single device per patient in clinical setting may be justified in order to minimize variations caused by different optical modules.

After we completed investigation of inter-subject data correlation and per subject inter-device variations, we explored clinical significance of acquired NIRS data. To do this, we divided clinical data analysis into four main sections: (1) Detection of oxygenation abnormality without baseline data, (2) Oxygenation monitoring with baseline data; (3) Effect of venous occlusion on NIRS signal at different tissue depths; and (4) Gender differences. Numerous clinical cases do not offer an opportunity to collect baseline data before the onset of pathology,

such as acute trauma and various complications. For these types of cases, we performed analysis of data after the onset of oxygenation abnormality (i.e. venous occlusion). The results returned statistically significant values which may indicate that novel NIRS system is capable of detecting abnormal lower leg oxygenation levels after the pathology had already started and when the contralateral unaffected leg is available as a control. We also investigated potential clinical applications of the novel NIRS system to situations where preventive long-term continuous monitoring of patients may be beneficial. To explore this possibility, we analyzed data and found that the novel NIRS system was able to reliably detect statistically significant oxygenation changes during venous occlusion in test leg. Clinically, these results could be used in development of NIRS system detection algorithms as they offer known baseline data. Next, we explored what effect depth of sampled tissue has on the acquired NIR and visible light data during venous occlusion. The results indicate that deeper muscle tissues experience greater change in detected visible light levels (i.e. deoxygenated hemoglobin levels), while the more superficial tissues show more pronounced changes in the detected NIR light levels (i.e. oxygenated hemoglobin levels). This information indicates that future clinical systems could be customized to include more NIR or more visible sensors, depending on specific perfusion pathologies that are depth-dependent, as means of maximizing acquisition of clinically-relevant information. Finally, we examined the inter-gender dependence of the acquired NIRS data based on known lower leg anatomical and physiological differences between females and males. The goal was to investigate the ability of the novel NIRS system to discern NIRS signals originating from female versus male subjects. Results showed that the system is capable of acquiring statistically significant information regarding the oxygenated and deoxygenated hemoglobin levels between genders during abnormal oxygenation states of lower leg tissues. These results

may influence design of future clinical NIRS system optical module and detection algorithms in order to improve clinically relevant data acquisition and detection.

In addition to the above data analysis procedures, several other data analysis tests were performed to see if additional information may be gathered from collected data. These additional tests included correlation of NIRS data to subjects' blood pressure values, calf circumference, age, and pneumatic cuff pressure values during venous occlusion. The outcomes of these tests yielded either inconclusive or no correlation results between NIRS data and variables of interest. The lack of correlation between these variables may be the result of our subject pool; all subjects in our study were healthy, in very good physical shape, and belonged to similar age group (Table 6-1).

Through the analysis of feasibility study results, we validated our research hypothesis that multi-channel depth-resolved near infrared spectroscopy can be used to monitor lower leg tissue oxygenation and lower leg oxygenation abnormalities. Additionally, we confirmed that depth-resolved data collection provides statistically significant information for analyzing the oxygenation state of tissues. Additional improvements and tests could now be identified for future development and testing of the clinical NIRS system.

Chapter 7

Conclusions and Future Work

The work described in this dissertation provides clinical motivation, development, testing, and clinical validation of a novel multi-channel depth-resolved near infrared spectroscopy system. The system was built from the ground-up based on the potential real-world clinical applications. It was designed to be portable, non-invasive, battery-operated and capable of long-term monitoring. After several iterations, the system was tested in a clinical setting on healthy subjects. The results of the feasibility study indicate that the NIRS system is capable of providing statistically significant information regarding:

1. Existence of tissue oxygenation abnormality without baseline information.
2. Onset of tissue oxygenation abnormality when baseline information is available.
3. Depth-resolved oxygenation status of underlying tissue.
4. Oxygenated and deoxygenated hemoglobin levels between genders during the abnormal oxygenation states of lower leg tissues.

Based on the shortcomings of the existing near infrared spectroscopy systems, I hypothesized that by utilizing multi-channel near infrared spectroscopy, improved depth-resolved lower leg tissue oxygenation information could be obtained from a hand-held portable system. Even though three prototype systems were hand-built in the laboratory, two systems used in the feasibility study performed flawlessly during a two-week period. Part of this can be

attributed to the devices robust design and the use of proven off-the-shelf components. Since this was a proof-of-concept system, its design has not been optimized for actual clinical use. The future clinical system will require certain modifications, improvements, and additional tests as outlined next.

7.1. System Improvements and Testing

7.1.1. Optical Module

Both functional tests and clinical data show that the most proximal NIR sensor saturates the photo detector during normal operation. This is a result of primarily two factors: (1) The photo detector sensitivity is greater for NIR light sensors than for the visible light sensors, and (2) The sensor current is too large for the given inter-optode distance. One way to gain useful information from this sensor is to implement a variable current control mechanism. This mechanism would reduce the current to more proximal sources and increase drive current to more distal sources. The caution must be exercised, however, when this mechanism is used as current variations between sensors must be taken into account when data is analyzed. Another way to gain useful information from the most proximal sensor would be to select a photo detector which has the same or similar spectral responses for visible and NIR light sensors. In addition to sensor detection improvements, the geometrical configuration of sensors and a detector may need to be changed or optimized depending on the results of phantom tests (Section 7.1.4).

7.1.2. Data Acquisition Unit

The current data acquisition unit is built as a prototype system with many unnecessary components and test parts. For the clinical system, the printed circuit board [PCB] should be redesigned to include only the necessary components. This would result in further reduction in size and weight and reliability of the overall system, which is desirable for devices that will be used in the field. In addition to PCB reduction, the clinical system should be placed in a more robust enclosure that would provide at least water resistance if not water-proofing capabilities. The user interface of the new enclosure would need to be made in such a way so that the patient is not able to accidently turn-off or disconnect the device during normal use. Finally, the clinical device should have an on-board memory storage unit (e.g., SD card) with sufficient capacity to store patient data for extended periods of time. The current prototype NIRS system lacks on-board data storage capability.

7.1.3. PC Software

The current PC software is capable of displaying up to 64 channels of data in real time or off line. For the clinical version of the NIRS system, PC application would need to be modified to include better data review options, as well as to include automated data analysis algorithms. One of the data analysis algorithms may include Linear Discriminant Algorithm [LDA] as an aid in clinical decision making. The LDA may utilize information from specific sensors and assign them greater or smaller decision-bearing weight based on the data collected during initial and future clinical studies (Section 7.2).

7.1.4. Phantom Tests

The current system optical configuration is linear in design (Figure 4-3). Depending on the clinical use and applications, linear placement of optical components (i.e. optical configuration) may not be the most optimal. A tissue phantom should be built and used in determining optimal clinically-specific optical configurations for the optical module. The phantom could be built using a clear acrylic reservoir for porcine or bovine blood storage, *ex vivo* porcine tissue sample, oxygen saturation reading port, oxygen-carbon dioxide mixing valve, and miscellaneous mechanical components (Figure 7-1).

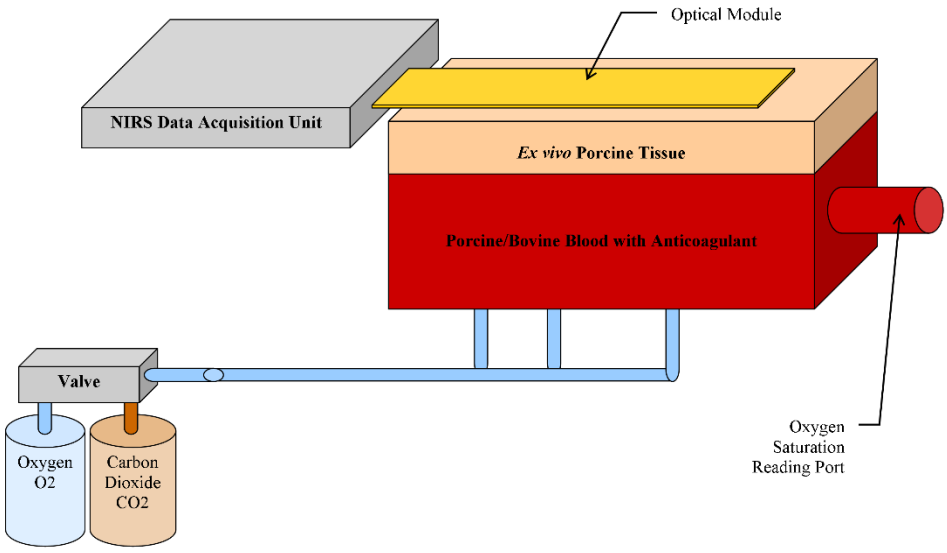

Figure 7-1 Optical Configuration Testing Phantom - Components and Setup

The phantom would operate in the following way: The porcine blood, containing heparin, is bubbled in the reservoir with either pure oxygen or carbon dioxide for approximately 15 minutes. This time will allow blood to become fully saturated with gas. Mixing different proportions of two gases, accomplished by different settings of the mixing valve, will permit variation in blood

oxygen saturation levels. The level of oxygen saturation in the reservoir should be monitored using the oxygen saturation reading port. Oxygen saturation data should be recorded over time and correlated with acquired NIRS data. In addition to saturation tests, the NIRS system depth resolution should be quantified using different thicknesses of *ex vivo* tissue samples at various levels of blood oxygen saturation. The resolution should be quantified for different tissue types individually and in various combinations.

7.2. Future Studies

The results of the present study have indicated the utility of a multi-channel depth-resolved near infrared spectroscopy system to detect normal and abnormal blood oxygenation states in healthy subjects. These results, however, represent only device proof-of-concept effort and are limited in scope. In order to truly explore clinical potential of the novel NIRS system, additional studies are required. One of the future studies may look at how the muscle orientation affects the NIRS signal during movement. Recent work by Sinha *et al.* [84], [85] suggests that diffusion tensor imaging [DTI] may be used for *in-vivo* calf muscle tracking, during rest or exercise. Furthermore, DTI may be used to verify data obtained with the novel NIRS system in patients with lower leg muscle ischemia [86], [87] or muscle denervation [88]. In order to conduct studies using DTI, the novel NIRS system must be redesigned so that it is compatible with the MRI system. In addition to these specific physiological studies, all future studies should include larger number of subjects (i.e. patients) representing different populations. Populations of interest may include patients with various existing or possible lower leg pathologies, various age groups, different melanin levels, as well as more even inclusion of both genders.

Appendix A

Supporting Feasibility study Documents

A-1 Subject Key Table Form

Subject Key Table

Subject № (1) _____ **Date:** _____

Time: _____

First Name: _____

Year of Birth: _____

Sex (circle one): **MALE** **FEMALE**

Telephone Number: _____

Email address: _____

---

(1) Number was generated using MATLAB *randi* function (one of 20 random numbers from interval 100,000 - 999,999)

Collected by: _____ Date: _____

A-2 Health History Questionnaire Form

Health History Questionnaire

Subject № _____ **Date:** _____

Time:

1. Do you currently have or have you ever had an extremity injury?

   YES ☐ NO ☐

2. Do you currently have or have you ever had any cardiac abnormalities?

   YES ☐ NO ☐

3. Do you have a history of peripheral vascular disease?

   YES ☐ NO ☐

4. Do you have a history of pulmonary disease?

   YES ☐ NO ☐

5. Do you smoke now or have you ever smoked regularly in the past?

   YES ☐ NO ☐

6. Do you have diabetes Type I or Type II?

   YES ☐ NO ☐

7. Are you pregnant now or are you taking any contraceptives?

   YES ☐ NO ☐

8. Are you physically able to lie still in a supine position for approximately one (1) hour?

   YES ☐ NO ☐

Current blood pressure values:

(S) _____ / (D) _____ [mmHg]

Collected by: _____ Date: _____

A-3 Study Table Form

Study Table

Subject № _____ **Date:** _____

Time: _____

Elapsed Time [s]	Pneumatic Cuff Pressure at Venous Occlusion [mmHg]	SpO_2 (RIGHT foot) [%]	SpO_2 (LEFT foot) [%]	BP (s/d)* [mmHg]	Heart Rate [BPM]	Remarks
0						baseline
180						
240						
540						
END OF STUDY PROCEDURE						

*s/d = systole / diastole

Data Collected by: _____ Date: _____

References

[1] Joel Mobley and Tuan Vo-Dinh, "Optical Properties of Tissue," in *Biomedical Photonics Handbook*, CRC Press, 2003.

[2] B. C. Wilson and S. L. Jacques, "Optical reflectance and transmittance of tissues: principles and applications," *Quantum Electronics, IEEE Journal of*, vol. 26, no. 12, pp. 2186–2199, 1990.

[3] D. W. Hahn, "Light Scattering Theory." Jul-2009.

[4] A. Ishimaru, "Wave propagation and scattering in random media. Volume I - Single scattering and transport theory," *Research supported by the U.S. Air Force, NSF, and NIH. New York, Academic Press, Inc., 1978. 267 p.*, vol. -1, 1978.

[5] A. Kienle, R. Michels, and R. Hibst, "Light propagation in a cubic biological tissue having anisotropic optical properties," in *Photon Migration and Diffuse-Light Imaging II*, Munich, Germany, 2005, vol. 5859, pp. 585917–7.

[6] A. Corlu, T. Durduran, R. Choe, M. Schweiger, E. M. C. Hillman, S. R. Arridge, and A. G. Yodh, "Uniqueness and wavelength optimization in continuous-wave multispectral diffuse optical tomography," *Opt. Lett.*, vol. 28, no. 23, pp. 2339–2341, Dec. 2003.

[7] E. Gratton, V. Toronov, U. Wolf, M. Wolf, and A. Webb, "Measurement of brain activity by near-infrared light," *J. Biomed. Opt.*, vol. 10, no. 1, pp. 011008–13, Jan. 2005.

[8] E. Okada and D. T. Delpy, “Near-Infrared Light Propagation in an Adult Head Model. I. Modeling of Low-Level Scattering in the Cerebrospinal Fluid Layer,” *Appl. Opt.*, vol. 42, no. 16, pp. 2906–2914, Jun. 2003.

[9] E. Okada and D. T. Delpy, “Near-Infrared Light Propagation in an Adult Head Model. II. Effect of Superficial Tissue Thickness on the Sensitivity of the Near-Infrared Spectroscopy Signal,” *Appl. Opt.*, vol. 42, no. 16, pp. 2915–2922, Jun. 2003.

[10] L. Alexandre and B. Jan, “Noninvasive monitoring of peripheral perfusion,” *Intensive Care Medicine*, vol. 31, no. 10, pp. 1316–1326, 2005.

[11] R. De Blasi, M. Cope, C. Elwell, F. Safoue, and M. Ferrari, “Noninvasive measurement of human forearm oxygen consumption by near infrared spectroscopy,” *European Journal of Applied Physiology and Occupational Physiology*, vol. 67, no. 1, pp. 20–25, Jul. 1993.

[12] M. C. P. Van Beekvelt, W. N. J. M. Colier, R. A. Wevers, and B. G. M. Van Engelen, “Performance of near-infrared spectroscopy in measuring local O2 consumption and blood flow in skeletal muscle,” *J Appl Physiol*, vol. 90, no. 2, pp. 511–519, Feb. 2001.

[13] Gratton Gabriele and Fabiani Monica, “Fast Optical Signals,” in *In Vivo Optical Imaging of Brain Function, Second Edition*, CRC Press, 2010, pp. 435–460.

[14] Huppert Theodore, Angela Franceschini Maria, and Boas David, “Noninvasive Imaging of Cerebral Activation with Diffuse Optical Tomography,” in *In Vivo Optical Imaging of Brain Function, Second Edition*, CRC Press, 2010, pp. 393–433.

[15] H. Gray, *Anatomy of the human body*, 20th ed. Philadelphia: Lea & Febiger, 1918.

[16] K. M. Patel and N. M. Major, “Compartmental Anatomy,” in *Imaging of Bone Tumors and Tumor-Like Lesions*, Springer Berlin Heidelberg, 2009, pp. 665–676.

[17] LadyofHats, “Circulatory System en.svg,” *Wikipedia, the free encyclopedia*. 05-Dec-2012.

[18] J. Hall and Guyton, *Guyton & Hall Textbook of Medical Physiology*, 11th ed. Saunders, 2005.

[19] S. McDonald and P. Bearcroft, “Compartment Syndromes,” *Semin Musculoskelet Radiol*, vol. 14, no. 02, pp. 236–244, May 2010.

[20] G. J. Mar, M. J. Barrington, and B. R. McGuirk, “Acute compartment syndrome of the lower limb and the effect of postoperative analgesia on diagnosis†,” *British Journal of Anaesthesia*, vol. 102, no. 1, pp. 3 –11, Jan. 2009.

[21] J. G. H. van den Brand, “Clinical Aspects of Lower Leg Compartment Syndrome,” University Utrecht, 2004.

[22] H. Janzing, “Epidemiology, Etiology, Pathophysiology and Diagnosis of the Acute Compartment Syndrome of the Extremity,” *European Journal of Trauma and Emergency Surgery*, vol. 33, no. 6, pp. 576–583, Dec. 2007.

[23] M. Hessmann, P. Ingelfinger, and P. Rommens, “Compartment Syndrome of the Lower Extremity,” *European Journal of Trauma and Emergency Surgery*, vol. 33, no. 6, pp. 589–599, Dec. 2007.

[24] M. M. McQueen, J. Christie, and C. M. Court-Brown, “Acute compartment syndrome in tibial diaphyseal fractures,” *J Bone Joint Surg Br*, vol. 78, no. 1, pp. 95–98, Jan. 1996.

[25] P. P. Oprel, M. G. Eversdijk, J. Vlot, W. E. Tuinebreijer, and D. den Hartog, “The Acute Compartment Syndrome of the Lower Leg: A Difficult Diagnosis?,” *Open Orthop J*, vol. 4, pp. 115–119.

[26] F. A. Matsen 3rd and R. B. Krugmire Jr, “Compartmental syndromes,” *Surg Gynecol Obstet*, vol. 147, no. 6, pp. 943–949, Dec. 1978.

[27] B. Gregory B., “Pathophysiology of free radical-mediated reperfusion injury,” *Journal of Vascular Surgery*, vol. 5, no. 3, pp. 512–517, Mar. 1987.

[28] P. R. Wood, P. F. Mahoney, and J. P. Cooper, “Compartment Syndrome,” in *Trauma and Orthopedic Surgery in Clinical Practice*, Springer London, 2009, pp. 103–107.

[29] F. Matsen, R. Winquist, and R. Krugmire, “Diagnosis and management of compartmental syndromes,” *J Bone Joint Surg Am*, vol. 62, no. 2, pp. 286–291, Mar. 1980.

[30] B. D. Browner, *Skeletal Trauma: Basic Science, Management, and Reconstruction*. Elsevier Health Sciences, 2003.

[31] R. J. Korthuis, J. K. Smith, and D. L. Carden, “Hypoxic reperfusion attenuates postischemic microvascular injury,” *American Journal of Physiology - Heart and Circulatory Physiology*, vol. 256, no. 1, pp. H315 –H319, Jan. 1989.

[32] B. Nachbur, “Vascular Trauma of the Lower Limb,” in *Vascular Surgery*, Springer Berlin Heidelberg, 2007, pp. 485–498.

[33] M. Odeh, “The Role of Reperfusion-Induced Injury in the Pathogenesis of the Crush Syndrome,” *New England Journal of Medicine*, vol. 324, no. 20, pp. 1417–1422, 1991.

[34] F. A. Matsen 3rd and D. K. Clawson, “The deep posterior compartmental syndrome of the leg,” *J Bone Joint Surg Am*, vol. 57, no. 1, pp. 34–39, Jan. 1975.

[35] A. R. Hargens, J. S. Romine, J. C. Sipe, K. L. Evans, S. J. Mubarak, and W. H. Akeson, “Peripheral nerve-conduction block by high muscle-compartment pressure,” *J Bone Joint Surg Am*, vol. 61, no. 2, pp. 192–200, Mar. 1979.

[36] A. Ames 3rd, R. L. Wright, M. Kowada, J. M. Thurston, and G. Majno, “Cerebral ischemia. II. The no-reflow phenomenon,” *Am. J. Pathol.*, vol. 52, no. 2, pp. 437–453, Feb. 1968.

[37] T. E. Whitesides Jr, T. C. Haney, H. Harada, H. E. Holmes, and K. Morimoto, “A simple method for tissue pressure determination,” *Arch Surg*, vol. 110, no. 11, pp. 1311–1313, Nov. 1975.

[38] R. B. Bourne and C. H. Rorabeck, “Compartment syndromes of the lower leg,” *Clin. Orthop. Relat. Res.*, no. 240, pp. 97–104, Mar. 1989.

[39] T. E. Whitesides, T. C. Haney, K. Morimoto, and H. Harada, “Tissue pressure measurements as a determinant for the need of fasciotomy,” *Clin. Orthop. Relat. Res.*, no. 113, pp. 43–51, Dec. 1975.

[40] K. G. B. Elliott and A. J. Johnstone, “Diagnosing acute compartment syndrome,” *J Bone Joint Surg Br*, vol. 85, no. 5, pp. 625–632, Jul. 2003.

[41] M. Mars and G. P. Hadley, “Raised compartmental pressure in children: a basis for management,” *Injury*, vol. 29, no. 3, pp. 183–185, Apr. 1998.

[42] S. J. Mubarak, C. A. Owen, A. R. Hargens, L. P. Garetto, and W. H. Akeson, “Acute compartment syndromes: diagnosis and treatment with the aid of the wick catheter,” *J Bone Joint Surg Am*, vol. 60, no. 8, pp. 1091–1095, Dec. 1978.

[43] J. M. Wiemann, T. Ueno, B. T. Leek, W. T. Yost, A. K. Schwartz, and A. R. Hargens, “Noninvasive measurements of intramuscular pressure using pulsed phase-locked loop ultrasound for detecting compartment syndromes: a preliminary report,” *J Orthop Trauma*, vol. 20, no. 7, pp. 458–463, Jul. 2006.

[44] C. Willy, H. Gerngross, and J. Sterk, “Measurement of intracompartmental pressure with use of a new electronic transducer-tipped catheter system,” *J Bone Joint Surg Am*, vol. 81, no. 2, pp. 158–168, Feb. 1999.

[45] “Hutchinson Technology BioMeasurement Division - NIRS and the InSpectra^{TM} StO2 Tissue Oxygenation Monitor.” [Online]. Available: http://www.htibiomeasurement.com/technology/nirs_and_the_inspectra_sto2/. [Accessed: 31-Jan-2013].

[46] G. Giannotti, S. M. Cohn, M. Brown, J. E. Varela, M. G. McKenney, and J. A. Wiseberg, “Utility of near-infrared spectroscopy in the diagnosis of lower extremity compartment syndrome,” *J Trauma*, vol. 48, no. 3, pp. 396–399; discussion 399–401, Mar. 2000.

[47] L. M. Gentilello, A. Sanzone, L. Wang, P. Y. Liu, and L. Robinson, “Near-infrared spectroscopy versus compartment pressure for the diagnosis of lower extremity compartmental syndrome using electromyography-determined measurements of neuromuscular function,” *J Trauma*, vol. 51, no. 1, pp. 1–8, discussion 8–9, Jul. 2001.

[48] J. M. Clayton, A. C. Hayes, and R. W. Barnes, “Tissue pressure and perfusion in the compartment syndrome,” *Journal of Surgical Research*, vol. 22, no. 4, pp. 333–339, Apr. 1977.

[49] A. Gersten, J. Perle, A. Raz, and R. Fried, “Probing brain oxygenation with near infrared spectroscopy,” *arXiv:1103.5502*, Mar. 2011.

[50] M. S. Shuler, W. M. Reisman, T. E. Whitesides, T. L. Kinsey, E. M. Hammerberg, M. G. Davila, and T. J. Moore, “Near-Infrared Spectroscopy in Lower Extremity Trauma,” *J Bone Joint Surg Am*, vol. 91, no. 6, pp. 1360–1368, Jun. 2009.

[51] T. Garabekyan, G. C. Murphey, B. R. Macias, J. E. Lynch, and A. R. Hargens, “New Non-Invasive Ultrasound Technique for Monitoring Perfusion Pressure in a Porcine Model of Acute Compartment Syndrome,” *J Orthop Trauma*, vol. 23, no. 3, pp. 186–194, Mar. 2009.

[52] J. Mobley and T. Vo-Dinh, “Optical Properties of Tissue,” in *Biomedical Photonics Handbook*, T. Vo-Dinh, Ed. CRC Press, 2003.

[53] D. Malacara-Hernández, “Optics for Engineers,” in *Photomechanics*, vol. 77, P. K. Rastogi, Ed. Berlin, Heidelberg: Springer Berlin Heidelberg, pp. 1–32.

[54] V. V. Tuchin and Society of Photo-optical Instrumentation Engineers, *Tissue Optics: Light Scattering Methods and Instruments for Medical Diagnosis*, 2nd ed. Bellingham, Wash: SPIE/International Society for Optical Engineering, 2007.

[55] S. L. Jacques, “Introduction to Biomedical Optics,” *Introduction to Biomedical Optics*, Jan-1998. [Online]. Available: http://omlc.ogi.edu/education/ece532/index.html. [Accessed: 30-Nov-2012].

[56] C. F. Bohren and D. R. Huffman, “Particles Small Compared with the Wavelength,” in *Absorption and Scattering of Light by Small Particles*, Wiley-VCH Verlag GmbH, 2007, pp. 130–157.

[57] C. F. Bohren and D. R. Huffman, “Angular Dependence of Scattering,” in *Absorption and Scattering of Light by Small Particles*, Wiley-VCH Verlag GmbH, 2007, pp. 381–428.

[58] L. Grossweiner, J. Grossweiner, and B. H. Gerald Rogers, “The Science of Phototherapy: An Introduction,” Springer Netherlands, 2005, pp. 9–55.

[59] L. Kocsis, P. Herman, and A. Eke, “The modified Beer–Lambert law revisited,” *Physics in Medicine and Biology*, vol. 51, no. 5, pp. N91–N98, Mar. 2006.

[60] Q. Luo, S. Nioka, and B. Chance, “Functional near-infrared imager,” pp. 84–93, Aug. 1997.

[61] B. Chance, Q. Luo, S. Nioka, D. C. Alsop, and J. A. Detre, “Optical investigations of physiology. A study of intrinsic and extrinsic biomedical contrast,” *Philosophical Transactions of the Royal Society of London. Series B: Biological Sciences*, vol. 352, no. 1354, pp. 707 –716, Jun. 1997.

[62] “Layers of the Skin,” *SEER Training Modules*. U. S. National Institutes of Health, National Cancer Institute, 12-Dec-2012.

[63] “Anatomy of the Skin,” *SEER Training Modules*. U. S. National Institutes of Health, National Cancer Institute, 12-Dec-2012.

[64] S. L. Jacques, “Skin Optics Summary,” *Skin Optics Summary*, Jan-1998. [Online]. Available: http://omlc.ogi.edu/news/jan98/skinoptics.html. [Accessed: 30-Nov-2012].

[65] S. A. Prahl, “Optical Absorption of Hemoglobin,” *Optical Absorption of Hemoglobin*, 19991215. [Online]. Available: http://omlc.ogi.edu/spectra/hemoglobin/index.html.

[66] A. N. Bashkatov, É. A. Genina, V. I. Kochubey, and V. V. Tuchin, “Optical properties of the subcutaneous adipose tissue in the spectral range 400–2500 nm,” *Opt. Spectrosc.*, vol. 99, no. 5, pp. 836–842, Nov. 2005.

[67] H. He, N. Zeng, R. Liao, T. Yun, W. Li, Y. He, and H. Ma, “Application of sphere-cylinder scattering model to skeletal muscle,” *Opt. Express*, vol. 18, no. 14, pp. 15104–15112, Jul. 2010.

[68] “Structure of Skeletal Muscle,” *SEER Training Modules*. U. S. National Institutes of Health, National Cancer Institute, 04-Dec-2012.

[69] S. A. Prahl, “Light transport in tissue,” Ph.D., The University of Texas at Austin, United States -- Texas, 1988.

[70] B. C. Wilson and G. Adam, “A Monte Carlo model for the absorption and flux distributions of light in tissue,” *Med Phys*, vol. 10, no. 6, pp. 824–830, Dec. 1983.

[71] L. Wang, S. L. Jacques, and L. Zheng, “MCML—Monte Carlo modeling of light transport in multi-layered tissues,” *Computer Methods and Programs in Biomedicine*, vol. 47, no. 2, pp. 131–146, Jul. 1995.

[72] S. A. Prahl, M. Keijzer, S. L. Jacques, and A. J. Welch, “A Monte Carlo Model of Light Propagation in Tissue,” in *SPIE Proceedings of Dosimetry of Laser Radiation in Medicine and Biology*, 1989, vol. IS 5, pp. 102–111.

[73] Tuan Vo-Dinh, “Biomedical Photonics,” in *Biomedical Photonics Handbook*, CRC Press, 2003.

[74] W. F. Cheong, S. A. Prahl, and A. J. Welch, “A review of the optical properties of biological tissues,” *IEEE Journal of Quantum Electronics*, vol. 26, no. 12, pp. 2166 –2185, Dec. 1990.

[75] R. Saager, “Corrected near infrared spectroscopy, C-NIRS: An optical system for extracting hemodynamic signatures unique to the brain,” University of Rochester, United States -- New York, 2008.

[76] C. Jäger, “Eye Safety of IREDs used in Lamp Applications,” Mar-2010. [Online]. Available: http://catalog.osram-os.com/catalogue/catalogue.do;jsessionid=64A829833A4FED421572D4957766AEFB?act=downloadFile&favOid=020000040001018500010 0b6. [Accessed: 17-Oct-2011].

[77] International Commission on Non-Ionizing Radiation Protection, “ICNIRP STATEMENT ON LIGHT-EMITTING DIODES (LEDs) AND LASER DIODES: IMPLICATIONS FOR HAZARD ASSESSMENT,” *Health Physics*, vol. 78, no. 6, 2000.

[78] K. P. Schmit-Neuerburg, “[The compartment syndrome as a sequela of trauma],” *Chirurg*, vol. 59, no. 11, pp. 713–721, Nov. 1988.

[79] B. Shadgan, M. Menon, D. Sanders, G. Berry, C. Martin, P. Duffy, D. Stephen, and P. J. O’Brien, “Current thinking about acute compartment syndrome of the lower extremity,” *Can J Surg*, vol. 53, no. 5, pp. 329–334, Oct. 2010.

[80] R. Kosir, F. A. Moore, J. H. Selby, C. S. Cocanour, R. A. Kozar, E. A. Gonzalez, and S. R. Todd, “Acute lower extremity compartment syndrome (ALECS) screening protocol in critically ill trauma patients,” *J Trauma*, vol. 63, no. 2, pp. 268–275, Aug. 2007.

[81] M. S. Shuler, W. M. Reisman, T. L. Kinsey, T. E. Whitesides, E. M. Hammerberg, M. G. Davila, and T. J. Moore, “Correlation between muscle oxygenation and compartment pressures in acute compartment syndrome of the leg,” *J Bone Joint Surg Am*, vol. 92, no. 4, pp. 863–870, Apr. 2010.

[82] J. Eng, “Sample Size Estimation: How Many Individuals Should Be Studied?1,” *Radiology*, vol. 227, no. 2, pp. 309–313, May 2003.

[83] A. Reisner, P. A. Shaltis, D. McCombie, and H. H. Asada, “Utility of the Photoplethysmogram in Circulatory Monitoring,” *Anesthesiology*, vol. 108, no. 5, pp. 950–958, May 2008.

[84] S. Sinha, U. Sinha, and V. R. Edgerton, “In vivo diffusion tensor imaging of the human calf muscle,” *J Magn Reson Imaging*, vol. 24, no. 1, pp. 182–190, Jul. 2006.

[85] S. Sinha and U. Sinha, “Reproducibility Analysis of Diffusion Tensor Indices and Fiber Architecture of Human Calf Muscles in vivo at 1.5 Tesla in Neutral and Plantarflexed Ankle Positions at Rest,” *J Magn Reson Imaging*, vol. 34, no. 1, pp. 107–119, Jul. 2011.

[86] A. M. Heemskerk, M. R. Drost, G. S. van Bochove, M. F. M. van Oosterhout, K. Nicolay, and G. J. Strijkers, “DTI-based assessment of ischemia-reperfusion in mouse skeletal muscle,” *Magn Reson Med*, vol. 56, no. 2, pp. 272–281, Aug. 2006.

[87] A. M. Heemskerk, G. J. Strijkers, M. R. Drost, G. S. van Bochove, and K. Nicolay, “Skeletal muscle degeneration and regeneration after femoral artery ligation in mice: monitoring with diffusion MR imaging,” *Radiology*, vol. 243, no. 2, pp. 413–421, May 2007.

[88] T. Saotome, M. Sekino, F. Eto, and S. Ueno, “Evaluation of diffusional anisotropy and microscopic structure in skeletal muscles using magnetic resonance,” *Magn Reson Imaging*, vol. 24, no. 1, pp. 19–25, Jan. 2006.